Robot Navigation in Distorted Magnetic Fields

von Leif Christensen

Dissertation

zur Erlangung des Grades eines Doktors der
Ingenieurwissenschaften
- Dr.-Ing. -

Vorgelegt im Fachbereich 3 (Mathematik & Informatik)
der Universität Bremen
im September 2019

Datum des Promotionskolloquiums: 28.11.2019

Gutachter: Prof. Dr. Dr. h.c. Frank Kirchner (Universität Bremen)
Prof. Dr. Oliver Zielinski (Carl von Ossietzky Universität Oldenburg)

Abstract

This thesis investigates the utilization of magnetic field distortions for the localization and navigation of robotic systems. The work comprehensively illuminates the various aspects that are relevant in this context. Among other things, the characteristics of magnetic field environments are assessed and examined for their usability for robot navigation in various typical mobile robot deployment scenarios.

A strong focus of this work lies on the self-induced static and dynamic magnetic field distortions of complex kinematic robots, which could hinder the use of magnetic fields because of their interference with the ambient magnetic field. In addition to the examination of typical distortions in robots of different classes, solutions for compensation and concrete tools are developed both in hardware (distributed magnetometer sensor systems) and in software. In this context, machine learning approaches for learning static and dynamic system distortions are explored and contrasted with classical methods for calibrating magnetic field sensors.

In order to extend probabilistic state estimation methods towards the localization in magnetic fields, a measurement model based on Mises-Fisher distributions is developed in this thesis.

Finally, the approaches of this work are evaluated in practice inside and outside the laboratory in different environments and domains (e.g. office, subsea, desert, etc.) with different types of robot systems.

Zusammenfassung

Diese Arbeit beschäftigt sich mit der Nutzbarmachung der Verzerrungen von Magnetfeldern für die Lokalisierung und Navigation von robotischen Systemen. Die Arbeit beleuchtet dabei umfassend die verschiedenen Aspekte, die hierbei relevant werden können. Unter anderem werden die Charakteristiken von Magnetfeldumgebungen in verschiedenen Szenarien untersucht, in denen Roboter typischerweise zum Einsatz kommen und auf ihre Nutzbarkeit für die Navigation hin untersucht.

Einen großen Teil nimmt weiterhin die Untersuchung der selbstinduzierten statischen wie dynamischen Magnetfeldverzerrungen von komplexen kinematischen Robotern ein, die der Nutzung von Magnetfeldern entgegenstehen könnten. Hierzu werden im Rahmen der Arbeit neben der Ermittlung von typischen Verzerrungen Roboter verschiedener Klassen auch Lösungsansätze zur Kompensation und konkrete Werkzeuge sowohl in Hardware (verteilte Magnetometersensorik-Systeme) als auch in Software entwickelt. Dabei werden unter anderem Ansätze des maschinellen Lernens zur Erfassung der statischen und dynamischen Verzerrungen verfolgt und klassischen Methoden zur Kalibrierung von Magnetfeldsensoren gegenübergestellt.

Um die Zustandsschätzung mittels probabilistischer Methoden um die Möglichkeiten der Lokalisierung in Magnetfeldern zu erweitern, wird darüber hinaus in dieser Arbeit ein auf von Mises-Fisher-Verteilungen basierendes Messmodell entwickelt.

Abschließend werden die Ansätze dieser Arbeit im konkreten Einsatz innerhalb und außerhalb des Labors in unterschiedlichen Umgebungen und Domänen (u.a. Unterwasser, Wüste) mit verschiedenen Arten von Robotersystemen evaluiert.

Acknowledgements

First and foremost, I would like to thank my colleagues who shared the very productive and stimulating PhD student retreats over the last years with me. The discussions and the suggestions given there were invaluable. In particular, I would like to thank my supervisor Prof. Dr. Frank Kirchner, who has always encouraged me to follow the not so well-trodden path of using distorted magnetic fields for localization purposes.

I am very grateful for the opportunities that the German Research Center for Artificial Intelligence - Robotics Innovation Center offered me with its unique collection of different types of robots and infrastructure, that I was fortunate to be able to use during the course of my work. Without this large variety of robots at the institute and the support of their system administrators, this thesis wouldn't have been possible.

Furthermore, I would like to thank my former team leaders Dr. Jan Albiez, Dr. Jakob Schwendner and Dr. Stefan Stiene, who not only backed me up in my daily work in order to pursue my goal, but also gave me valuable advice for my doctoral thesis due to their long experience in the field of robotics science. I would also like to thank Dr. Hendrik Müller from the Federal Institute for Geosciences and Natural Ressources (BGR), who, at the very beginning of my work, provided valuable insights into the world of magnetism and magnetometers from the perspective of a physicist.

The extensive field trials campaign in the Mars-like environment of the desert of Utah (US) was a particularly one-of-a-kind experience that pushed me forward in my work. In this context I would like to say a special thank you to the whole field trials Utah team. I wish to thank Dr. Johannes Lemburg, Martin Fritsche and Christopher Gaudig, who always provided thematic as well as moral support when I felt a little bit lost in my endeavor. Special thanks go to Dr. Florian Cordes, who took it upon him to read through the entire thesis and mercilessly pointed out to me not only mistakes in sentence construction.

Finally and above all, I would like to thank my family. This work is dedicated to them.

Contents

Chapter 1

Introduction

The magnetic field of our planet Earth is available at the deepest points of the seafloor and in the troposphere where most airplanes fly, in buildings as well as in the most remote outdoor places, even deep underground in the Earth crust. Basically, if one is not located in a zero-Gauss chamber, the magnetic field will be measurable. Since the magnetic flux is not a scalar value but has a certain direction and strength, the magnetic field may be significantly distorted in both of these components, but it will be there.

This may not be true for all planets, but fortunately on Earth, the magnetic field is not only available, but it also has a certain exploitable and defined quasi-static structure (for details see section 2.3), that is quite robust against disruptions, that otherwise often restrict or even prevent the function of sensors used in mobile robotics.

However, since the beginning of the usage of magnetic needles in the 11th century, the utilization of the Earth magnetic field for navigation purposes, although refined, has not come very far: the basic principle is still to use only the projected horizontal component of the magnetic field for heading estimation, ignoring other available information from the local magnetic field vector.

Whereas humans don't have the capability to sense the magnetic field directly by themselves, it is known that certain species of migratory birds are using geographic variations in the strength and inclination of the magnetic field to determine their position [Hiscock et al., 2017]. In fact, after the first discovery of magnetotaxis in certain bacteria in 1963, magnetoreception has been discovered in a variety of species, for example salmon, homing pigeons, honeybees and sea turtles [Kirschvink et al., 2001]. For specific species, there is evidence that the magnetoreception may be related to cryptochromes in the retina as well as to magnetite

(a) *Migrating Birds* **(b)** *Leatherback Sea Turtle*

Figure 1.1: *Animals with magnetic field sensing capabilities (Magnetotaxis)*

crystals in parts of the beak [Johnsen and Lohmann, 2008]. And although the specific sensory principle of magnetoreception in animals is still a field of ongoing research, it is clear, that biological systems like those depicted in figure 1.1 are ingeniously exploiting the features of the surrounding magnetic field deeper than we currently do by merely using a compass.

1.1 Motivation

Navigation is a topic that has had huge influences in the past of mankind, society and trade. Arising technical inventions combined with long gathered knowledge often constituted new navigational methods with a major impact. For example the invention of the marine chronometer combined with knowledge of the stars allowed for precise astronavigation, which in turn paved the way for the age of exploration: estimating the latitude was already possible by measuring the altitude of celestial bodies like Polaris with a sextant and looking up the coordinates schedule in an almanac, but solving the longitude problem took great efforts over centuries and only the substitution of estimating lunar distances with precise time measurements after the invention of the modern chronometer in 1761 allowed for precise localization that was needed for modern maritime trade.

Today's commercial localization technique has found its reference technology in Global Navigation Satellite Systems (GNSS, e.g. GPS), but is only applicable to surface navigation, where there is a free view of the sky, and may deteriorate or even fail completely in more demanding environments. Even in established and well-defined application scenarios, it is often needed to supplement the major sensor modality with extra sensing capabilities that make the localization solution more robust and are crucial in situations, where certain sensors might fail (see for example figure 1.2).

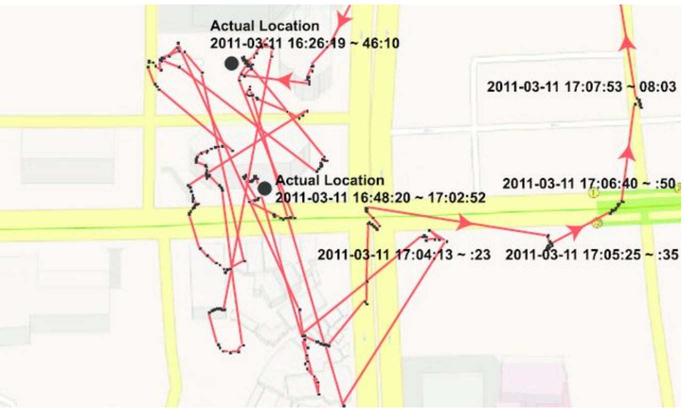

Figure 1.2: *Position estimation failure due to multipath GNSS signals in urban environment from [Lee et al., 2013]*

Current robots are taking a more and more prominent role in the world of today, where they have to leave classic domains like (aero-)nautical or indoor office environments and have to cope with increasingly tough environments in more demanding and unstructured terrain, where humans or remote-controlled systems cannot go. And in correlation with the progress of robotic skills and the advances in the degree of autonomy, expectations are raised and society legitimately demands that robotic systems support humans not only in laboratory environments but in real-world scenarios (see e.g. [Garcia-Soto et al., 2017]), from everyday situations at home to most challenging and maybe also dangerous tasks.

The area of localization and mapping plays an important role in robotics since decades and has seen huge advances in recent years (see Chapter 3), nonetheless, there are still open issues, especially when leaving laboratory or office-like environments and dealing with long term autonomous robotic operations. Commonly used sensors in such applications, apart from the aforementioned global navigation satellite systems, often include sensors in the visual spectrum like cameras (stereo, time of flight, monocular, RGB-D, etc.), LIDARs or different kinds of sonars (especially in the underwater domain) as well as a huge variety of other exteroceptive sensors [Thrun et al., 2005, Siegwart et al., 2017], all of which may fail in certain scenarios depending on the ambient condition of the situation at hand. For example, strong smoke or excessive dust may significantly limit the effectiveness of such sensors in disaster scenarios, the same holds true for intense turbidity or marine snow conditions in subsea applications. Sensors utilizing the runtime of signals (e.g. GPS, acoustic sonar, etc.) may be subject to strong performance restrictions due to multipath effects or even complete signal extinction as a result of total internal reflection at the interface between two media, a common problem in subsea navigation due to strong thermoclines.

The main two motivations for this thesis are thus:

1. The ambient magnetic field carries more information than we currently make use of, as indicated by animal magnetotaxis.
2. Since the ambient magnetic field is unaffected by a lot of effects that restrict commonly deployed localization sensors, magnetometers can play a crucial role both as an additional sensor modality for increased performance in mobile robot navigation as well as a complementary sensor to increase localization robustness in case of complete signal dropouts of the other deployed sensor modalities.

1.2 Thesis Structure

However, in order to fully exploit the benefits of the almost omnipresent magnetic field for mobile robot navigation, several questions arise:

- What are the general features of the Earth magnetic field with regard to robot localization?
- How do local ambient magnetic fields look like in different application scenarios for robots (vector field structure)? Is there exploitable information with regard to robot localization and are the signals strong enough (vector field key parameters)? Are they static enough in time for our purpose?
- Do robots themselves distort the ambient magnetic field and to what extent? Can we identify typical sources of self-induced magnetic distortions for different classes of mobile robots?
- How can we compensate those disturbances? Can they be analytically modeled based on the physical principles or can they be learned?
- Finally, can we enhance the localization of very compact or complex robots using ambient magnetic fields?

The thesis is structured alongside these questions (see figure 1.3). Chapters 2 and 3 provide the foundations for this thesis, describing magnetism, the Earth magnetic field and magnetic distortion types as well as the current state of the art. Chapters 4 and 5 then assess the magnetic field characteristics of different application environments and for different types of mobile robotic systems. The technical core contributions are described in Chapters 6 – 8: Chapter 6 describes a distributed magnetometer array approach and related algorithms based on vonMisesFisher (vMF) distributions, Chapter 7 discusses the application of machine learning techniques for magnetic field distortion compensation on complex mobile robotic systems and Chapter 8 addresses the localization of robotic systems in magnetic fields. Finally, Chapter 9 concludes the work of this thesis and gives an outlook on future work in the area of magnetic field navigation.

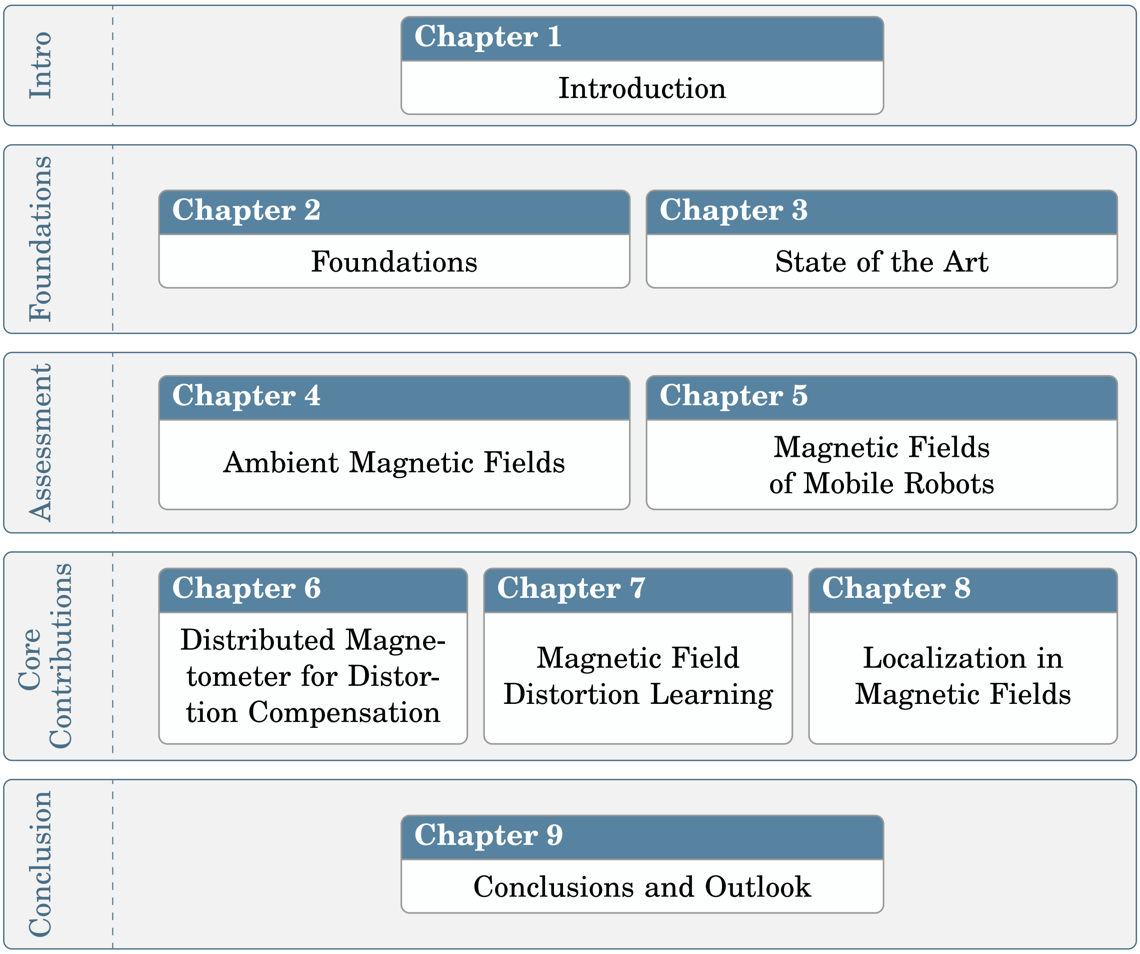

Figure 1.3: *Structure of this thesis*

Chapter 2

Foundations

2.1 Magnetism and Magnetic Fields

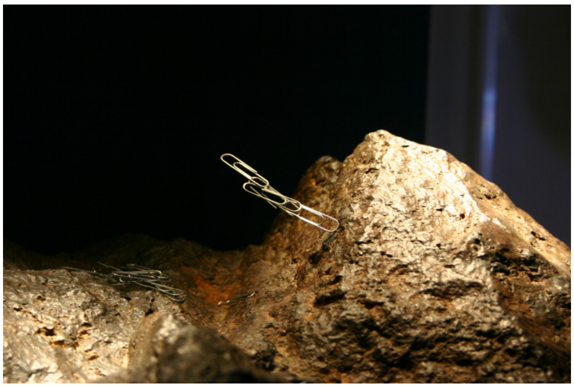

Figure 2.1: *A magnetic lodestone attracting iron paper clips*

Magnetism describes a set of physical phenomena mediated by magnetic fields. Magnetism is one of the four fundamental forces in physics, and magnetic fields are influencing and are being influenced by magnets and magnetized objects as well as electrical currents. The attraction of iron to basalt magnetite minerals (Fe_3O_4) called 'lodestones' is known to mankind since centuries and was first described in ancient China. Later, in his pursuit of trying to explain natural objects and phenomena by theories and hypotheses instead of resorting to mythology, the earliest debate with scientific character on magnetism is attributed to *Thales of Miletus* (624-546 BC). The scientific philosopher and mathematician is counted as one of the Seven Sages of Ancient Greece, otherwise best known for his mathematical theorems on elementary geometry. The first experimental research on magnetism was done in the middle ages by the scholar *Petrus Peregrinus* with his work "Epistola de Magnete", published in

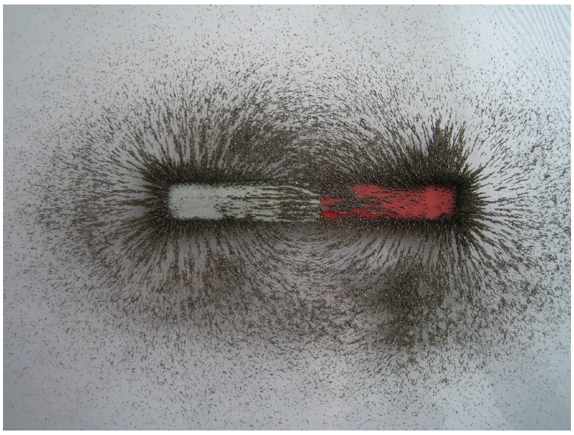

Figure 2.2: *The magnetic field surrounding a permanent dipole magnet made visible by iron filings*

1269. Peregrinus discovered the dipolarity of magnets: having created a sphere from a huge lodestone, he evaluated the alignment of an iron needle on this sphere towards the poles, although he still attributed the magnetic properties to the celestial dome instead to the Earth. After the discovery of the influence of electric currents on magnet fields by *Hans Christian Øersted* in 1819 and further research by *Ampere, Faraday and Henry* in the 19th century, the work by *James C. Maxwell* finally lead to a set of partial differential equations that found the basis for the new combined field of *electromagnetism* [Maxwell, 1865]. Because of his unifying work we know today, that the forces mediated by a magnetic field are just one manifestation of this underlying physical phenomenon.

A *magnetic field* is a vector field allocating a three-dimensional vector to every point in a subspace, describing the effect of the magnetic force (direction, intensity) at that location. Unlike the electric field component, the magnetic field component has no dedicated sources, it is *source-free*, but is generated by moving electric charges or time-varying electrical fields. This also holds true for fields originating from magnetic material, since they are caused by lined up magnetic moments of free electron pairs [Barnert et al., 2000]. The magnetic field can be expressed by two physical quantities, the magnetic field strength $\vec{H}$ with SI unit ampere per meter ($\mathrm{A\,m^{-1}}$) or the magnetic flux density $\vec{B}$ with derived SI unit tesla (T). Both are often just called 'magnetic field', their absolute value 'magnetic strength' or 'magnetic field strength', with $\vec{B}$ and $\vec{H}$ being closely related and proportional to each other in vacuum by the magnetic constant, the *vacuum permeability* $\vec{\mu_0}$:

$$\vec{B} = \mu_0 \vec{H} \tag{2.1}$$

In the following, this work is referring to $\vec{B}$ and the corresponding unit *tesla*, when talking about the magnetic field. Also, *magnetic flux density* and *magnetic field strength* are used interchangeably, both describing the length of a magnetic field vector $\vec{b} = (b_x, b_y, b_z)^\intercal$ at a certain point in the field $\vec{B}$ by their Euclidean norm (a.k.a. $\mathbf{L^2}$ norm):

$$\|\vec{b}\|_2 = \sqrt{{b_x}^2 + {b_y}^2 + {b_z}^2} \tag{2.2}$$

When not in a vacuum, the *magnetic permeability* μ describes the ability of a material to support the formation of a magnetic field inside it in the presence of an external magnetic field. For low-frequency fields like the geomagnetic field, μ can be considered a material-dependent scalar value and μ_r describes the relative permeability with respect to the magnetic constant μ_0 (the permeability in a vacuum):

$$\mu_r = \frac{\mu}{\mu_0} \tag{2.3}$$

The magnetic permeability plays an important role for robot navigation in magnetic fields, because it defines the reaction of a certain material (material in the local environment or material, the robot is built from) in the presence of the geomagnetic field. Depending on their permeability, materials are usually classified as *diamagnetic*, *paramagnetic* and *ferromagnetic*. Apart from strong diamagnetic superconductors with μ_r close to zero, most *diamagnetic* material shows a permeability slightly less than vacuum, examples are lead, copper or water ($\mu_r \approx 1 - 9 \times 10^{-6}$). Plastic material like polyethylene is considered completely neutral, while *paramagnetic* material like air or metals like aluminum, titanium or platin have a relative permeability also close to one, but slightly larger. The effects of both diamagnetic and paramagnetic common materials on the geomagnetic field are so small that they are neglectable with respect to the purpose of this work. In contrast to diamagnetic and paramagnetic material, that assumption doesn't hold for the third class of material with respect to their permeability, the *ferromagnetic* material (see schematic diagram 2.3). They have a very high relative permeability, with μ_r ranging from 300 to 300000, depending on the material at hand. Such materials like iron, cobalt or nickel show strong internal alignment parallel to the applied external field with a non-linear amplifying effect. Such material is quite common in robotic systems, since they are the core component for electromagnetic coils and motors.

Another key parameter of ferromagnetic material is the *magnetic remanence*, meaning the tendency to keep an internal magnetization, once the externally applied field

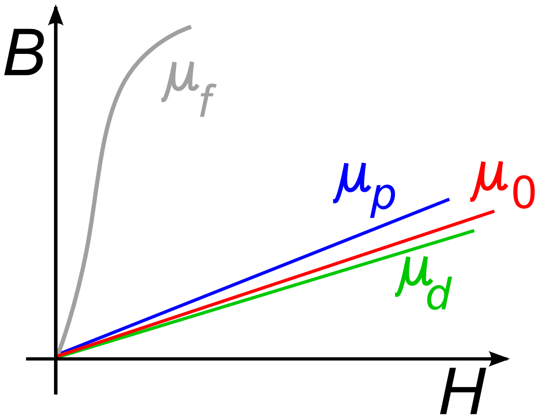

Figure 2.3: *Schematic diagram of different classes of magnetic permeability in material. While diamagnetic and paramagnetic material (μ_d, μ_p) show a proportional relationship and are close to the permeability in vacuum (μ_0), ferromagnetic material (μ_f) reacts with a much higher internal flux density B, when exposed to an external magnetic field H.*

is removed. The amount of magnetic remanence is dependent on the material-specific hysteresis curve, and a distinct hysteresis effect is desired for e.g. permanent magnets. This characteristic is also called *hard iron effect*, as opposed to the *soft iron effect*, where the material quickly loses the remnant internal magnetization, once the external magnetic field is removed. Pure non-alloyed iron, for example, shows strong soft iron characteristics, while alnico alloys or neodymium magnets composed of neodymium, iron and boron ($Nd_2Fe_{14}B$) show very strong hard iron effects.

Concerning electromagnetism, a magnetic field $\vec{B}$ exerts a force (the *Lorentz force*) $\vec{F}_L$ on a moving electrical charge q, proportional to the velocity $\vec{v}$ of the charge:

$$\vec{F}_L = q\vec{v} \times \vec{B} \tag{2.4}$$

This correlates with the inverse effect when electric charges are flowing through a conductor, e.g. a wire: The current I is generating a magnetic field concentric to the axial direction of the current flow (see figure 2.4). If the wire is forming an ideal coil with n windings of length l, the magnetic flux density B is then given by

$$B = \mu_0 \cdot \mu_r \cdot I \cdot \frac{n}{l} \tag{2.5}$$

with μ_r being the relative permeability constant for the material enclosed by the coil and μ_0 the magnetic constant (permeability in a vacuum).

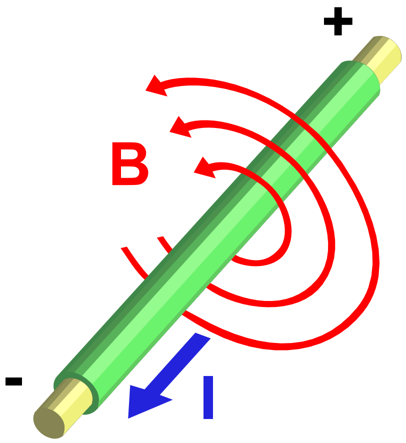

Figure 2.4: *Electric current I flowing through a wire, generating a magnetic field B concentric to the technical flow direction*

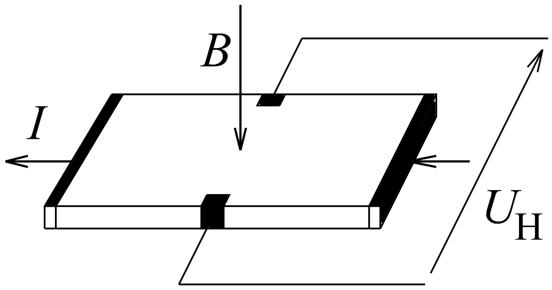

Figure 2.5: *Principle of a sensor exploiting the Hall effect*

The same principles are governing the Hall effect, which can be used for directional magnetometer sensors. The charge carriers of a current-carrying semiconductor exposed to an external magnetic field experience a force perpendicular to the plane established by the current direction and the magnetic field vector. The corresponding charge surplus in the opposite sites of the conductor is creating an electrical field compensating the Lorenz forces. The difference in charge is called the Hall voltage U_H, which then can be measured and is proportional to the magnetic field strength (see figure 2.5). Combining lateral and vertical Hall elements on a chip, the full 3D-vector of the magnetic flux density can be measured.

2.2 Magnetic Field Distortion Types

In direct response to the aforementioned hard- and soft iron characteristics of specific materials as well as the magnetic fields induced by electric current flowing through a wire (section 2.1), the typical distortions of local magnetic fields can be grouped in two classes, in so-called *soft iron distortion* and *hard iron distortion* [Caruso, 2000].

In the case of *soft iron* material, where the strong internal magnetization is in the same direction as the external field the material is exposed to, the material basically provides a path of lower impedance for the external field. Thus, the external field is just diverted, depending on the alignment of the material in the external field: a solid pure iron rod oriented in parallel to the external field has no effect on the direction of the external field vectors since the path of lower impedance is in the same direction. The same holds true for an arrangement of the iron rod directly perpendicular to the external field since a deflection to either side of the rod then has equally low impedance. Imagining a full 360° circle of the rod in a static external field, starting parallel to the magnetic field lines, there is no deviation at 0° (parallel), 90° (perpendicular), 180° (parallel) and 270° (perpendicular), but significant deflections in between. The deflections are different when going from perpendicular to parallel, then they are when going from parallel to a perpendicular alignment, but the same after a 180° turn, since the enclosing acute-angle between the rod longitudinal axis and the field is the same. A plot of the deviation in 2D would thus show a point-symmetric tilted ellipse with its center in the origin (see figure 2.6). Such deviation properties are called *two-cycle characteristics*.

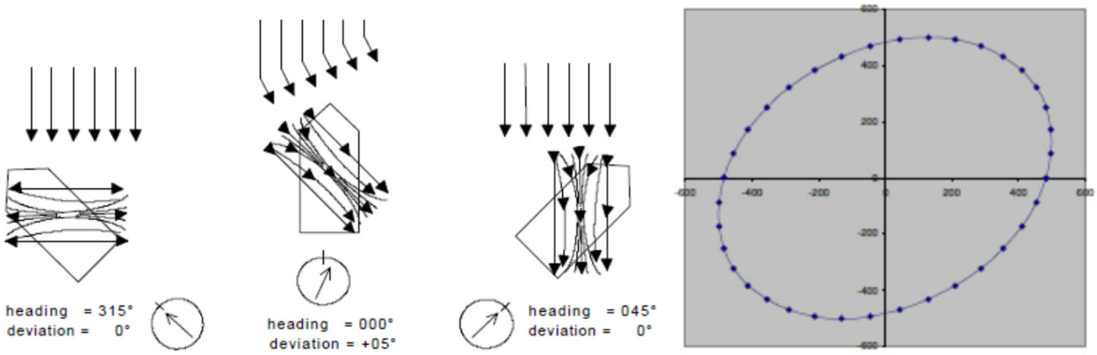

Figure 2.6: *Soft iron distortion provides a path of lower impedance for the external field, thus diverting it. The deviation has a two-cycle characteristic.*

Opposed to that is the second class of magnetic field distortions, the *hard iron* effect, for example from permanent magnets, as well as electromagnetically induced magnetic fields. Here, an individual magnetic field exists with its own different direction

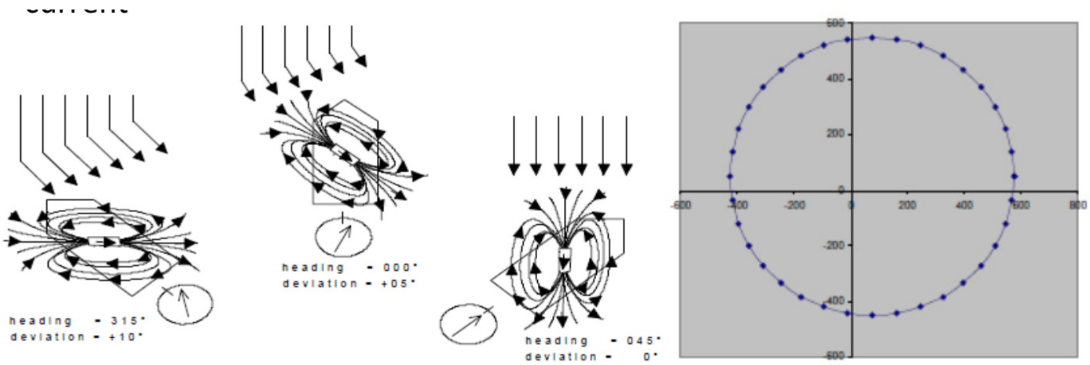

Figure 2.7: *Hard iron distortion superimposes an additional own magnetic field on the external field, thus creating a constant offset depending on alignment. The deviation for a full turn has a one-cycle characteristic, resulting in an off-centered sphere.*

and strength, which consequently superimposes the external field. The magnetic field vectors at the same point in space are combined via vector addition. In the case of the hard iron effect, the magnetic remanence in such material generates this magnetic field, in the electromagnetic case, it is caused by the electrical charges flowing through a wire.

Again imagining a full $360°$ circle in a static uniform external field, but this time with a rod with hard iron characteristics: when in parallel with the external field, the hard iron-induced magnetic field will not change the external field's direction, but contribute fully to the strength component, depending if it points to the same direction or the direct opposite. When not in parallel, both direction and strength components are affected, again as expected from vector addition. In this case, a plot of the deviation in 2D would show an undistorted sphere with a constant offset from the origin (see figure 2.7). Such deviation properties are called *one-cycle characteristics*.

Distortion Type Summary

In summary, depending on the alignment of the material in the magnetic field, the results of both distortions types are quite different and this difference in the deviation characteristics will be crucial when modeling or trying to learn the deviations of deflecting and superimposing magnetic fields. It also has to be noted, that both the soft iron as well as the hard iron effect usually don't exist in isolation, but so-called hard iron material also shows to some extent the soft iron effect and vice versa.

2.3 The Earth Magnetic Field

The Earth, like most other planets of our solar system apart from Venus and Mars, is equipped with a magnetosphere, which in case of the Earth extends several tens of thousands of kilometers into space from the ionosphere. Our magnetosphere is critical not only to mankind but the whole flora and fauna, since it deflects charged particles of the solar wind and protects, for example, our ozone layer from being stripped away by cosmic radiation.

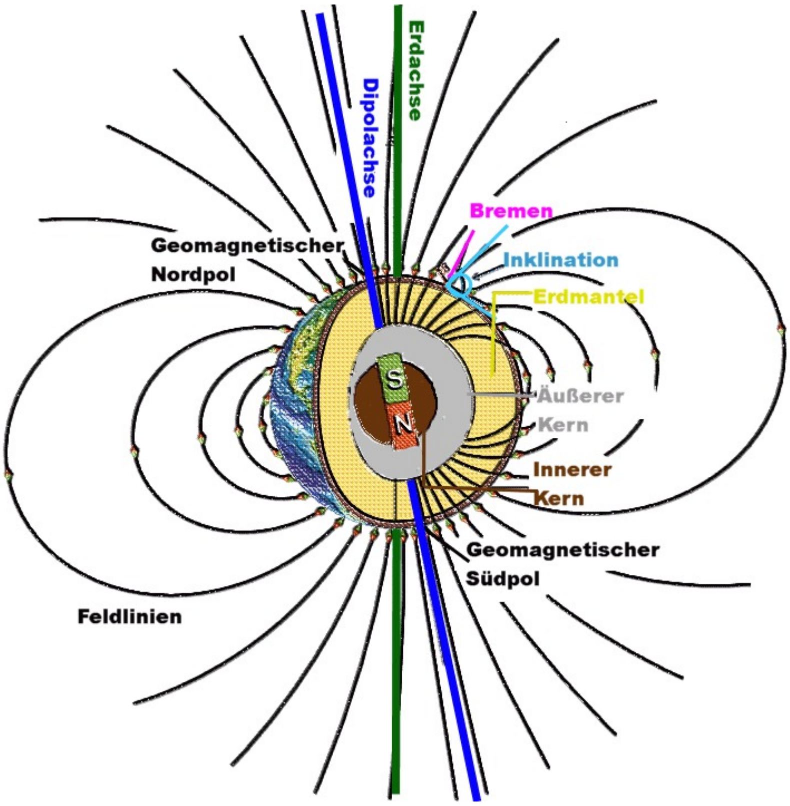

Figure 2.8: *The geomagentic field can be first-order approximated as a magnetic dipole sitting in the center of the Earth and tilted from the Earth's rotational axis by* 9.6°

Although magnetism was already known in ancient times (see section 2.1), the first description of the use of the geomagnetic field for navigational purposes by utilizing a magnetized needle is attributed to Shen Kuo, a Chinese scientist of the 11th century [Kuo, 1088]. However, the idea that the earth itself has some magnetic properties was not brought up before the year 1600, when the English physician and scientist William Gilbert published his work "De Magnete" (figure 2.9), the first systematic description of the geomagnetic field as the cause for the reproducible orientation of magnetized objects [Gilbert, 1600]. Gilbert's findings were based on rigorous experi-

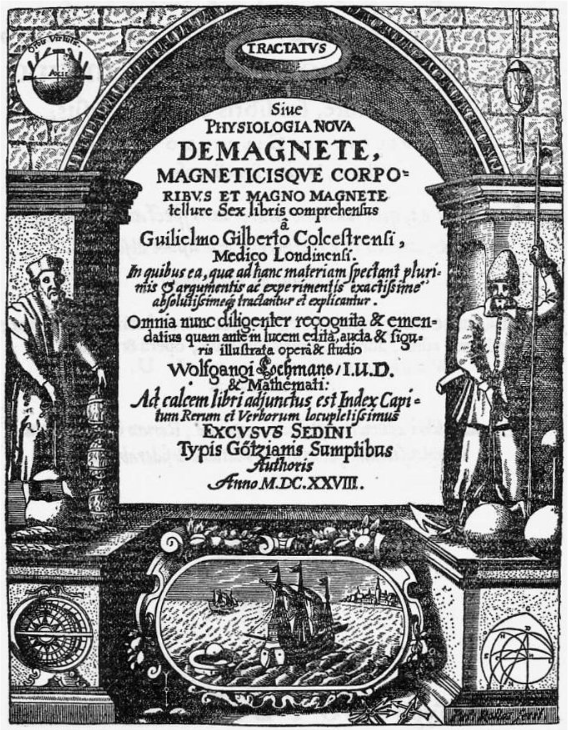

TRACTATVS
Siue
PHYSIOLOGIA NOVA
DE MAGNETE,
MAGNETICISQVE CORPO-
RIBVS ET MAGNO MAGNETE
tellure Sex libris comprehenſus
â
Guilielmo Gilberto Colceſtrenſi,
Medico Londinenſi.
In quibus ea, quæ ad hanc materiam ſpectant pluri-
mis & argumentis ac experimentis exactiſsime
abſolutiſsimeq; tractantur et explicantur.
Omnia nunc diligenter recognita & emen-
datius quam ante in lucem edita, aucta & figu-
ris illuſtrata operâ & ſtudio
Wolfgangi Lochmans/I.U.D.
& Mathemati:
Ad calcem libri adjunctus est Index Capi-
tum Rerum et Verborum locupletiſsimus
EXCVSVS SEDINI
Typis Götzianis Sumptibus
Authoris
Anno M.DC.XXVIII.

Figure 2.9: *Title page of William Gilbert's De Magnete - edition from 1628*

ments with a *terella*, a small magnetized model ball representing the Earth. Gilbert rejected the ancient theories of magnetism and was the first to argue correctly, that the Earth's center must be made of iron. Although Gilbert was profoundly convinced that electricity and magnetism were different things, which was later disproved by Hans Christian Oersted and James Clerk Maxwell as being two aspects of electromagnetism, he is regarded as one of the fathers of electricity and magnetism.

The work to systematically measure the geomagnetic field also led to the foundation of the "Magnetischer Verein" by Carl Friedrich Gauß and Wilhelm Weber with support by Alexander von Humboldt in 1834, which is considered to be one of the first truly international scientific endeavours with more than 50 participating observatories in Europe, Asia, Africa, North America and the South Seas. It was established to systematically describe the geomagnetic field and its observed dynamic fluctuations, providing magnetic maps for the whole terrestrial globe, and also proved that the main and static contribution to the geomagnetic field originates from the Earth core. Gauß also constructed the first magnetometer to be able to measure an absolute value of the Earth's magnetic field, the unit for the magnetic flux density in the CGS system is named in the honor of his work, superseded later by the unit *tesla*, with $1\,\mathrm{G} = 1 \times 10^{-4}\,\mathrm{T}$.

The geomagnetic field can be first-order approximated as a magnetic dipole sitting in

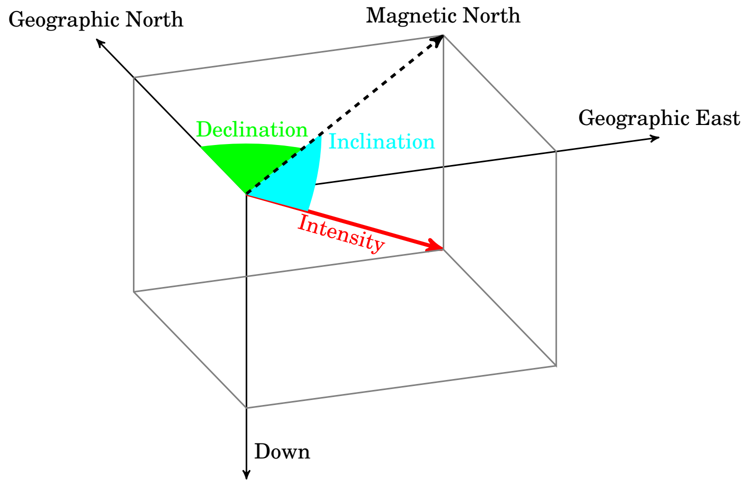

Figure 2.10: *Geomagnetic field coordinate system with declination, inclination and intensity nominators*

the center of the Earth and tilted from the Earth's rotational axis by 9.6° as shown in figure 2.8, with the geomagnetic north pole being technically a magnetic south pole and vice versa [McElhinny and McFadden, 1998].

Due to this shape of the geomagnetic field, the magnetic field lines are oriented in parallel to the surface at the equator and become more and more dipped towards the poles, eventually becoming vertical. The amount of dip is defined as the *inclination*. Due to the fact, that geomagnetic and geographic north are not identical, there is an offset between the magnetically observed north direction and true north, called *declination*, depending on the location on the Earth's surface. Furthermore, the intensity of the the geomagnetic field is increasing towards the poles, since the magnetic field lines are becoming more dense, resulting in higher magnetic flux density. The magnetic flux density at the equator is roughly $30\,\mu\mathrm{T}$ compared to $60\,\mu\mathrm{T}$ at the poles. In Bremen, Germany it amounts to $49.53\,\mu\mathrm{T}$ with a declination of $2°30'9''$ east and inclination of $68°5'14''$ down for June 2018. Figure 2.10 gives a visual description of the common nomenclature.

Observations have shown the limitation of the dipole approximation and therefore, apart from complex numerical models of the geodynamo [Christensen et al., 1998, Glatzmaier and Roberts, 1995], two analytical mathematical models are widely in use today, that describe the geomagnetic field much more accurately using 12-13th order spherical harmonic representations: the International Geomagnetic Reference Field (IGRF) introduced by the Internation Association of Geomagnetism and Aeronomy (IAGA) [Finlay et al., 2010] and the World Magnetic Model (WMM) of National Oceanic and Atmospheric Administration (NOAA), which is used for exam-

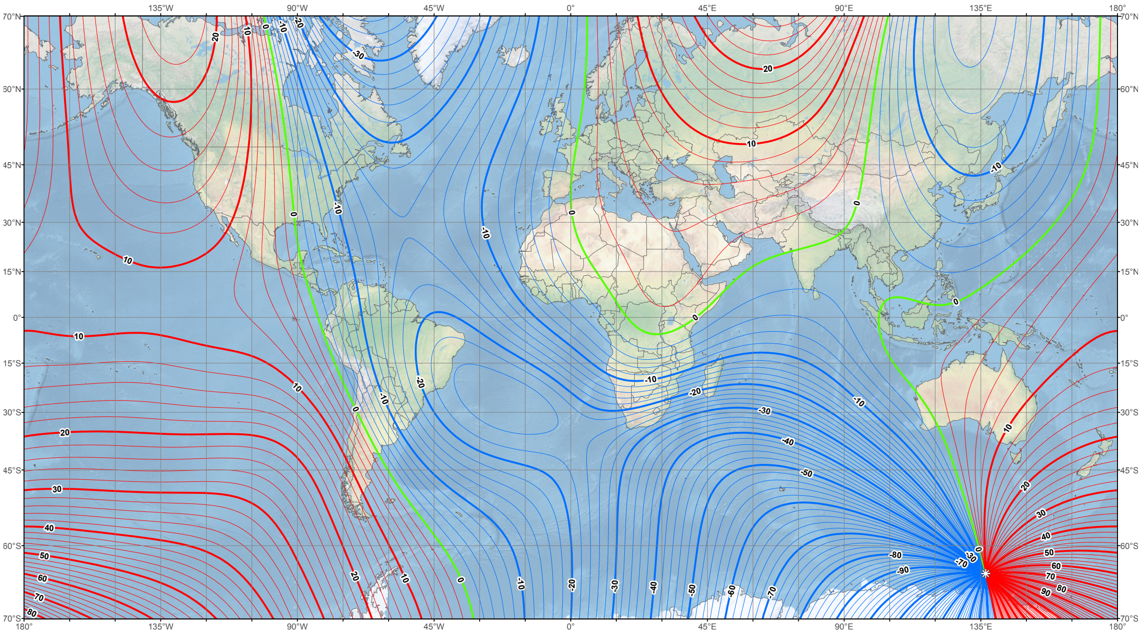

Figure 2.11: *WMM2150.0 main field declination map, mercator projection, contour interval: 2 degrees, red contours positive (east), blue negative (west) by NOAA/NGDC & CIRES*

ple as the standard model by the U.S. Department of Defense, the NATO and the International Hydrographic Organization (IHO) [Chulliat et al., 2015]. Both models continuously incorporate measurements from satellites monitoring the geomagnetic field and update their models every 5 years, with IGRF-12 and WMM2015.0 being the latest releases. The rolling releases of these models are incorporating more or better observations for example by the geomagnetic field observation satellites CHAMP or SWARM to increase the accuracy of the model, since the geomagnetic field is subject to continuous changes both on larger and smaller timescales, that affect every technique, that is using the Earth's magnetic field for navigational purposes [Maus et al., 2002, Sabaka et al., 2018].

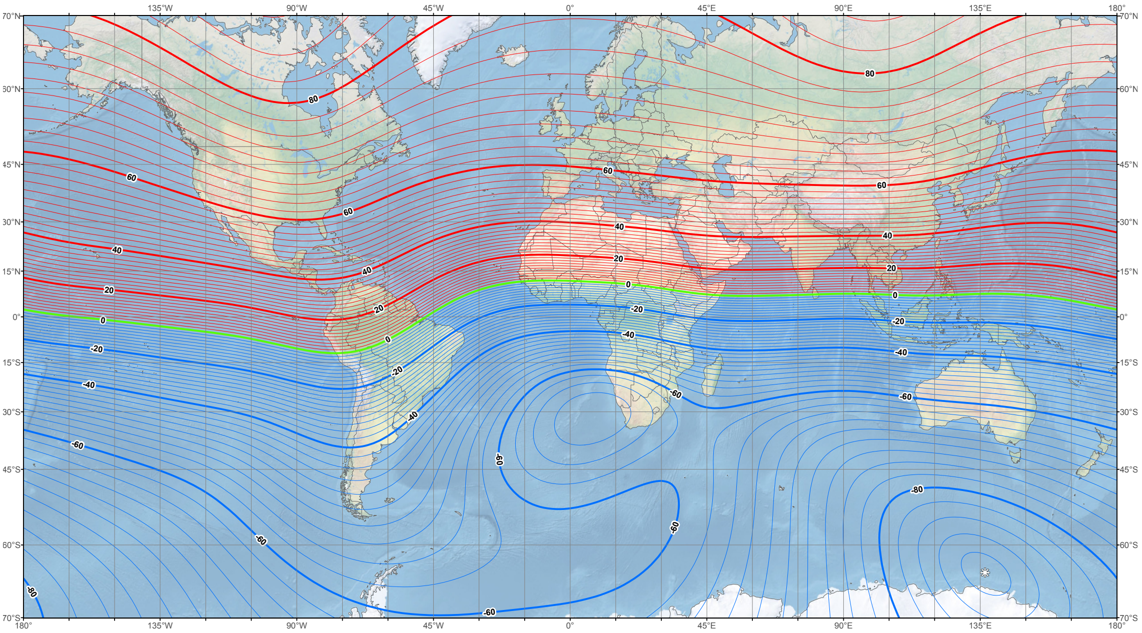

Figure 2.12: *WMM2150.0 main field inclination map, mercator projection, contour interval: 2 degrees, red contours positive (down), blue negative (up) by NOAA/NGDC & CIRES*

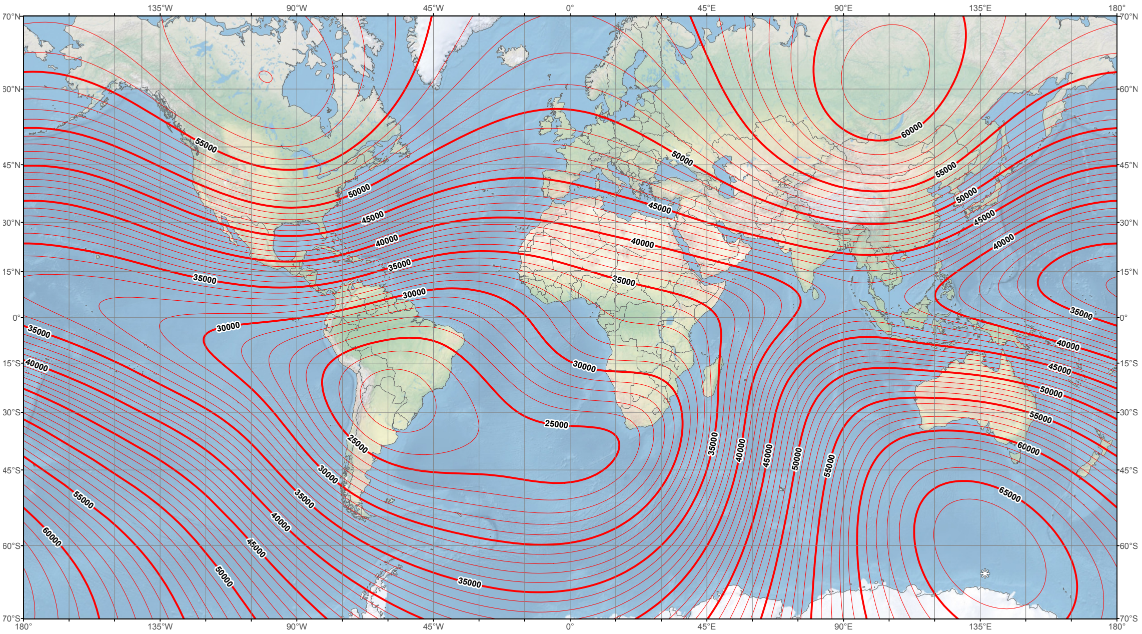

Figure 2.13: *WMM2150.0 main field total intensity map, mercator projection, contour interval:* 1000 nT *by NOAA/NGDC & CIRES*

Geomagnetic Field Main Contributors

The geomagnetic field has three main contributors, a) the outer Earth core, b) the Earth crust and c) activities in the magnetosphere.

Earth Core

By far the most significant contribution to the geomagnetic field is due to convection of electrically conducting fluids in the liquid outer Earth core, mainly consisting of molten iron and nickel heated up by the inner core. The planetary rotation generates a Coriolis force, which is forming the convection flows into rolls and thus establishing the main shape and intensity of the geomagnetic field (see figure 2.14). This mechanism is called the *geodynamo*. In average, the geodynamo contributes about $95\,\%$ to the shape and total intensity of the geomagnetic field. Due to the large contribution of the geodynamo, changes of this effect have a huge influence on the current manifestation of the geomagnetic field.

This rather strong, but slow change (compared to the changes in the magnetosphere, see below) are called *secular variation* and are happening in the order of years, rather than hours. Their influence is drastically, though, leading to a decrease of the overall dipole moment of $6.3\,\%$ over the last century and a drift of the geomagnetic north pole by $\approx 30\,\mathrm{km}$ per year, leading in Bremen, Germany to change in the declination of $0°8'26''$ east per year. Since these changes are well understood, the secular variation is already incorporated in the analytical WMM and IGRF models, so that declination, inclination and total intensity of the geomagnetic field can be derived for any latitude and longitude on the surface of the Earth for any point in time, at least for the validity period of these models of five years.

However, paleomagnetic research of strongly remanent magnetic material like magnetite showed, that there were times in the past, where the geomagnetic field was not at all predictable or well-structured, which is a prerequisite for the named models to work properly. These materials show clearly distinguishable periods of different intensity and polarity of the geomagnetic field in the past, which is also used to date sediments (Magnetostratigraphy). The average time period between total field reversals is roughly 450000 years, with an average polarity transition phase between 1000 and 10000 years. Yet such phases may be much shorter for a particular event: the duration of the last total field reversal approx. 780000 years ago (known as the *Matuyama-Brunhes* reversal) is assumed to have taken no longer than an average human lifetime [Sagnotti et al., 2014]. In such a transition phase, the geomagnetic field is not vanishing completely, but might be very unstructured, with multiple mag-

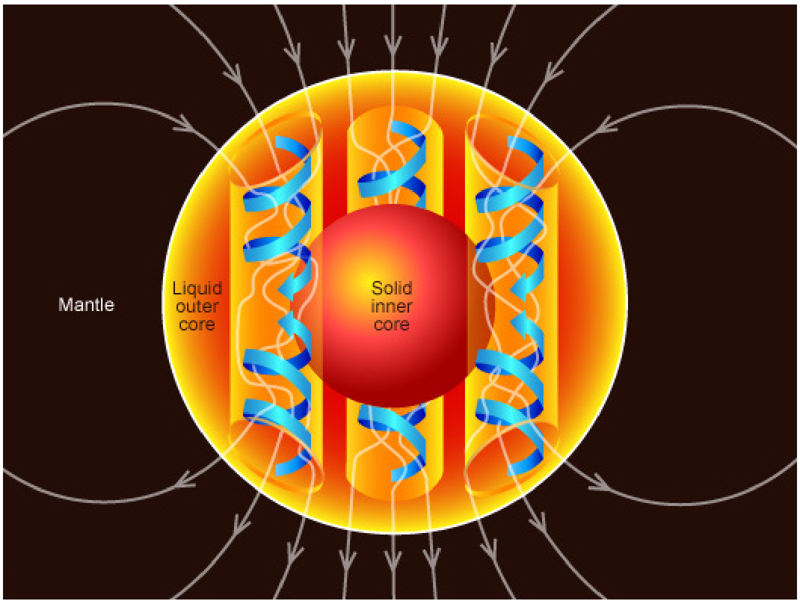

Figure 2.14: *Illustration of the geodynamo effect from convection flux in the liquid outer core of the Earth*

netic north and south poles, with changes up to 6° per day as shown by extensive simulations of the complex numerical models [Glatzmaier and Roberts, 1995]. Although the increasing drift of the magnetic north pole suggests that we may be at the verge of such a field reversal phase, we can assume the geomagnetic field to be stable enough and thus predictable by the WMM or IGRF model at least for the next few decades.

Earth Crust

The second most important contributor to the total geomagnetic field is remanent magnetization of the upper layer of the Earth crust, especially in ferrous minerals like ore deposits or iron-bearing volcanic basalt, which is, for example, quite common on the ocean floor. The temporal variation is quasi-static, varying only over geological timescales, but the spatial variation is significant, although minor in respect to the influence of the geodynamo effect. As depicted in figure 2.15, the most extreme anomalies arising from Earth crust remanent magnetization range from $-700\,\mathrm{nT}$ to $1200\,\mathrm{nT}$ in Germany, but are usually much smaller: Bremen, Germany for example has an Earth crust anomaly of $\approx -30\,\mathrm{nT}$ [Gabriel et al., 2010]. Compared to the total field intensity at that location of $49\,530\,\mathrm{nT}$, the contribution of the Earth crust amounts to less than $0.1\,\%$.

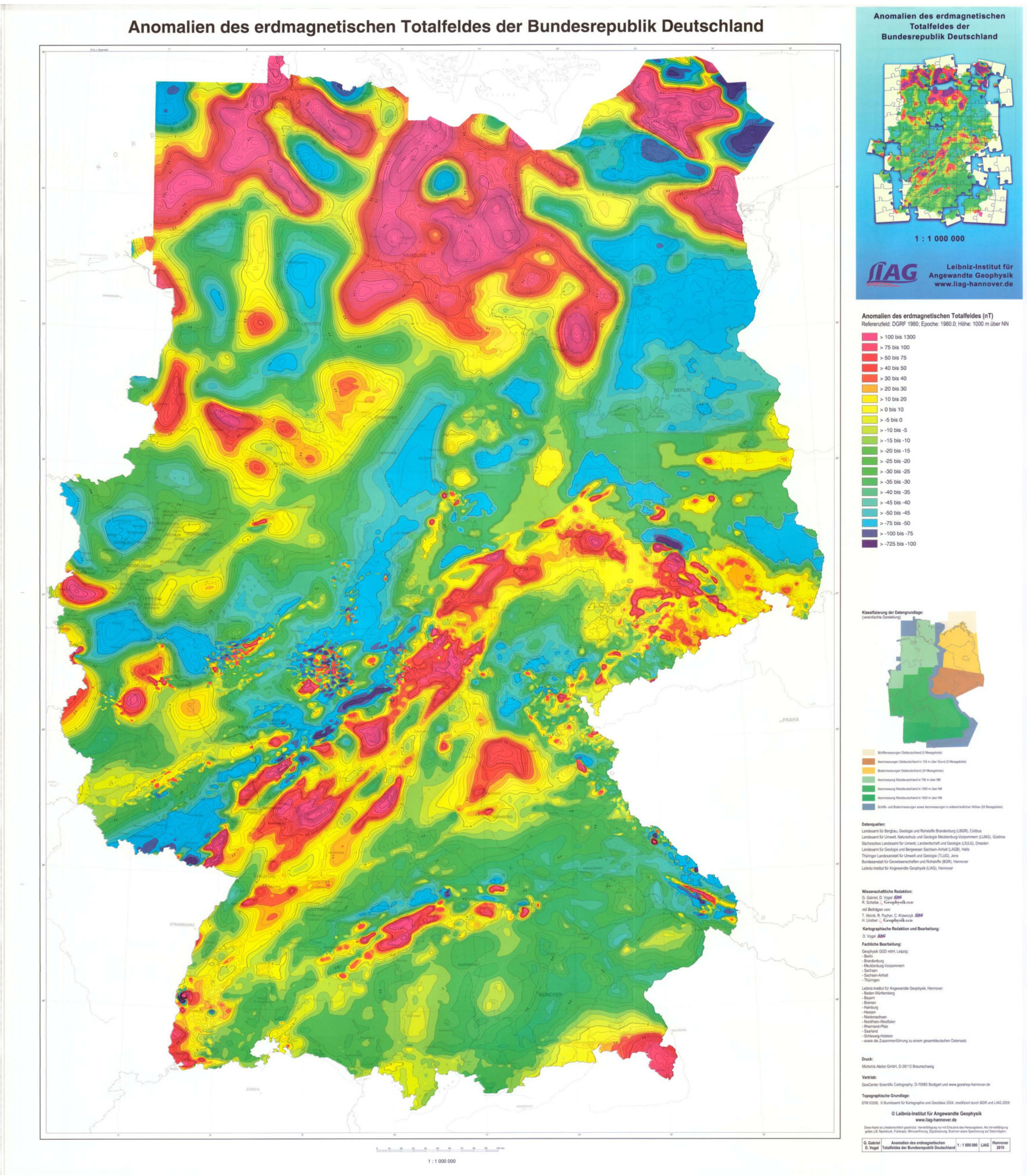

Figure 2.15: *Illustration of the static anomalies of the geomagnetic field due to remanent magnetization of the Earth crust in Germany [Gabriel et al., 2010]*

Magnetosphere and Ionosphere

Temporal variations over shorter time scales mostly arise from the third contributor to the geomagnetic field: currents in the ionosphere and magnetosphere mostly due to magnetized plasma of the solar wind (figure 2.16). During normal activity of the sun (solar-quiet variation (sq)), the variation shows a periodic characteristic over 24 hours, with its peak intensity at noon, when the solar wind hits the magnetosphere at the steepest angle. At this time of the day, the maximum sq-variation typically amounts to $\pm 19\,\mathrm{nT}$ which is approximately $0.04\,\%$ of the total intensity in Germany.

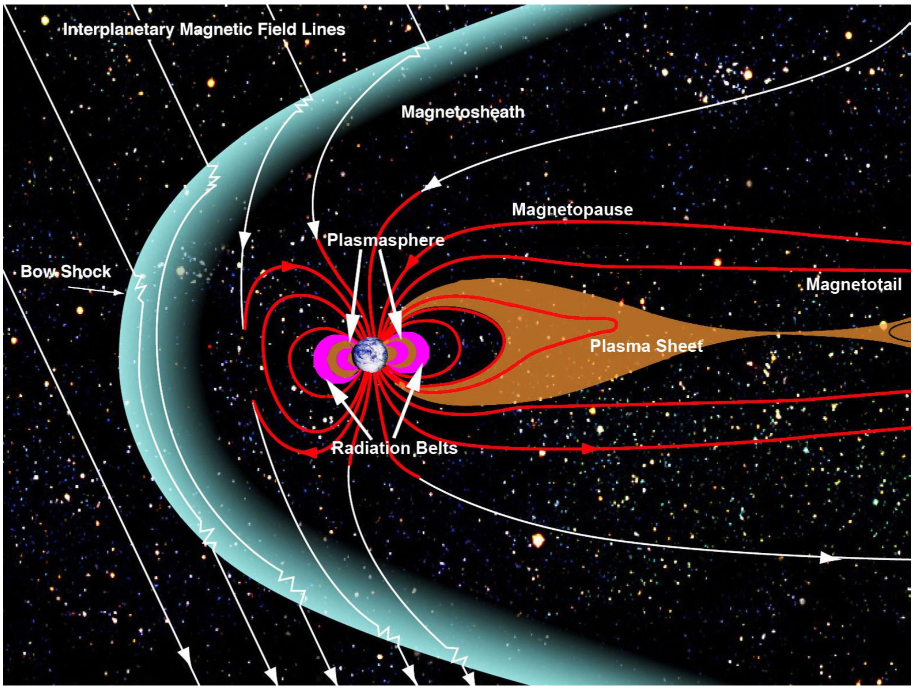

Figure 2.16: *The Magnetosphere of the Earth*

While mild geomagnetic storms may just lead to phenomena like aurora borealis, it must be noted that severe geomagnetic storms in the order of the Carrington Event from 1859 (the biggest ever recorded magnetic storm) can have catastrophic effects on electronic devices and electricity infrastructure. Although such an event could potentially lead to critical blackouts and financial damage in the trillion-dollar range due to geologically induced currents (GICs) in the shock phase [National Research Council, 2008], the overall effect on the geomagnetic field is rather small. Even in times of massive solar activity causing geomagnetic storms, for example due to a co-rotating interaction region (CIR) or a strong coronar mass ejection (CME), the effects on the direction and intensity of the geomagnetic field are orders of magnitudes smaller than the geodynamo effect: $44\,\%$ of geomagnetic storms are categorized as *weak*, with a change in the intensity of the horizontal component of the magnetic field between $30\,\mathrm{nT}$ and $50\,\mathrm{nT}$ ($\approx 0.2\,\%$ of the horizontal intensity at Bremen, Germany) and even storms categorized as *severe*, which make up $4\,\%$ of the total amount of storms are in a range $200\,\mathrm{nT}$ to $350\,\mathrm{nT}$ [Loewe and Prölss, 1997], which is about $1\,\%$ of the horizontal intensity at Bremen, Germany.

Geomagnetic Field Summary

To summarize, although there are shorter minor temporal variations due to activity in the magnetosphere and minor spatial variations due to remanent magnetization of parts of the Earth crust, the predominant contribution to the geomagnetic field by orders of magnitude is the geodynamo effect. This effect is changing only on large timescales and is analytically predictable by models like WMM or IGRF mentioned above, thus the Earth magnetic field can be considered sufficiently stable in the temporal domain for the purpose of this work.

Chapter 3

State of the Art

Navigation usually consists of the three major iterative parts: 1) localization, 2) finding an optimal path or trajectory to the goal and 3) trajectory following, including obstacle avoidance and compensating for external interferences. Especially localization has been a prominent research topic in robotics for decades and has been called the most fundamental challenge for autonomy in mobile robotic systems [Cox, 1991, Thrun et al., 2005].

3.1 General Localization and SLAM

The capability of mobile robotic systems to get from point A to point B efficiently, and also to know when the goal is reached, goes hand in hand with the availability of a model of the current environment (a *map*).

Both localization in a known map as well as mapping the environment with a known pose have their own challenges, but the most difficult and quite common case is, that both pose and map are unknown and have to be established at the same time. This problem is the well-known problem of *Simultaneous Localization and Mapping (SLAM)*, first coined that way by [Durrant-Whyte et al., 1996]. A wide range of research has been conducted in that area, especially fusing odometry and Inertial Measurement Units (IMUs) with vision or lidar-based sensory input, like FastSLAM [Montemerlo et al., 2002, Montemerlo and Thrun, 2007], 6D SLAM for large outdoor environments [Nüchter et al., 2007] or RGBDSlam [Endres et al., 2012], often based on probabilistic approaches like Extended Kalman Filters, Particle Filters or a mixture of both, like the Rao-Blackwellized Particle Filters (RBPFs) introduced by [Doucet et al., 2000]. A promising approach to overcome the shortcomings of having to rely on sensory input in the visual spectrum from cameras or lidars was presented in [Schwendner et al., 2014a], using data relating to the body of a robot, at the border of internal and external data (EmbodiedSLAM). In recent years, graph-based approaches to solving the SLAM problem have gained a more and more prominent role. Approaches like GraphSLAM [Thrun et al., 2005, Chpt. 11], GMapping [Grisetti et al., 2007] or g2o [Kümmerle and Grisetti, 2011] represent all poses and measurements of the past as vertices in a graph, which are connected by probabilistic pose constraints. Consecutive poses are constrained by the probabilistic motion model of the robot, whereas different measurements of the environment are constrained by their respective measurement models. At specific times, the graph is optimized to relax the constrained connections, thus producing a globally consistent map and robot pose history.

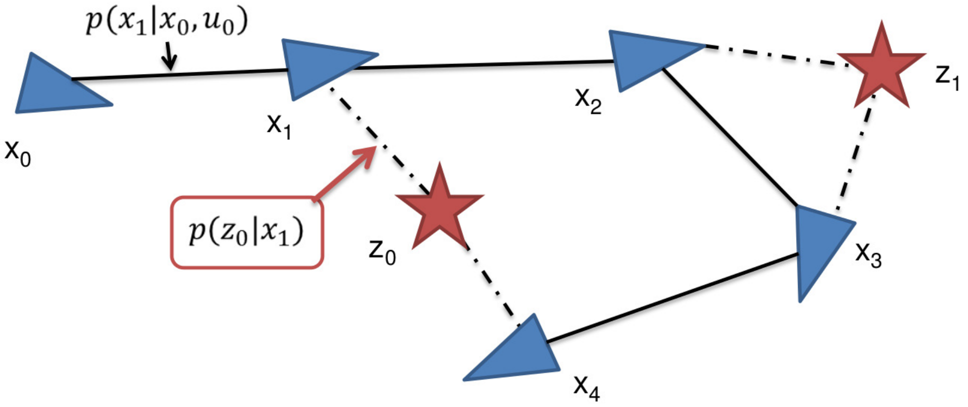

Figure 3.1: *General principle of graph-based SLAM approaches. All states* $x_0 \dots x_n$ *(blue triangles) and measurements* $z_0 \dots z_n$ *(red stars) are kept in the graph and constrained by their respective probabilistic models. Relaxation of the graph then produces the most globally consistent pose history and map*

Independent of the SLAM backend, that performs the more generic probabilistic optimizations, all of the mentioned approaches have to apply specific pre-processing of the sensory input, since the position of a robot usually cannot be directly observed, but has to be inferred from noisy or fragmentary sensor data. [Oehmcke et al., 2017] are describing an approach using Recurrent Neural Networks (RNNs) to handle such data loss in the case of marine sensor failures in harsh environmental conditions. Apart from the focus on visual perception, nearly all currently established robot localization techniques are heavily relying on IMUs, consisting mainly of gyroscopes and accelerometers to determine orientation. But as discussed in the motivational chapter 1.1 of this work, visual sensors may fail in demanding environments and magnetometers measuring the geomagnetic field are currently only used to correct heading drift IMUs, if used at all.

3.2 Magnetic Field Localization

To overcome the problems of drift in odometry based localization of cars, [Xu et al., 2006] propose the usage of discrete magnetic markers deployed in the roads in conjunction with a so-called 'magnetic ruler' consisting of 13 anisotropic magnetoresistance (AMR) sensors mounted to the front bumper of their car (see figure 3.2). For the authors, the weather independent nature of the magnetic field is the main advantage of using magnetometers in their scenario. They also elaborate and present data on the main drawback using magnetic artificial markers: Although they use one of the strongest permanent magnet materials available commercially (Neodymium Iron and Boron (NdFeB)) with a field strength of nearly 10 000 G near the surface, the strength drastically drops with the distance to less than 6 G at distances over 180 mm. The authors present a simple magnetic dipole model that they integrate with a nonlinear measurement model to be used in an Extended Kalman filter (EKF). Their filter then estimates the lateral offset of the vehicle in relation to a prerecorded trajectory. The authors show the general applicability of their approach up to a sensor - magnet distance of 180 mm, but they also describe problems with external and internal magnetic field disturbances, that would need to be dealt with in the future.

Figure 3.2: *'Magnetic Ruler' from [Xu et al., 2006] attached to a test vehicle for lateral trajectory offset estimation using artificial magnetic markers*

[Cole, 2005] describes the idea of using magnetic fields for mobile robot navigation in the sense of a reactive turn left/turn right homing behavior in the presence of an artificial alternating electromagnetic field. The field is created by a device that radiates an alternating electromagnetic field with constant amplitude and frequency of 8.8 Hz. The robot then contains three orthogonal loop antennas and due to Faraday and Lenz's laws, the changing electromagnetic field induces currents in the loop antennas proportional to the field strength in the respective axis. Depending on the measured strength in the two orthogonal axes in the plane where the robot moves, the robot corrects its path either to the left or the right, finally homing towards the device that emits the electromagnetic field (see figure 3.3). The author describes his system as a simple remote control direction device, the robot has no localization capabilities and is subject to local electromagnetic noise distortions.

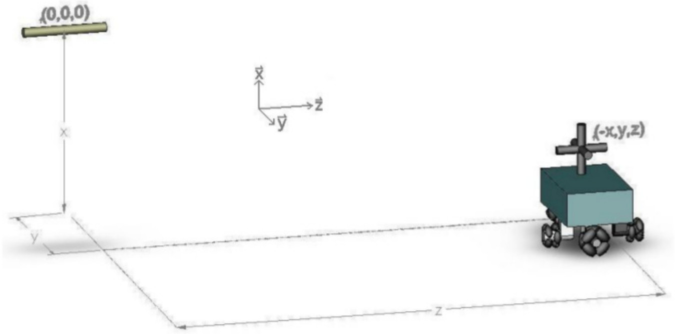

Figure 3.3: *Homing system from [Cole, 2005] using a mobile robot with orthogonal loop antennas and a transmitter generating an alternating electromagnetic field*

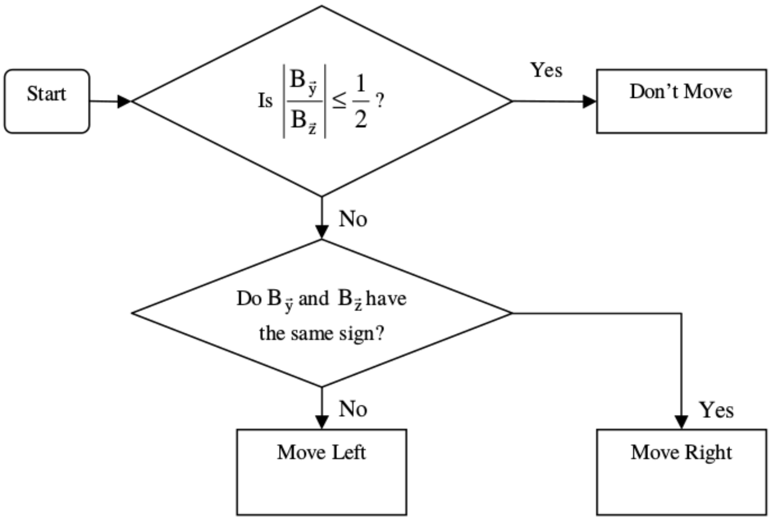

Figure 3.4: *Simple homing behavior of a mobile robot in the presence of a generated and known electromagnetic field [Cole, 2005]*

One of the first to describe the idea of explicitly using the ambient magnetic field for localization purposes apart from ordinary compass/heading applications were [Vissière et al., 2007]. In their conceptual work, they describe the idea to use magnetic field distortions (figure 3.5) in order to reduce drift in low-cost IMU-based localization estimation for military operations in urban areas, where GPS will most likely be not available and also vision-based approaches may fail due to dust or smoke. The work stresses the relevance of using magnetic field disturbances to improve position estimation in future works, but also presents preliminary results of drift elimination in a rail-based (1D) setup using an Extended Kalman filter. The work relies on some strong assumptions on the nature of the magnetic field though, like constant field strength changes and a totally stationary field with negligible other disturbances.

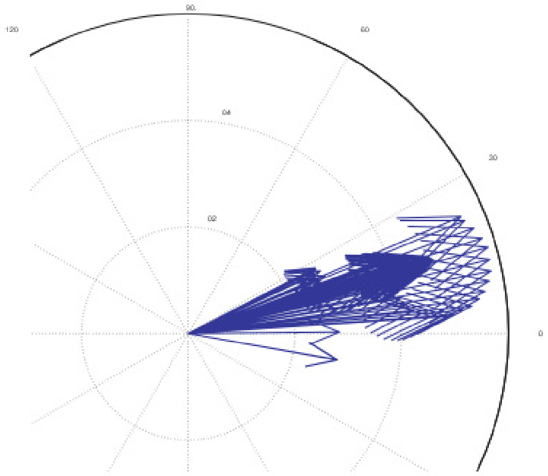

Figure 3.5: *Heading variations of (projected) magnetic field during 2.4 m horizontal displacement in a business building from [Vissière et al., 2007]*

[Vallivaara et al., 2010] propose a SLAM method utilizing local magnetic field anomalies in office environments to enhance low-cost robotic vacuum cleaners to allow for more sophisticated navigation to avoid overcleaning. They present a proof of concept for 2D map building (figure 3.6) in a simple one-room laboratory environment with an area of $5 \times 5\,\mathrm{m}$ using magnetic field strength readings and odometry information combined in a particle filter to overcome the cumulative error of standalone odometry. Their work is based on random movement on the robot and the strong assumption, that the magnetic field in the unvisited vicinity of single measurements can be modeled independently by Gaussian processes for each of the three orthogonal components of the magnetic field. They give no qualitative or quantitative result analysis, but claim that they were able to produce geometrically consistent maps in 19 cases out of 20. The magnetic field is considered static in time and disturbances introduced by the robot are neglected.

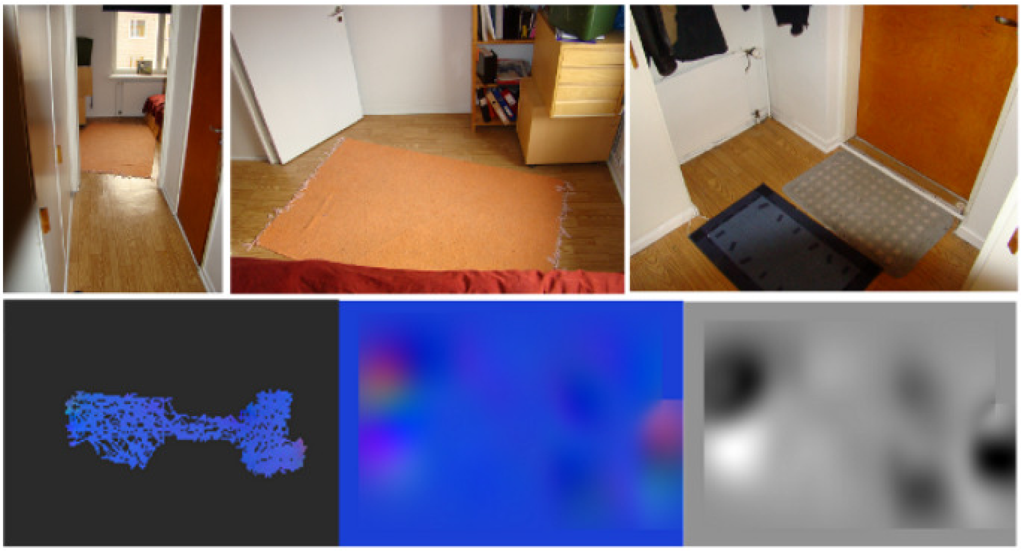

Figure 3.6: *Magnetic maps generated in an appartment by [Vallivaara et al., 2010]. x, y and z component RGB map (bottom middle) and magnetic field norm map (bottom right) showing significant features near steel radiators.*

[Rahok et al., 2010] describe a method to utilize the magnetic field of three pre-recorded trajectories to reactively follow the middle trajectory in subsequent runs with a robot (see figure 3.7). This virtual follow-the-wire method avoids the deployment of infrastructure, e.g. digging trenches for electromagnetic guidance wires for repetitive path-following applications. The authors report problems of not being able to return to the desired trajectory once the mobile robot has diverged too far from the pre-recorded magnetic field in their database due to magnetic noise coming from their mobile robot, which they don't model nor are able to compensate for by mounting the sensor far away from the robot due to security restrictions while driving in areas heavily frequented by pedestrians.

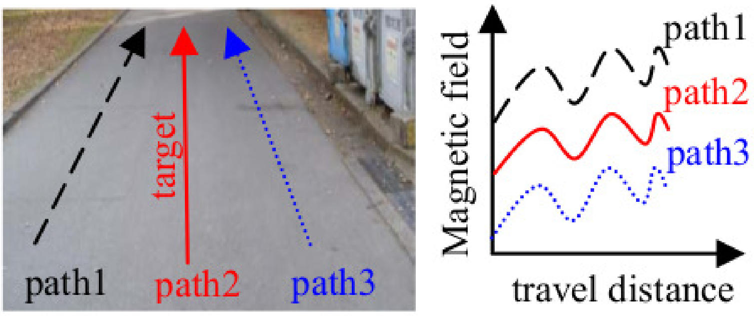

Figure 3.7: *Illustration of the reactive magnetic field based steering behavior by [Rahok et al., 2010]. The pre-recorded magnetic field values are used to keep the robot on the target path in the middle.*

During the work of the author of this thesis on ballast water tank inspection robots between 2009 and 2012, it became clear, that the commonly used sensors for robot localization are not feasible in such extreme conditions. No satellite navigation signals are available in the confined spaces of ballast water tanks, and mud and biological processes (e.g. algae) were rendering sensors like lidar and time-of-flight cameras useless due to absorption issues. Otherwise distinct geometrical features are changing fast in such conditions and were impeding the application of marker or feature-based localization techniques. In the light of the problems in such conditions of the commonly used sensors together with a poor odometry performance on a slippery rail, a magnetic field-based concept using probabilistic particle filter localization was developed and introduced [Christensen et al., 2011a], and preliminary results presented in [Christensen et al., 2011b], achieving a localization accuracy in the range of centimeters (see figure 3.8, 3.9), but limited to one dimension because of the robotic concept using a rail-based setup.

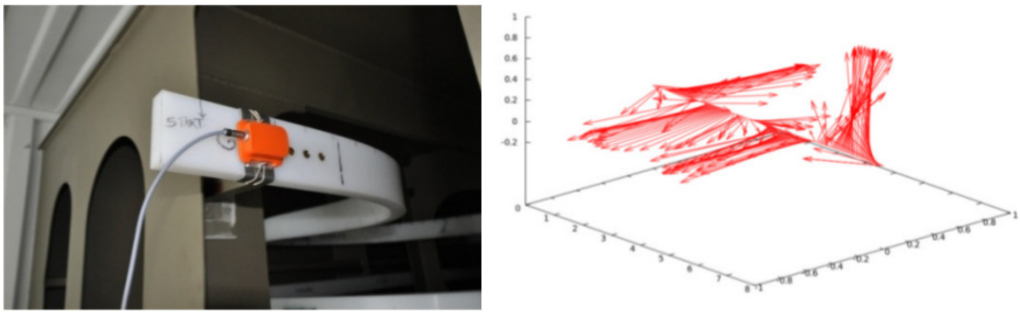

Figure 3.8: *Magnetic field based localization in a rail-based ballast water tank setup [Christensen et al., 2011a]. The magnetic field vectors are projected to 1D (right).*

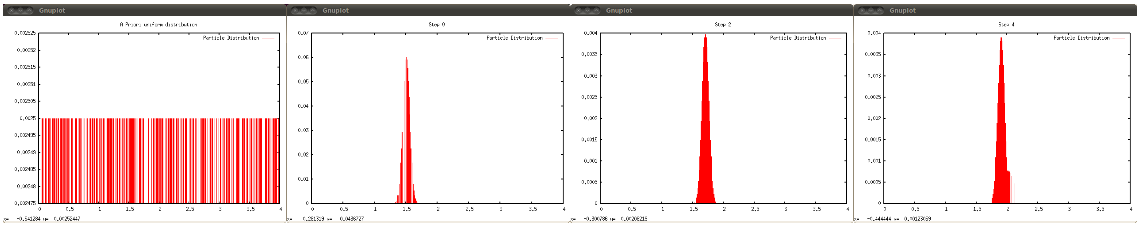

Figure 3.9: *Subsequent particle filter posterior estimation of the robot's position on a rail in a ballast water tank inspection setup.*

In 2012, parallel to the work carried out by the author of this thesis, [Grand and Thrun, 2012] also proposed the use of magnetic field disturbances as a signal rather than noise for localization purposes. In their preliminary work using the build-in magnetometers of smartphones, the authors demonstrated, that considerable improvements in positional accuracy compared to WiFi-based localization methods can be achieved. They, too, are applying a particle filter to estimate the position given an a priori magnetic field map. As visible in the results, the authors are not applying proper error-models to the used low-cost magnetometers in the handheld devices, which leads to strong discontinuities in the maps, depending on the direction of movement during the recording of the magnetic field strength component (see figure 3.10). The authors name the necessity of accurate a priori magnetic field maps the main limitation of the approach. Also, due to the limited sensor quality in handheld devices, the authors rely only on the rotation-invariant strength component of the magnetic field.

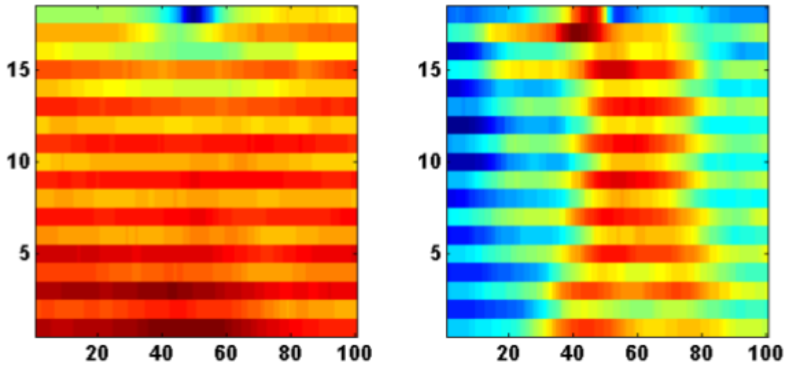

Figure 3.10: *Discontinuities in the generated magnetic field intensity maps of the x- and y-component using low-cost magnetometers with limited calibration and no error models [Grand and Thrun, 2012]*

[Robertson et al., 2013] are also proposing the usage of local magnetic field distortions, in their case to enhance pedestrian localization in indoor environments. The authors are adding magnetic field intensity measurements to their previously introduced *FootSLAM* approach based on human odometry (step measurements). In order to weigh the particles based on magnetic field strength measurements from magnetometers in the pedestrians shoes, they adopt a hierarchical map representation composed of uniformly sized hexagonal bins (see figure 3.11) and model the magnetic field strength in each bin as a Gaussian distribution, assuming that neighboring cells carry no information for the current cell. The authors propose their approach also for robots, but are assuming noise-free measurements and are using uncalibrated magnetometer data. Since humans in general don't distort the ambient magnetic field, this assumption holds true to a certain point in their setup of pedestrian localization, achieving a 2D localization error on the order of $10\,\mathrm{cm}$ to $20\,\mathrm{cm}$. The authors propose the usage of the full 3D vector for further work and not only the intensity, although that would mean that the magnetic field measurements are not rotation-invariant any more.

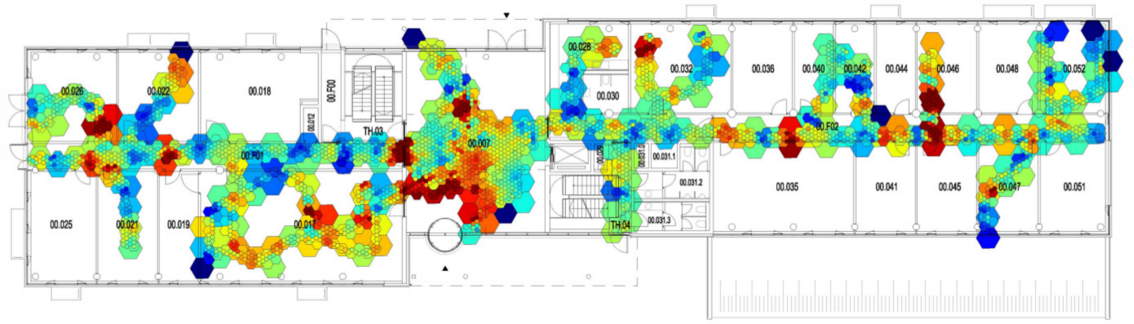

Figure 3.11: *FootSLAM map of a large office building annotated with hierarchical magnetic field intensity measurements in hexagonal bins [Robertson et al., 2013]*

[Akai and Ozaki, 2015] also base their localization method on a pre-collected magnetic field intensity map, which they gather in advance using a LIDAR-based RBPF-SLAM on a mobile wheeled robot. Similar to the work by [Robertson et al., 2013], they are dividing the magnetic field into grid cells and use a particle filter for localization (see figure 3.12). Rather than solving the full SLAM problem, the work focuses on efficient magnetic intensity map building for large scale indoor environments modeling the magnetic field intensity for each cell as a Gaussian process (figure 3.13). The authors make a strong simplification though, by assuming the intensity of each axis to be independent and learning a model for each one individually, basically losing the rotation-invariant property of the magnetic flux density, but neglecting the meaning of *direction* inherent to the magnetic vector field. The authors describe an error accumulation problem in their experiments, but since a similar trajectory for collecting the magnetic field map and the localization evaluation is driven, the method still works, with a reported estimation error of approximately $1\,\mathrm{m}$.

[Jung et al., 2015] describe in their work a method of solving the indoor SLAM problem using a pose graph optimization approach, utilizing the local magnetic field. They propose to add two types of constraints based on 3D magnetometer measurements, one for local heading correction and one for loop closures. The first uses the property, that the magnetic field vector represented in a global frame should remain stable when the robot is turning without translating (magnetic pivoting constraint). For the loop-closing constraint, the authors are using a sequence of magnetic field measurements and apply sequence-based matching techniques to overcome spatial similarities of the magnetic field. During evaluation with a wheel based robot, the authors relied on these sequences being recorded while the robot is moving strictly linear, since they experienced magnetic field inconsistencies (they call *magnetic fluctuations*) while turning with the robot, most likely due to distortions of the local

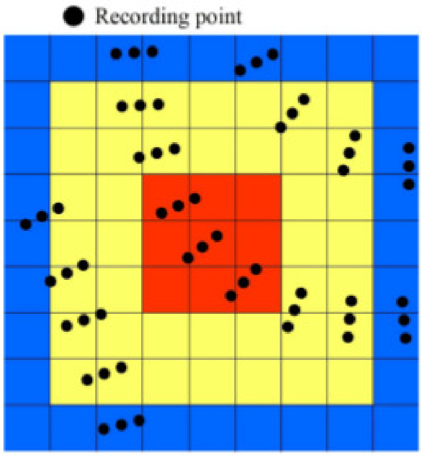

Figure 3.12: *Discrete magnetic intensity grid cell by [Akai and Ozaki, 2015], with recording points only in the yellow and red region contributing to the learned gaussian process for the red area*

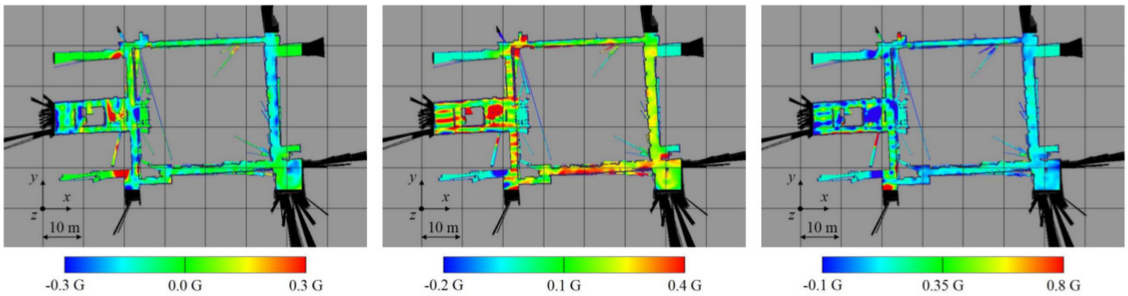

(a) Mean of B_x (b) Mean of B_y (c) Mean of B_z

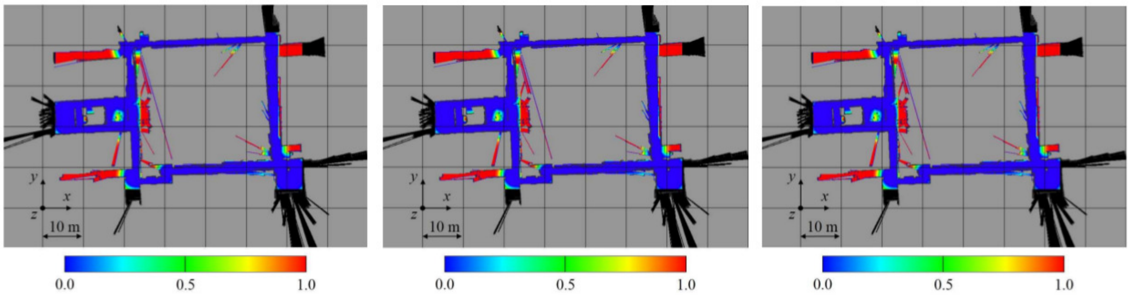

(d) Variance of B_x (e) Variance of B_y (f) Variance of B_z

Figure 3.13: *Separately learned distributions using gaussian processes for each intensity component of the magnetic field by [Akai and Ozaki, 2015], showing respective mean and variance of an indoor office environment*

magnetic field caused by the robotic system itself (see chapter 4 and 5 on system-immanent distortions). This further implies that the robot has to drive in the same direction (or the direct opposite) on a similar trajectory for loop closures to work. The authors comment, that they therefore recommend to augment their magnetic constraints with further sensor systems like laser range finders or cameras in the pose graph SLAM approach, but that under the mentioned restrictions in the application scenario, they were able to achieve a mean absolute trajectory error of $(0.28 \pm 0.19)\,\mathrm{m}$ against a reference path. Like [Akai and Ozaki, 2015], they are not using the direction component of the magnetic field directly, although they briefly mention the possibility to use a cosine similarity metric when comparing 3D magnetic field measurements, but eventually choose to use a Euclidian distance metric.

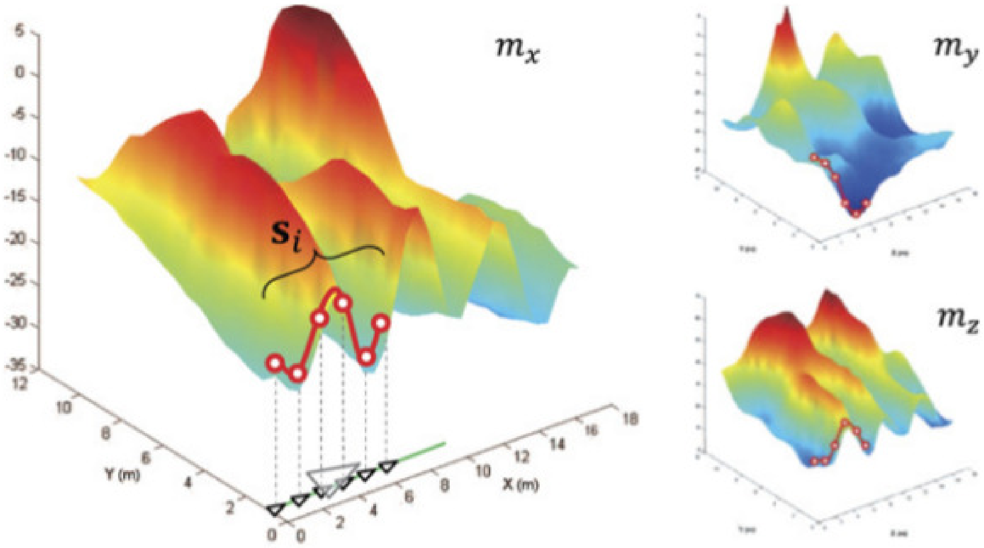

Figure 3.14: *Magnetic field intensity sequence constraint for pose graph SLAM approach by [Jung et al., 2015] for each magnetic field component separately*

Chapter 4

Ambient Magnetic Fields

In order to use the local distortions of the geomagnetic field for mobile robot localization purposes as intended in this work, the ambient magnetic field has to exhibit characteristics, that provide a sufficient amount of information for a specific application scenario. What may be considered *sufficient* in this sense will be dependent on the concrete task at hand, the spatial extent and the expected localization accuracy. Previous works in this area are strongly focussed on humans in office indoor environments, and the applicability for mobile robot localization in other environments remained vague as discussed in Chapter 3. It seems reasonable to postulate, that a certain amount of variation per volume from a uniformly distributed field will be required, along with a particular non-periodicity to avoid ambiguity, again depending on the robotic task requirements. Therefore, this chapter will describe some exemplary robot application scenarios that have been assessed with respect to the encountered magnetic field characteristics and reason on the applicability of a magnetic field distortion localization approach in these scenarios.

4.1 Ballast Water Tanks

Ballast water is used to stabilize partially loaded or empty ships on the open sea. When needed, ocean or port water is pumped into special ballast water tanks (BWTs) to increase the mass of a ship. Because ocean water is typically contaminated with algae, plankton and other organisms, and due to the aggressive nature of salt-water, BWTs are often subject to serious bio-fouling and corrosion. The ballast tanks represent more than 40 % of the entire coated area on a vessel. They therefore need frequent inspection, cleaning, and repair. Until now, the maintenance of BWTs cannot be performed under operating conditions. Consequently, ship owners are forced to send their ships to dock inspection frequently, causing high costs in labor and ship downtime. On cruise vessels, BWTs are typically built in those spaces of a ship that cannot be used for other purposes. As a consequence, they are narrow, irregularly shaped, and badly ventilated. They are designed to be accessible to human workers, but are a dirty, unhealthy, and unpleasant workplace (see figures 4.1 and 4.2).

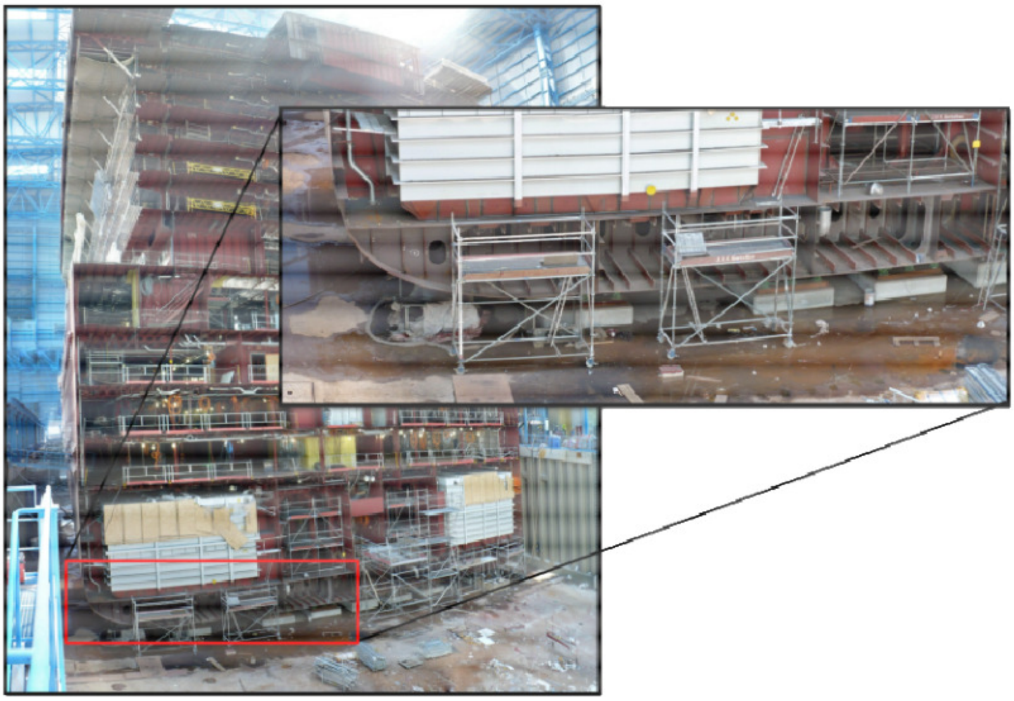

Figure 4.1: *Double bottom ballast water tank of a cruise liner at Meyer Werft Shipyard during construction phase*

Figure 4.2: *Possible ballast water tank environments for robotic inspection and maintenance*

Manual work in a BWT is a tedious task that carries potential short- and long-term health risks for the workers involved. Nevertheless, coating, cleaning, inspection and repair of ballast water tanks are still done manually. Automation of these processes is not feasible so far due to the complexity and the variability of current tank designs, as well as the limited flexibility of the currently available robotic systems. If robots were to take over the inspection, cleaning, coating, and repair of ballast water and other tanks and narrow spaces, this would greatly speed up the process and reduce the health risks for workers and ship crews. Using robots, shipbuilders, ship owners and class societies alike would also be able to considerably reduce the cost for inspection and maintenance. For an extended overview on BWT- or ship inspection and on possible robotic concepts see [Christensen et al., 2011a].

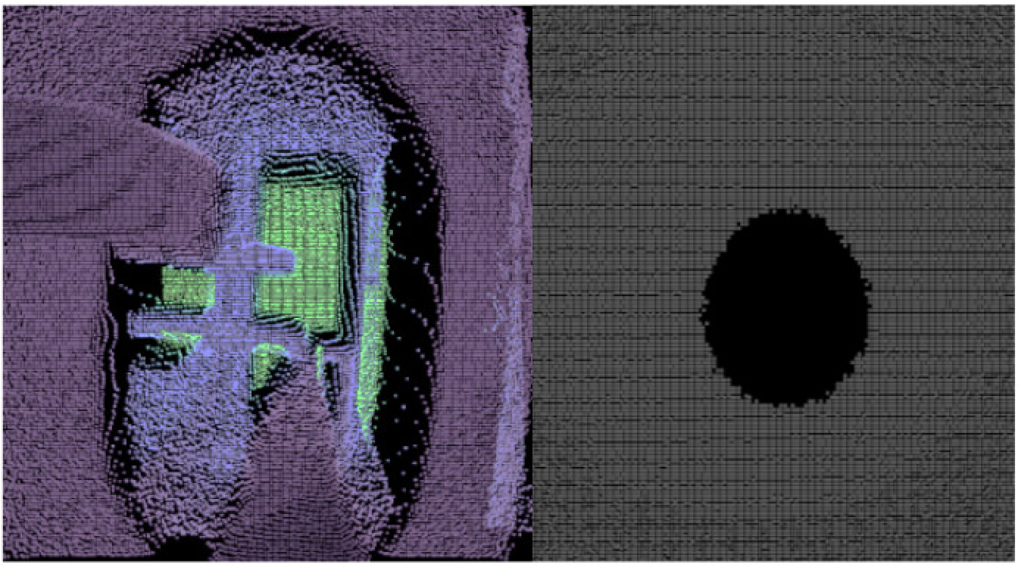

Figure 4.3: *PMD camera point cloud looking through a BWT manhole with extinction artifacts on sharp edges (left) and directly looking at flat surfaces (right)*

Since the narrow and contorted design is effectively preventing any remote-controlled robotic applications, any feasible robotic application scenario will have to feature autonomous behavior, at least to a certain degree. This inherently requires the capability of *localization* based on sensors that can perform properly in such conditions as encountered in ballast water tank environments. Apart from the obvious non-functionality of GPS-based localization in these environments due to the massive steel barrier, [Christensen et al., 2011b] further describe the problems of typical exteroceptive sensors used for robot localization in these environments, like erroneous measurements near the sharp edges of so-called manholes or extinction and strong multi-path reflection artifacts on flat coated surfaces with cameras based on Time of Flight (ToF) or Photonic Mixing Device (PMD) sensors and laser scanners (figure 4.3). These problems are in most cases combined with a bad odometry of the robot, mostly due to slippage caused by moisture or dirt residue from the last floodings. Using magnetic field distortions for localization as described in this work may help counter some if not all of these problems, given that the magnetic field exhibits the required features like measurable variations of the flux density and temporal stability.

Multiple assessments of the magnetic field were carried out in a BWT testbed of $16.7\,\mathrm{m}^3$ with an installed plastic rail for rail-guided robotic inspection of $22\,\mathrm{m}$ over a period of two years. The construction is made of standard shipbuilding steel of $5\,\mathrm{mm}$ thickness with strong ferromagnetic soft iron properties and has 27 separate compartments on two floors connected with manholes. First measurements of the magnetic field were done manually by moving an IMU with a built-in 3 axis magnetometer on a non-magnetic slider by hand over the rail, to avoid any magnetic field distortions from the robot. Measurements were taken every $5\,\mathrm{cm}$ (figure 4.4). Later, to evaluate the temporal stability of the ambient magnetic field, multiple measurement runs were also carried out with the robot *Artis*, always with the same setup and static calibration of the magnetometer, but no noticeable changes of the magnetic field inside the test tank occurred.

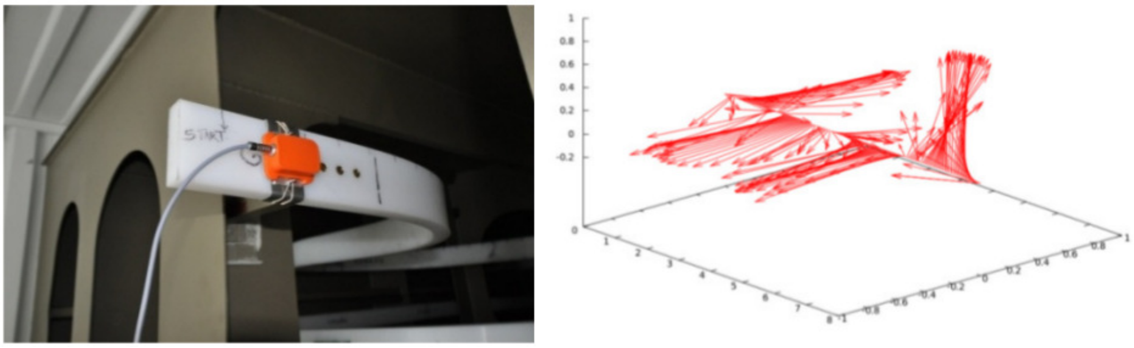

Figure 4.4: *Collecting magnetic field readings for the generation of a magnetic field map for localization purposes in a BWT testbed. The plot on the right shows the mangetic flux density vectors of the rail trajectory straightened out.*

Figure 4.5 shows the variations of the magnetic field during a straight run on a rail through a BWT. The huge amount of soft iron steel leads to strong deviations of the geomagnetic field in every axis of the magnetometer, especially when passing through manholes or crossing sections, where the rail was attached to the BWT by means steel fasteners.

When looking at the combined magnetic field flux density (the length of the magnetic field vectors or strength, see Section 2.1) across the rail segment in figure 4.6, the change in strength is also significant, ranging from a minimum of $13.65\,\mu\mathrm{T}$ to a maximum of $38.37\,\mu\mathrm{T}$, with a mean value of $23.82\,\mu\mathrm{T}$. The low mean value (less than half of the expected geomagnetic field in Bremen, Germany) indicates a strong shielding effect of the surrounding steel container, but is still in the same order. Looking at the distribution of the strength readings, there is no prominent singular mode around

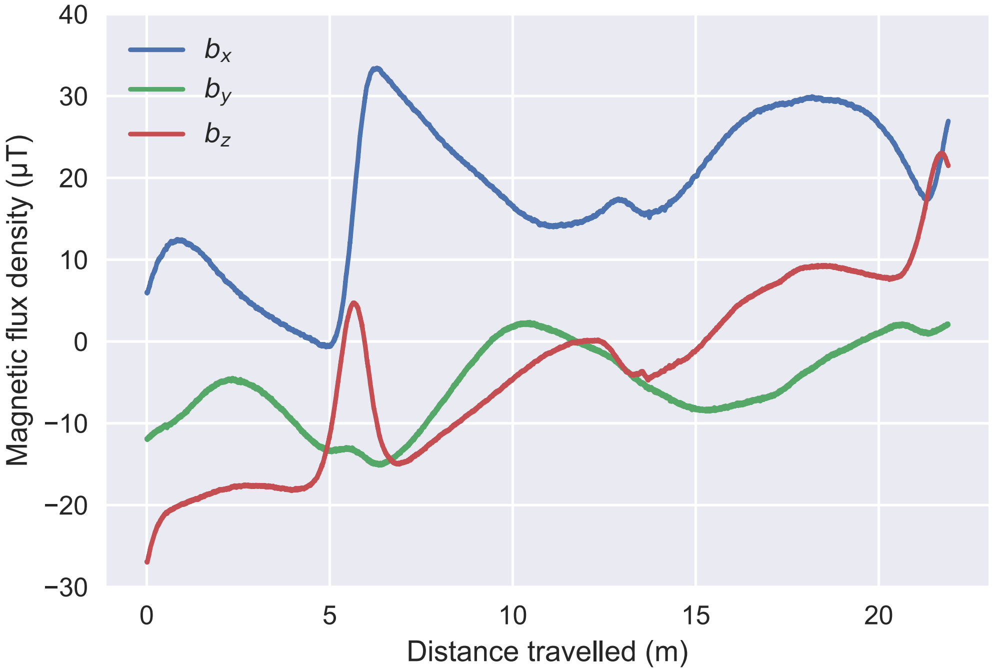

Figure 4.5: *Magnetic field variations per 3D component during a straight run on a rail through a ballast water tank*

which the magnetic field strength deviates.

Although it is possible to have strong changes in the strength component without a change of the field direction, in this case figure 4.7 shows, that the direction of the magnetic field is also changing dramatically during the same run on a rail through the BWT. To visualize just the change in direction, the measured magnetic field vectors are normalized to unit length and projected onto the unit sphere, each rooted in the origin of the sphere. No change in the direction of the field measurements would thus lead to just one fixed point on the unit sphere, whereas continuous changes in the direction would lead to a defined path on the unit sphere, as it is the case with the BWTs.

Given the significant changes of the magnetic field both in strength as well as the direction with distinct features, such structured artificial environments consisting of a huge amount of soft iron material like shipbuilding steel seems very well suited to provide enough information for magnetic field-based localization.

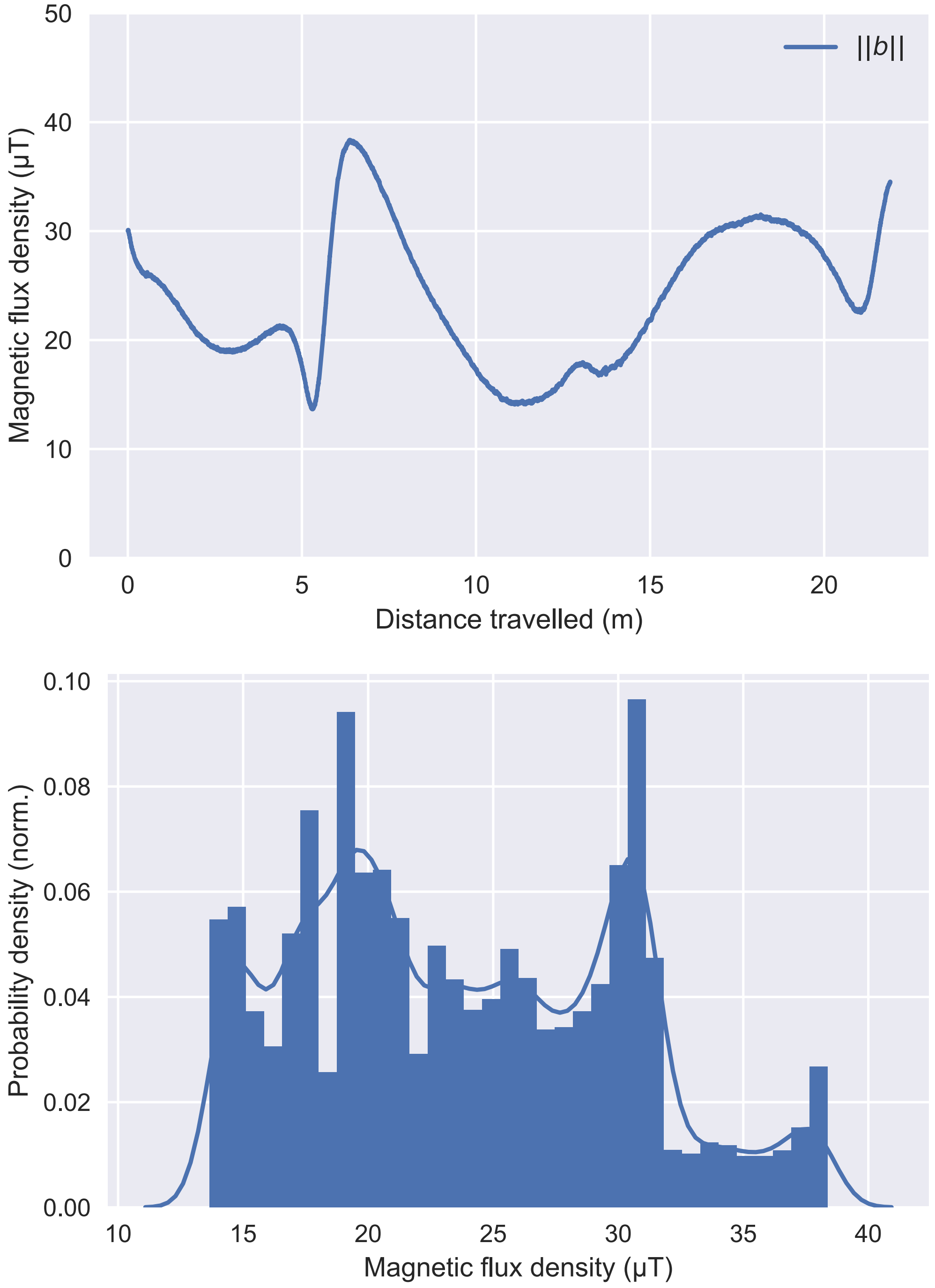

Figure 4.6: *Combined magnetic field strength variations during a straight run on a rail through a ballast water tank and the corresponding field strength distribution*

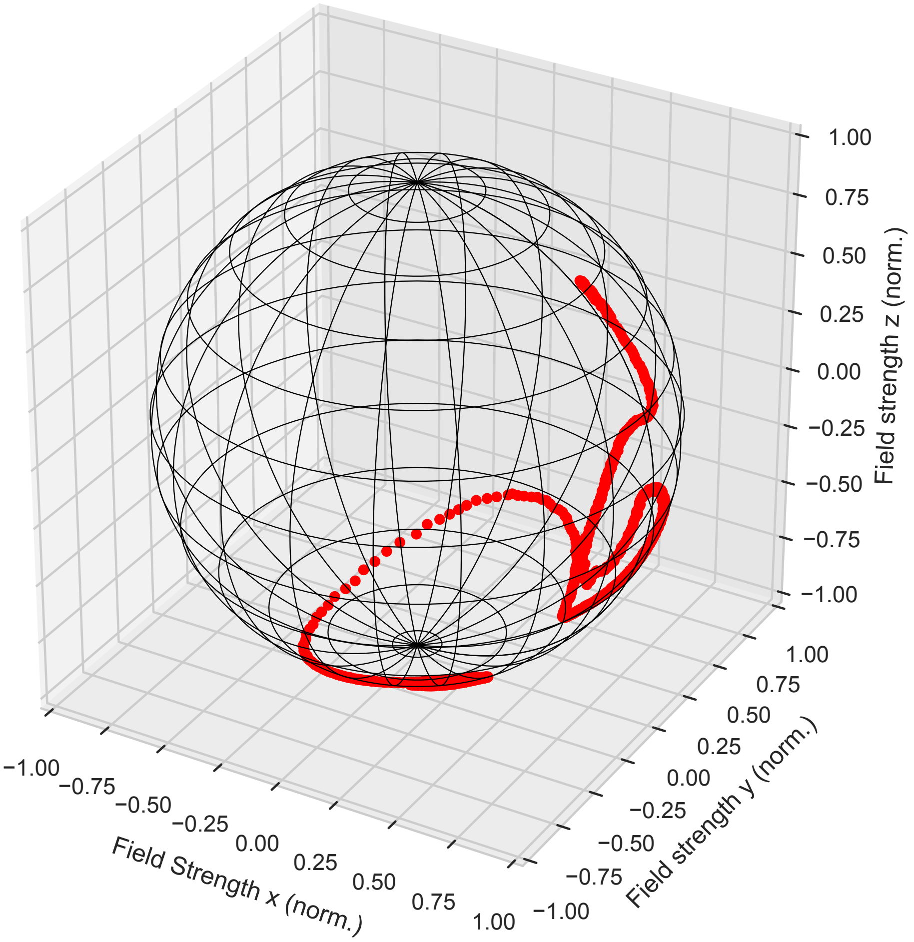

Figure 4.7: *Magnetic field direction change during ballast water tank rail run*

4.2 Office Environment

Because of their typically easy-to-access nature, office environments are one of the most common test scenarios for small robots. For magnetic field localization, though, there are more reasons why office environments are not only convenient, but an appropriate test scenario: localization in buildings is challenging, because of the limited or mostly non-availability of global navigation satellite systems (GNSSs) like Global Positioning System (GPS), GLONASS or Beidou, the de-facto standard for most outdoor localization applications. Furthermore, most common multi-floor office building architectures depend on long massive steel girders in the walls and reinforced ferroconcrete for the floors. Such construction material can be expected to exhibit strong static deviations of the earth magnetic field.

Figure 4.8: *Magnetic field sampling in typical office environment*

For the purpose of this work, data of an office environment was gathered using a special setup avoiding ferromagnetic material, that may hamper with the ambient magnetic field measurement procedure. A lightweight small plastic sled carrying an IMU containing a calibrated 3 axis magnetometer was set up, which was attached to a supporting rope and pulled in a uniform motion by a plastic fishing line on a motorized reel (see figure 4.9). The required power-supply battery was mounted $\approx 20\,\mathrm{cm}$ away from the sensor and the whole sled sensor setup was statically calibrated (for static calibration procedures see Section 6.2).

The isolated components of the magnetic field b_x, b_y and b_z are showing again significant changes of up to $30\,\mu\mathrm{T}$ (figure 4.10). This is also reflected in the variation of the

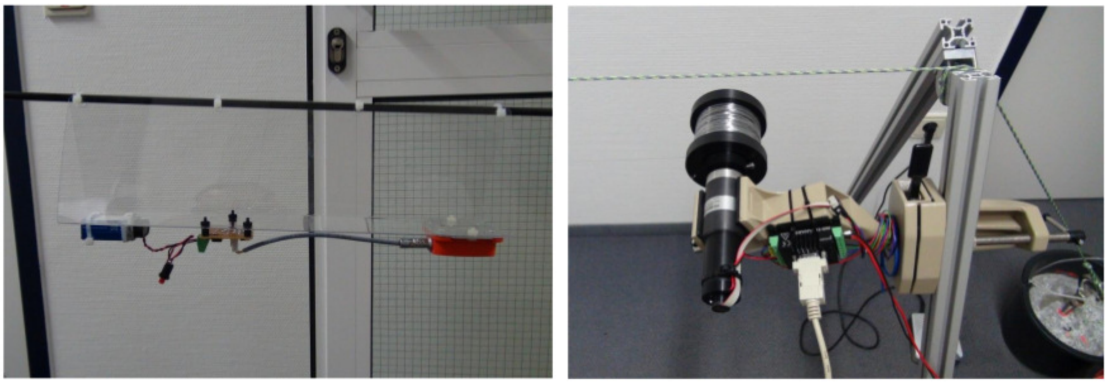

(a) *Measurement sled* **(b)** *Reel for steady pulling*

Figure 4.9: *The office environment magnetic field measurement setup avoiding ferromagnetic material to prevent disturbances during data aquisition*

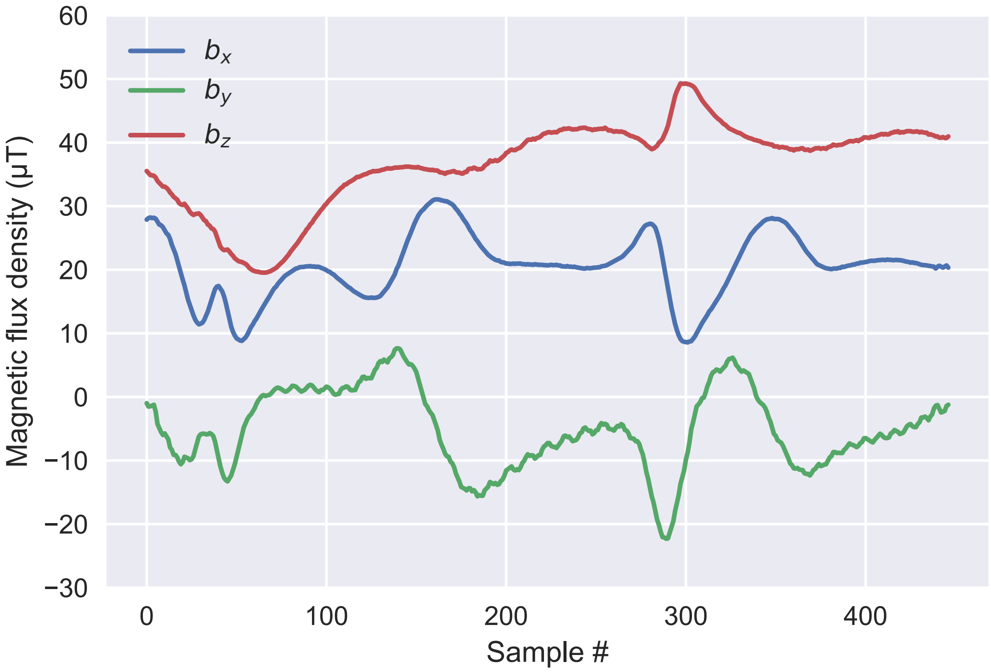

Figure 4.10: *Component-wise magnetic field variations of an office floor environment (straight run RH5, no. 1)*

absolute magnetic field strength along the office floor, but looking at the distribution over the strength range, one can see an accumulation around $47\,\mu T$ (figure 4.11), reflected also in the median value of that dataset of $46.28\,\mu T$. While the median value is therefore quite close to the expected geomagnetic field strength of $49.46\,\mu T$ in Bremen on that day, the distribution shows a longer tail to the left with a significant amount of samples with lesser strength values $43.03\,\mu T$.

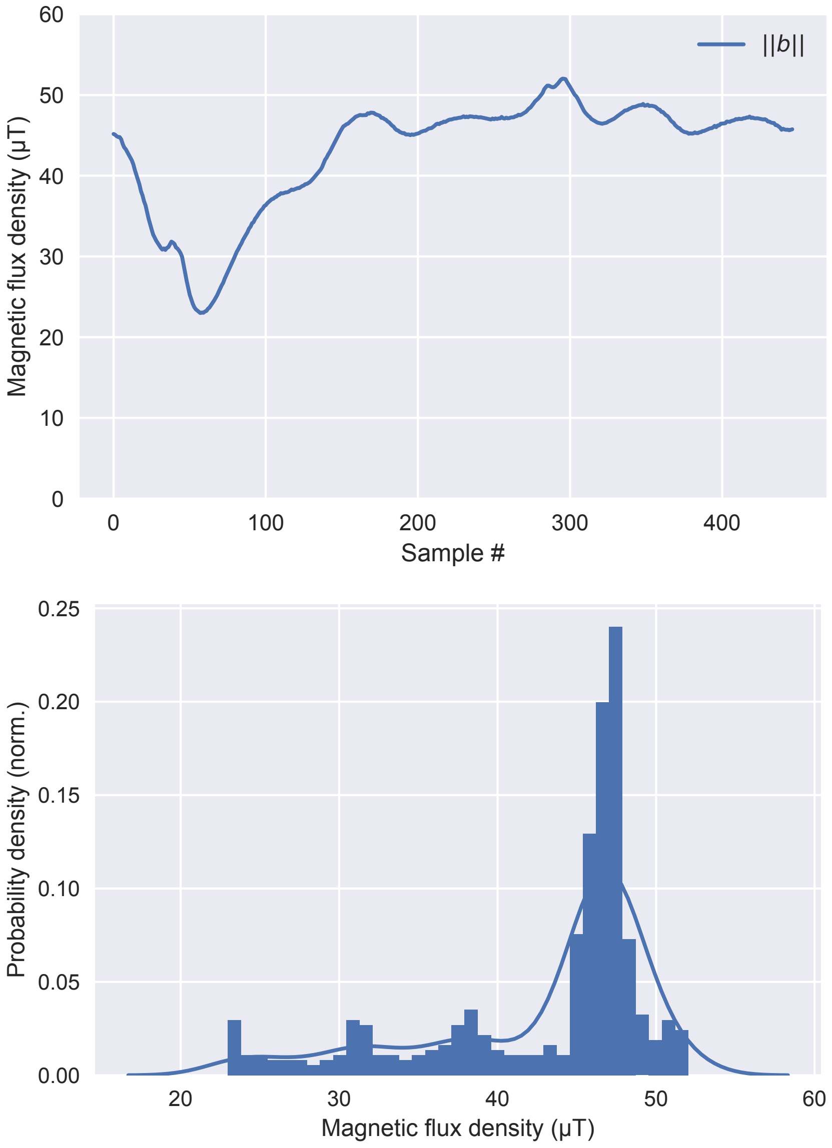

Figure 4.11: *Combined magnetic field strength variations during a straigth run through an office floor environment (straight run RH5, no. 1) and the corresponding field strength distribution*

A noticeable element of the office environment at hand were two strong pillars of reinforced concrete encapsulating a steel girder. When overlayed with the floorplan of the environment, the significant dents in the intensity correlate with the respective positions of the pillars (figure 4.12). This is a typical sign of the soft iron effect, that is expected from such material (see Section 2.2): the iron material provides a path of lower impedance for the magnetic field with increased magnetic flux density in the material, but corresponding lower flux density or strength in the vicinity of that object. A similar effect but to a lesser extend than with the steel girders is noticable in figure 4.12 when passing the steel door frames.

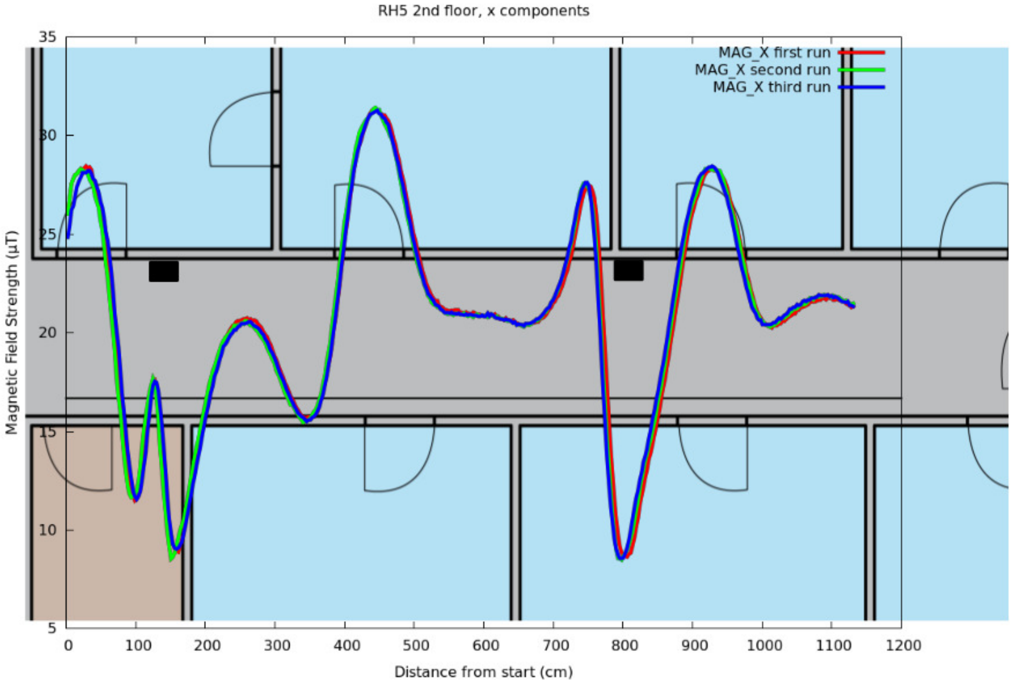

Figure 4.12: *Magnetic field X component variations overlaid on top of office floor plan (straigth runs RH5 no. 1-3)*

Concerning the deviations of the direction of the magnetic field in such an environment, the directions are much less spread out than for example in the ballast water tank scenario (figure 4.13). While having a strong effect on the strength, the direction of the field shows noticeable, but weaker deviations in the vicinity of the pillars along the path (figure 4.14).

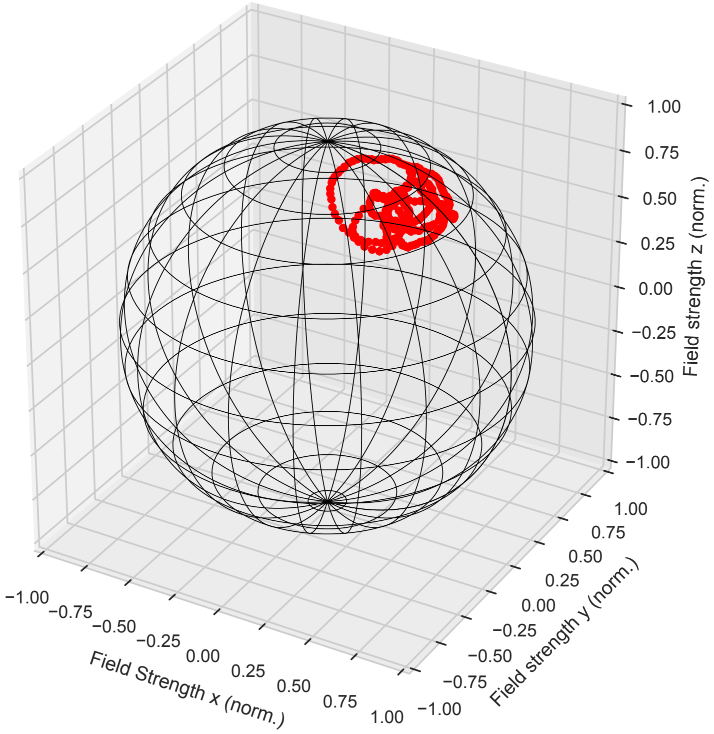

Figure 4.13: *Magnetic field direction change during straight office floor environment run (straight run RH5, no. 1)*

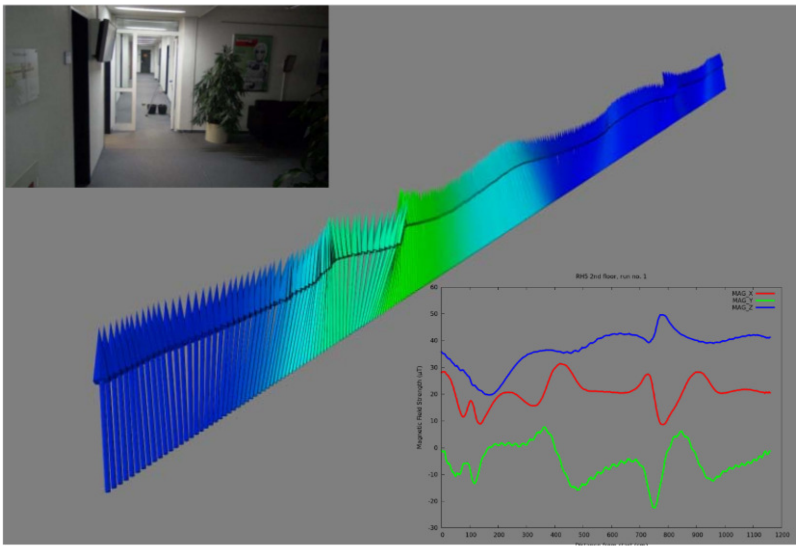

Figure 4.14: *3D rendering of magnetic field direction and strength variations along the office environment sampling trajectory*

4.3 Outdoor Cattle Grid

When testing robot navigation at the outdoor test track of the German Research Center for Artificial Intelligence - Robotics Innovation Center (DFKI RIC), a special challenge is to overcome a small canyon or trench by means of a cattle grid. A cattle grid can be quite easily crossed by wheeled vehicles like cars, but effectively prevent livestock from passing due to a traverse grid of tubes running across (figure 4.15). Planned mainly as a challenge for legged walking robots, it was quickly realized during testing of new navigational approaches, that often the localization solution degraded, just when trying to navigate over that difficult structure, due to IMUs providing bad pose estimates.

Figure 4.15: *A cattle grid on the outdoor testtrack at DFKI RIC*

Saturation of the accelerometers inside the IMU could be one problem, since crossing the cattle grid can lead to strong shaking motions of the robot and correlating vibration of the IMU. However, the main cause for localization degradation is anticipated to be strong magnetic field distortions at that area due to the steel construction. Therefore, data of the magnetic field across the cattle grid was gathered in the same way as in the office environment.

In terms of the single components of the magnetic field in the case of the cattle grid, one can directly see the magnetic flux density rising and falling quickly during the crossing, with strong amplitudes of up to 90 µT (figure 4.16) in a single component.

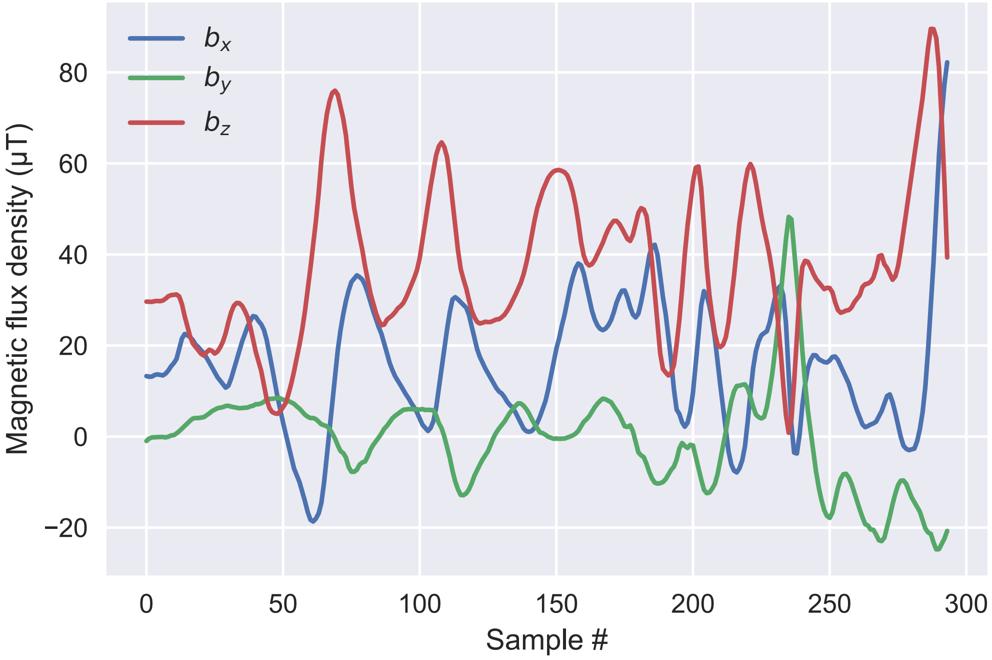

Figure 4.16: *Component-wise magnetic field variations during a run over a cattle grid at the DFKI RIC outdoor test track*

Examining the variations of the total magnetic flux density of the field, the changes are similar to the single-component values, but with an even bigger range of 94.10 µT and a maximum strength of 104.87 at the end of the cattle grid (figure 4.17). This is more than twice the amount of the expected undistorted geomagnetic field strength, though the mean of the ambient distorted total field strength is still close to the expected mean with a value of 44.49 µT. The distribution of the total field strength is mostly centered around the median of 41.17 µT, with some outliers grouped at the high values of around 100 µT.

The magnetic field is not only distorted in the strength of the field, but the vector directions are also strongly diverting as depicted in figure 4.18, which could result in heading deviations of more than 90° in the worst case, which would very well explain the encountered difficulties of the IMU-based navigation.

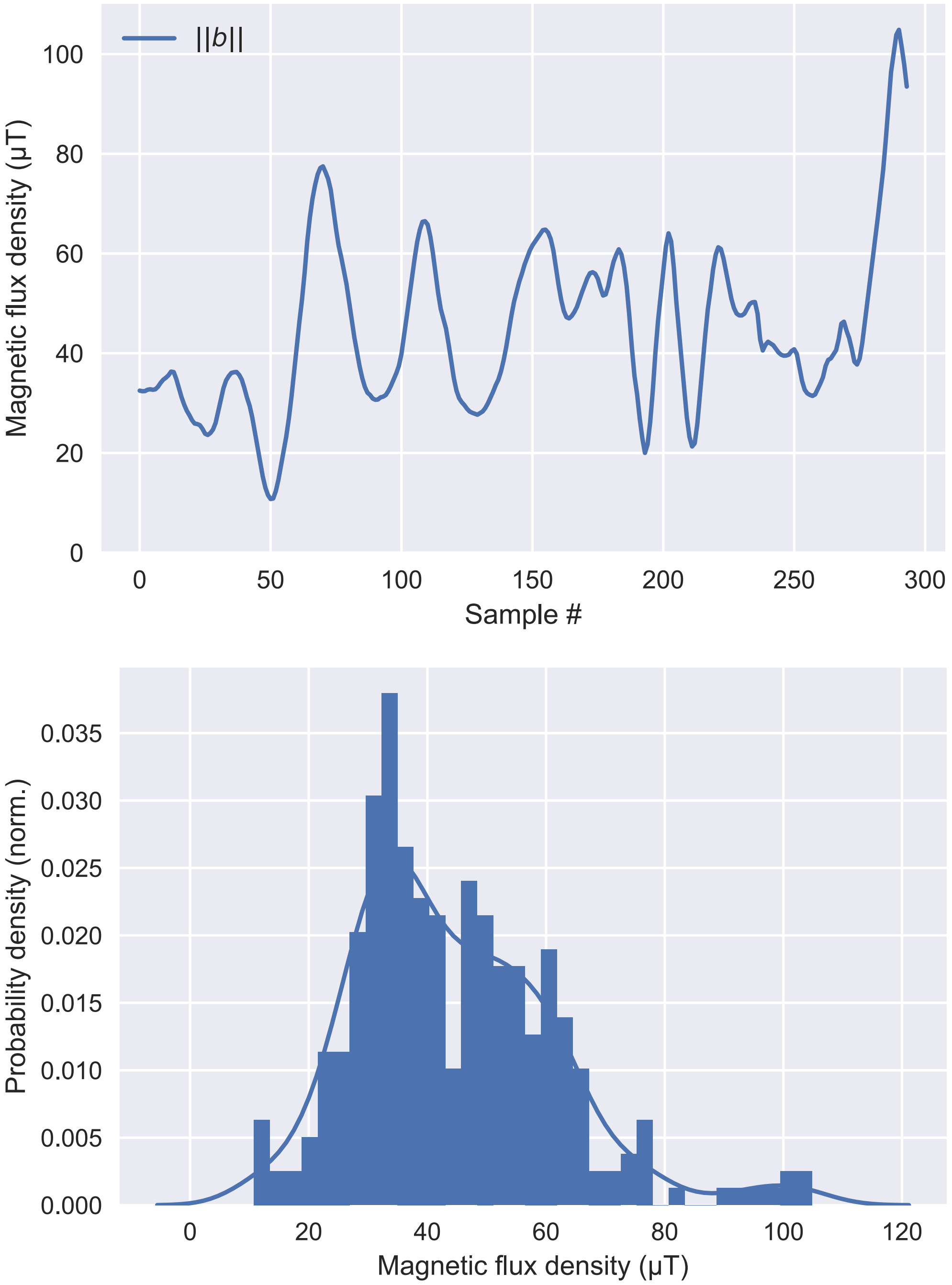

Figure 4.17: *Combined magnetic field strength variations during a run over a cattle grid at the DFKI RIC outdoor test track and the corresponding field strength distribution*

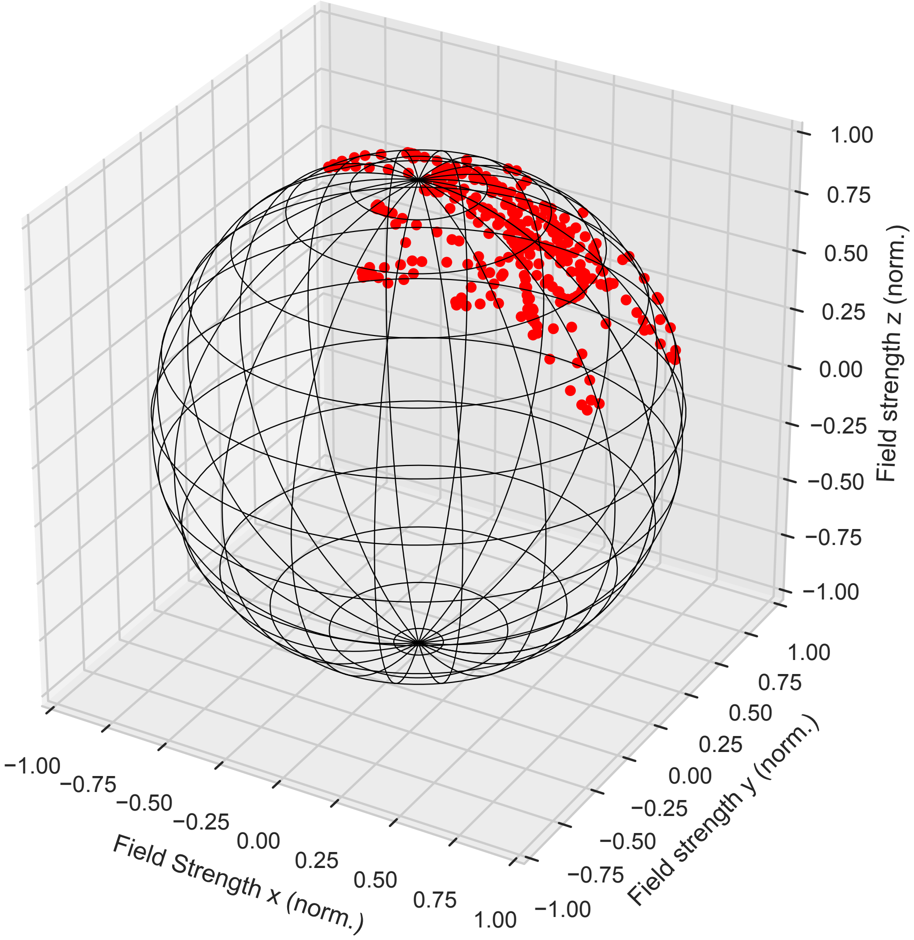

Figure 4.18: *Magnetic field direction change during a run over a cattle grid at the DFKI RIC outdoor test track*

4.4 Space Hall Testbed

Designed to test robotic systems for space applications, the space exploration testbed at DFKI RIC covers an area of $288\,\mathrm{m}^2$, with a maximum height of $10\,\mathrm{m}$. The testbed is equipped with several technical installations for the aspired goal, most notably a $9\,\mathrm{m}$ wide crater test area modelled after a lunar crater near the south pole of the moon and a cable-robot based on a *SpiderCam*-System to simulate (in conjunction with a 6 degrees of freedom (DoF) robotic arm) new methods for the approach or docking of two spacecraft or satellites (see [Girault et al., 2013]). The cable-robot has an extended working range of $16 \times 7 \times 5.5\,\mathrm{m}$. Also installed is an infrared-based marker pose tracking system, covering a volume of $770\,\mathrm{m}^3$.

Figure 4.19: *Space crater environment for robotic testing at DFKI RIC*

Although it is known that the moon has no significant magnetic field in comparison with the Earth, with mainly planetary crust related field strength in the order of nT [Purucker, 2008], a distinct magnetic field is expected in this testbed environment, although the steel frame and sheet metal used in the building may have a shielding effect due to soft iron deflection.

To assess the magnetic field in the volume above and in front of the crater area, an IMU with an integrated 3-axis magnetometer was equipped to the cable-robot via an aluminum profile to prevent magnetic distortions from the fastener. In addition, only the electronic components for communication using a glass fiber to submit the magnetometer signals were activated on the cable-robot rig. To exactly track the magnetometer position, the IMU was equipped with an infrared marker for the *VICON* tracking system, the magnetometer- and tracking data was later fused using pre-coordinated timestamps. The setup is depicted in figure 4.20.

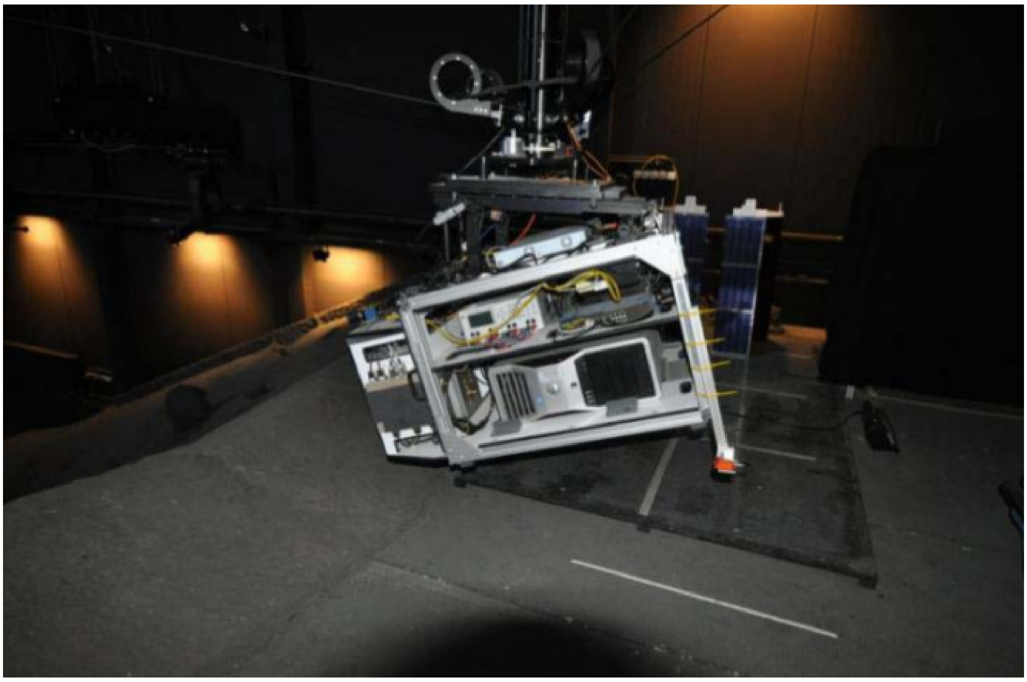

Figure 4.20: *Spidercam system to move the magnetometer through the volume of the space testbed*

The cable-robot then followed a horizontal meandering back-and-forth motion, before moving on to the next lower level, subsequently down the crater rim to the floor of the space testbed, as shown in figure 4.21. For security reasons, the magnetometer mounted to the cable-robot maintained a distance to the crater surface of $\sim 0.5\,\mathrm{m}$.

The characteristics of the plot of the isolated b_x, b_y and b_z components of the magnetic field (figure 4.22) reflect the movement pattern chosen to cover the volume inside the spacehall above the crater slope, for example the distinct 4-cycle in the b_y component is due to the left-right motions across the volume, horizontally approaching the side of the volume with lesser magnetic field strength on one one height level and then withdrawing again on the next.

The 3D plot of the volume with annotated magnetic field strength is depicted in figure 4.23. The difference in magnetic flux density between the sides of the volume is apparent, although the absolute strength variations are rather small compared to the environments discussed before, ranging from $36.92\,\mu\mathrm{T}$ to $45.15\,\mu\mathrm{T}$, with a mean value of $40.08\,\mu\mathrm{T}$ and similar median of $40.12\,\mu\mathrm{T}$.

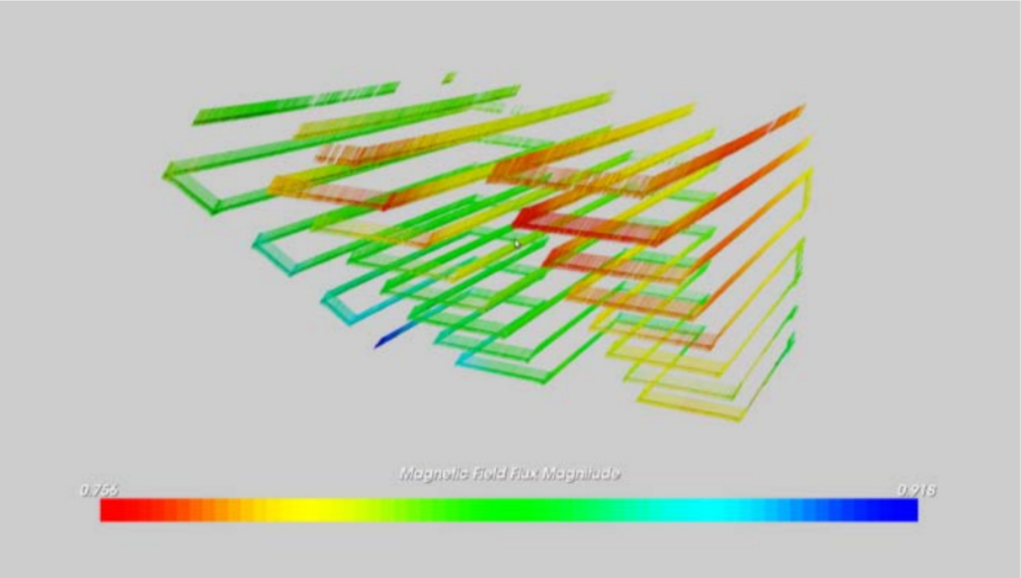

Figure 4.21: *3D rendering of magnetic field vectors (direction and strength) variations in the space crater testbed environment*

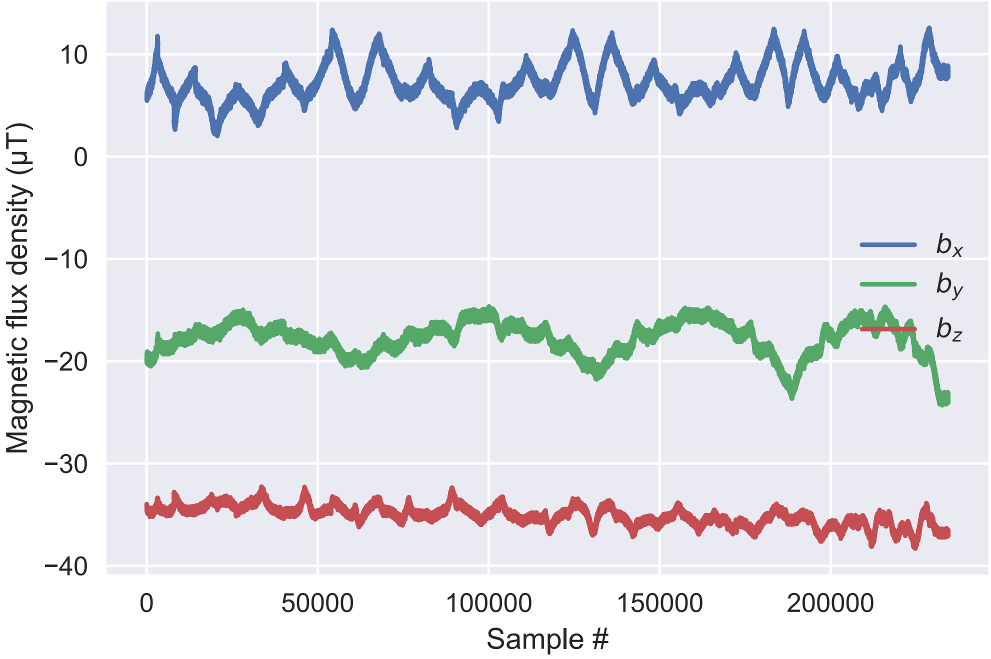

Figure 4.22: *Component-wise magnetic field variations of the volume inside the DFKI RIC space testbed*

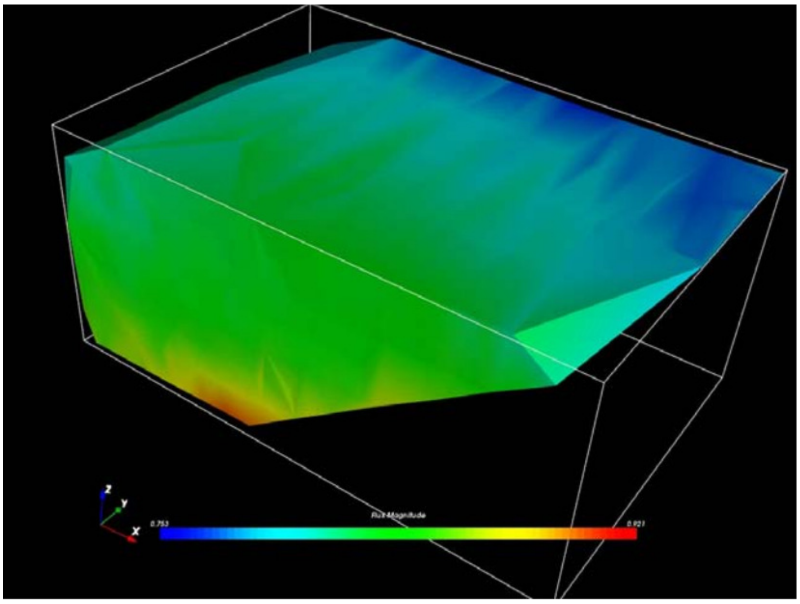

Figure 4.23: *3D volumetric rendering of interpolated magnetic field strength variations in the space crater testbed environment*

Looking at the total field strength, a much more centered distribution can be seen, with a standard deviation of 1.32 µT (figure 4.24), which is also reflected in the low variations of the magnetic field direction, as can be seen in figure 4.25.

On first thought, one would expect stronger deviations of the magnetic field, similar to the distortions experienced in the office environment, due to the material of the main construction frame of the building, which consists of steel girders equipped with a metal sheet roof and side panels. However, with the measured magnetic field in the working space of the cable-robot above and in front of the lunar crater setup being several meters away from the sidewalls and the roof, the soft iron effect of the steel frame construction could cause only minor interference with the assessed magnetic field. The lower overall magnetic field strength of the covered volume in comparison with the geomagnetic field at that place indicates a considerable shielding effect caused by the building construction.

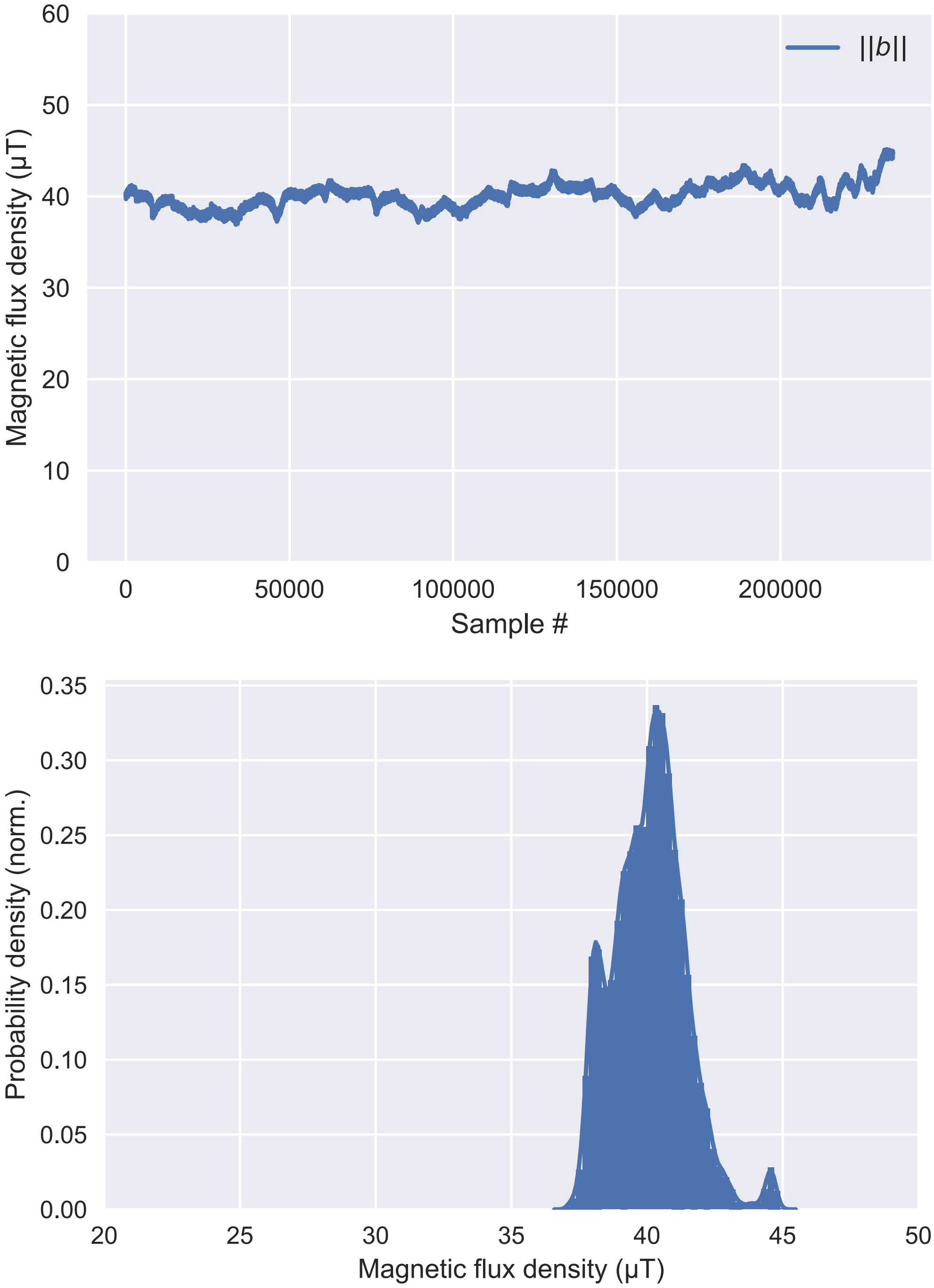

Figure 4.24: *Combined magnetic field strength variations of the volume inside the DFKI RIC space testbed and the corresponding field strength distribution*

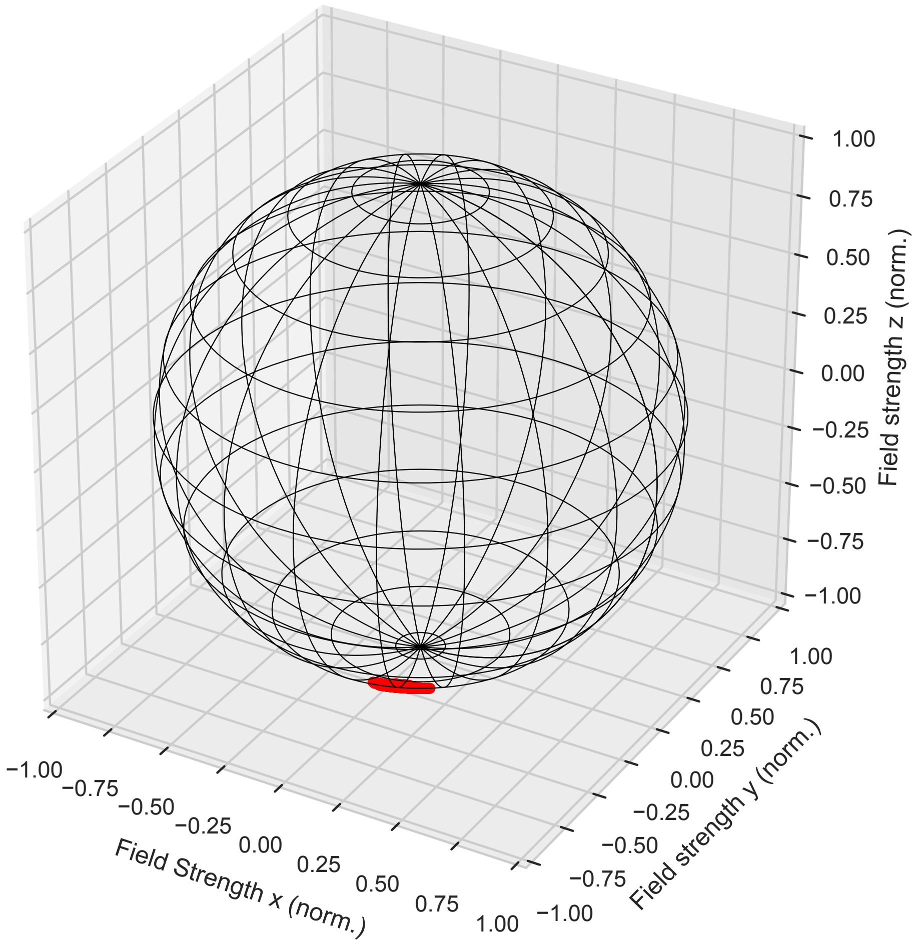

Figure 4.25: *Magnetic field direction change in the volume inside the DFKI RIC space testbed*

4.5 Assessment Comparison

Figure 4.26 sets the total magnetic field strength variations of the environments assessed in the previous sections in relation to each other using boxplots. The line in the middle of each individual box represents the median of the data set, whereas the lower bound of each box indicates the lower quartile (Q_1, 25th percentile) and the upper bound accordingly the upper quartile (Q_3, 75th percentile). The distance between the lower and upper quartile defines the interquartile range (IQR), a measure of statistical dispersion, estimating the spread/variability of the distribution. The 'whiskers' are indicating the limits of $Q_1 - 1.5IQR$ and $Q_3 + 1.5IQR$, commonly denoting the outlier boundaries. The dots above and below those boundaries indicate the samples outside of these boundaries.

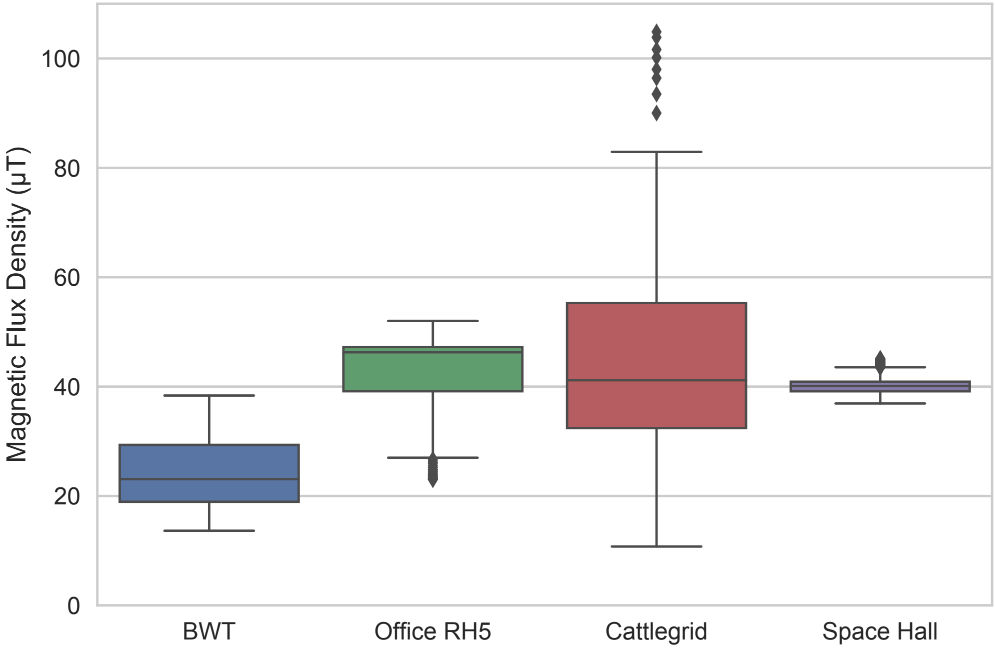

Figure 4.26: *Boxplots of the total magnetic field strength distortion distributions for several robotic application environments*

All evaluated environments are displaying a considerable amount of spread due to ambient features of the environment, with the space environment testbed having the smallest interquartile range and the cattle grid environment the largest. Summarizing, most of the exemplary environments for possible robot application scenarios have an ambient magnetic field that shows significant features in comparison to the locally uniform geomagnetic field, which could be exploitable for navigation purposes. This holds true especially for environments like artificial structures with material of high magnetic permeability, even though also large scale outdoor environments with natural formations of magnetic susceptible material like magnetite on the seafloor may lend themselves to exploit the magnetic field features for navigation purposes, depending on the distribution of the features and the scale of the navigation task.

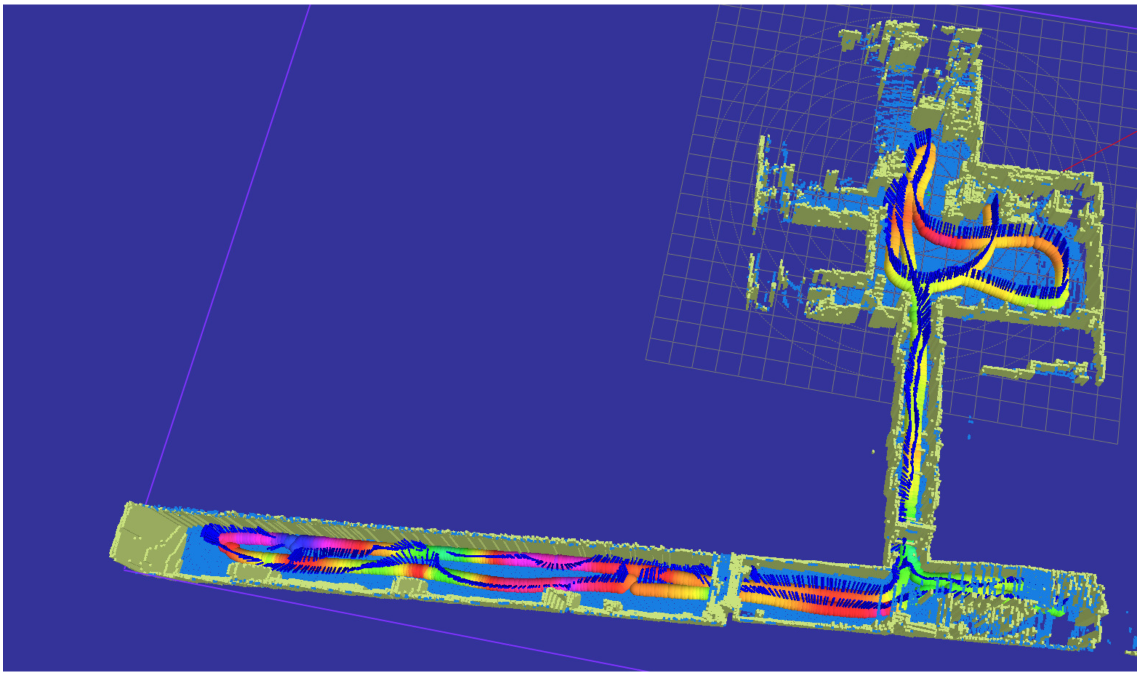

Figure 4.27: *SLAM generated map of larger indoor environment at DFKI RIC RH1 integrating magnetic field readings. Changes of the sphere color indicate significant changes of the magnetic flux density in such environment, whereas the blue pin is indicating the magnetic field direction.*

Depending on the position in the magnetic field of the local environment, the distinct deviations occur more in the strength component or are more significant in the directional component. Figure 4.27 shows a SLAM generated map of the DFKI RIC RH1 building, incorporating both the strength and directional components of the local magnetic field variations. Considering the temporal domain, the ambient magnetic fields could be considered quasi-static, remaining stable over time, just changing with the secular variations of the geomagnetic field itself.

Chapter 5

Magnetic Fields of Mobile Robots

Given that one either wants to use the undisturbed geomagnetic field at a certain time and place (see Section 2.3) or exploit the more sophisticated features of ambient magnetic fields (see Chapter 4) for navigating mobile robots, there is a major obstacle for that in either way: the physical embodiment of the robot itself. While some approaches to robot localization like *EmbodiedSLAM* [Schwendner and Kirchner, 2010, Schwendner et al., 2014a] are making use of just that property, it provides a major hurdle when trying to measure the ambient magnetic field without self-induced distortions. A lot of the material used in robotic systems show strong soft- or hard iron effects, like iron, cobalt or nickel and alloys like AlNiCo or permalloy ($Nd_2Fe_{14}B$).

Nowadays, in the search for lightweight or robust materials for robotic applications, material like fiber-reinforced plastics (e.g. fiberglass, carbon, aramid), stainless steel or titanium are often used. These materials show a quasi-neutral behavior due to their relative magnetic permeability coefficient close to one (see Section 2.1), however, some of the fundamental components of robots like motors or hard drives are virtually depending on strong ferromagnetic materials, which exhibit unwanted hard- or soft iron distortion effects (see Section 2.2).

In addition to that, considerable electric currents may flow through supply lines, motor windings and other conductors of internal or external equipment and payloads of a robotic system. To further complicate the usage of magnetometers in often confined mobile robots, the robots may be able to change their posture or configuration, for example robots with arms and legs showing a high number of DoF or modular robots with changing payloads or configurations. To get an overview of the amount of distortion caused by the systems, several mobile robots of different classes were evaluated in the course of this work, which are discussed in the following subsections.

5.1 Rigid Body AUV - *DAGON*

The autonomous underwater vehicle (AUV) *DAGON* is specifically designed as a scientific AUV for visual mapping and localization with stable hovering capabilities. Its high-quality stereo camera system usually acts as the main sensor system and is supplemented by an internal IMU and a pressure sensor. Using visual odometry and SLAM approaches, a map of the seafloor and the vehicle's trajectory can be generated [Hildebrandt and Hilljegerdes, 2010]. In addition to the visual main sensory system, the AUV is equipped with additional navigational instruments like an Acoustic Long Baseline Navigation System (LBL), a Doppler Velocity Log (DVL) and a Fibre Optic Gyroscope (FOG), usually used to establish a ground truth to evaluate novel underwater localization techniques. The AUV has a lithium-ion battery with a capacity of 1.6 kWh, resulting in a corresponding nominal operating time of six hours, which may vary with the type of mission. *DAGON* can either be used as a completely autonomous vehicle, with the only communication available being the low-bandwidth acoustic modem, or connected to a fiber-optic cable for telemetry. Using this cable, a hybrid-ROV mode is also possible, where the vehicle is controlled by a human operator or a control station onshore [Hildebrandt et al., 2012].

Figure 5.1: *Scientific AUV DAGON, a representative of a rigid-body robotic system*

For the purpose of evaluating magnetic fields generated by different types of mobile robotic systems, the AUV *DAGON* represents a more static type of robot, with a rigid body and thus a limited amount of DoF of its posture. While other AUVs like gliders have internal moving parts like dive-cells or movable battery packs to change the buoyancy or the center of gravity, *DAGON*'s configuration is completely fixed during a dive. In such a setup, the only persistent distortion one would expect could be due to electromagnetic effects of the changing motor currents. Data sets with *DAGON* were recorded while decreasing the PWM signal from 100 to $0\,\%$ over a period of $10\,\mathrm{s}$, then increased again back to $100\,\%$ in the same period of time. This was done for every thruster subsequently. The internal magnetometer of the IMU residing in the main pressure compartment was used as data source for the 3D magnetic field measurements. The AUV's position was fixed during the whole recording process, to isolate the distortions induced by the motor currents.

Figure 5.2 depicts the singular magnetic field components b_x, b_y and b_z for one increase/decrease PWM cycle of $20\,\mathrm{s}$ of the vertical front heave thruster. As can be seen, all singular components of the magnetic field show no drift, but significant noise and 3 distinct peaks in the magnetic flux density.

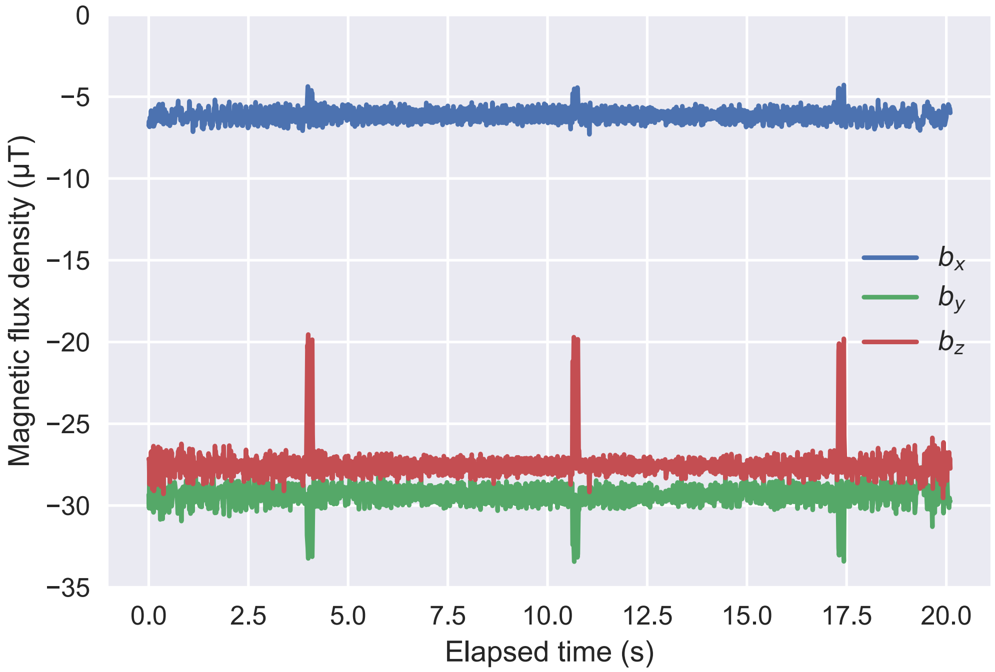

Figure 5.2: *Singular components of magnetic field variations on AUV DAGON, 20 s sequence of decreasing (10 s) and increasing (10 s) heave thruster PWM values from 100 to 0 % and back*

Compared to the total strength variations depicted in figure 5.3, the peaks are showing up too, although to a lesser extent. Zooming in, the amplitude of the high-frequency noise seems to be correlated to the decreasing and then again increasing

PWM signal.

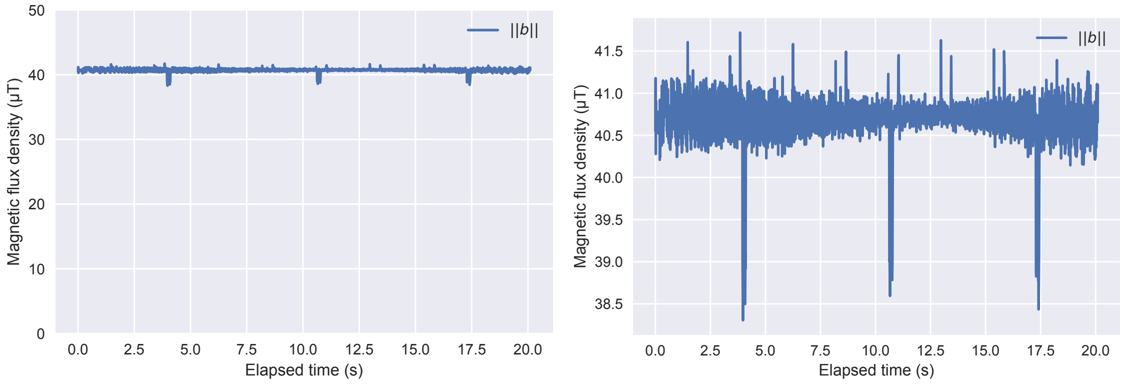

Figure 5.3: *Combined magnetic field strength variations on AUV DAGON, 20 s sequence of decreasing (10 s) and increasing (10 s) heave thruster PWM values from 100 to 0 % and back. Zooming in (right), the plot indicates a correlation between the PWM value and the noise amplitude.*

The distribution of the total magnetic field strength for the *DAGON* data set (figure 5.4) is closely centered around the median of 40.73 µT with a lower quartile of 40.60 µT and an upper quartile of 40.85 µT, with a minor mode around 39 µT due to the peaks in magnetic flux density noticed before.

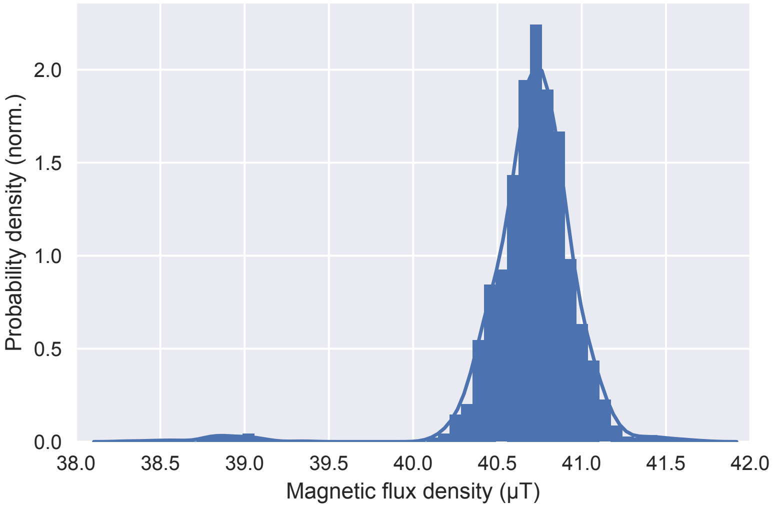

Figure 5.4: *Distribution of the total magnetic field strength variations on AUV DAGON*

Despite the noticeable peaks in the magnetic flux density, the directional component of the magnetic field during the change in thruster PWM of AUV *DAGON* remains a narrow cluster with very small deviation (see figure 5.5).

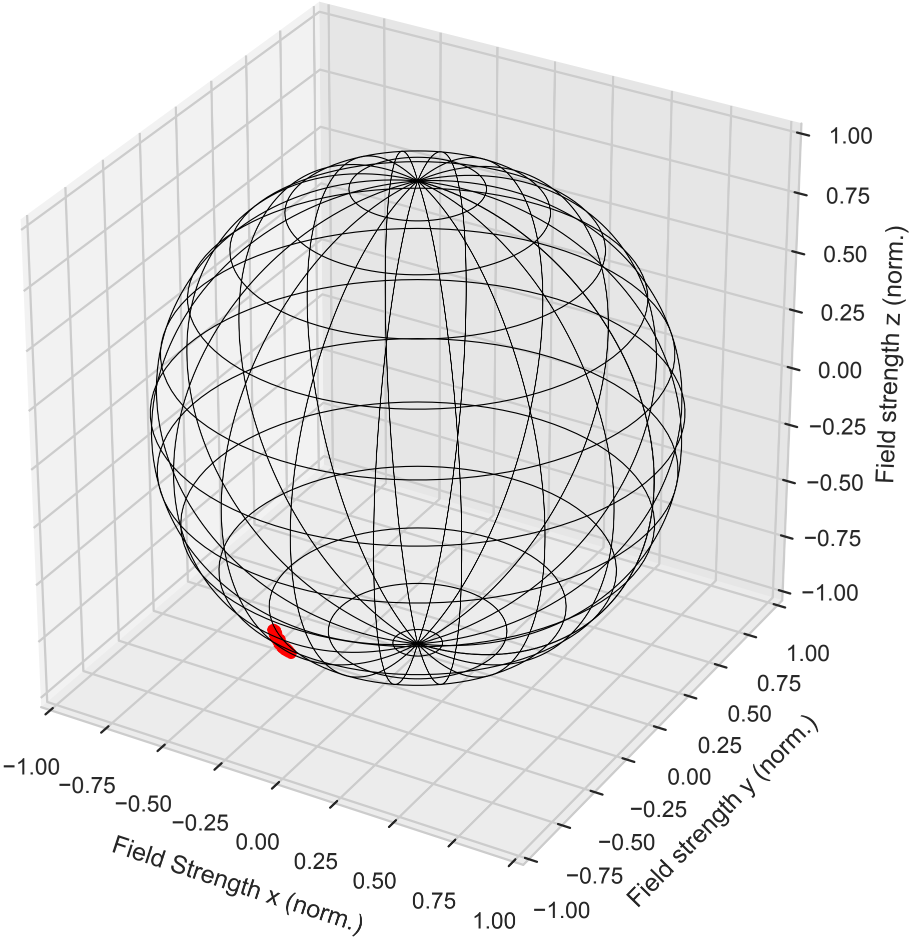

Figure 5.5: *Magnetic field direction change while changing thruster PWM of AUV DAGON*

5.2 Agile Wheeled Rover - *ASGUARD*

This subsection discusses a robot having a lightly raised body complexity with an additional DoF compared to the robot discussed before. The micro rover *ASGUARD* II, designed for agile locomotion in harsh outdoor environments, features a rear body part, that can rotate via a passive rotary joint (see figure 5.6).

Figure 5.6: *Agile micro rover ASGUARD II, featuring a free rotating rear axle*

The robot's rear body part structure is made of carbon fiber and aluminum, both non-ferromagnetic materials. But since there are DC-motors equipped at either end of the axle, both incorporating strong ferromagnetic material, the rotation of the rear body part of the robot may distort the magnetic field measured at the magnetometer sensor integrated into the IMU of *ASGUARD*, which is located in the front main body housing.

To assess the amount of distortion emanating from the specific locomotion feature of *ASGUARD*, the 3D magnetometer data was recorded while deliberately turning the rear body part to its rotary limits with an otherwise fixed pose of the robot. The singular components b_x, b_y and b_z of the measured magnetic field overlayed with the turning angle θ in rad of the rotary joint is depicted in figure 5.7. While minuscule variations in the components are visible, the magnetic flux density levels remain level throughout the turning sequence.

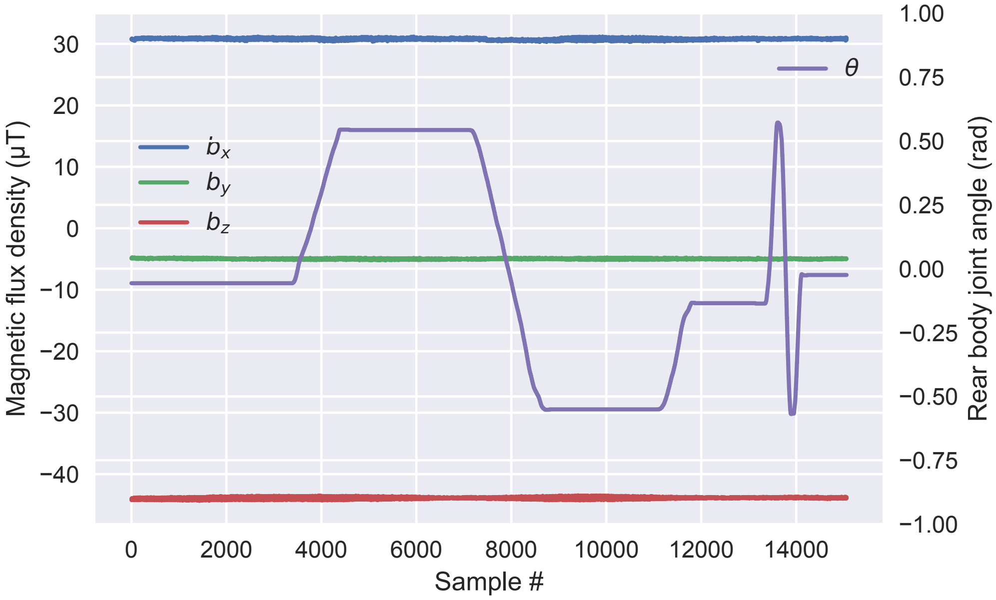

Figure 5.7: *Magnetic field singular component variations on rover ASGUARD II during rotation of the rear body part from limit to limit*

The same holds true for the total magnetic field strength, as can be seen in figure 5.8. The distribution is centered around the median at 53.82 with very close lower and upper quartile of 53.67 µT and 54.01 µT, respectively. The significant three peak modes of the distribution are likely corresponding to the three main held turning angles: left limit, neutral and right limit of the rotary rear body joint.

The interesting multi-mode distribution of the strength is however not reflected in the direction component of the magnetic field during the rear joint turning motion, which remains centered at its original direction (figure 5.9).

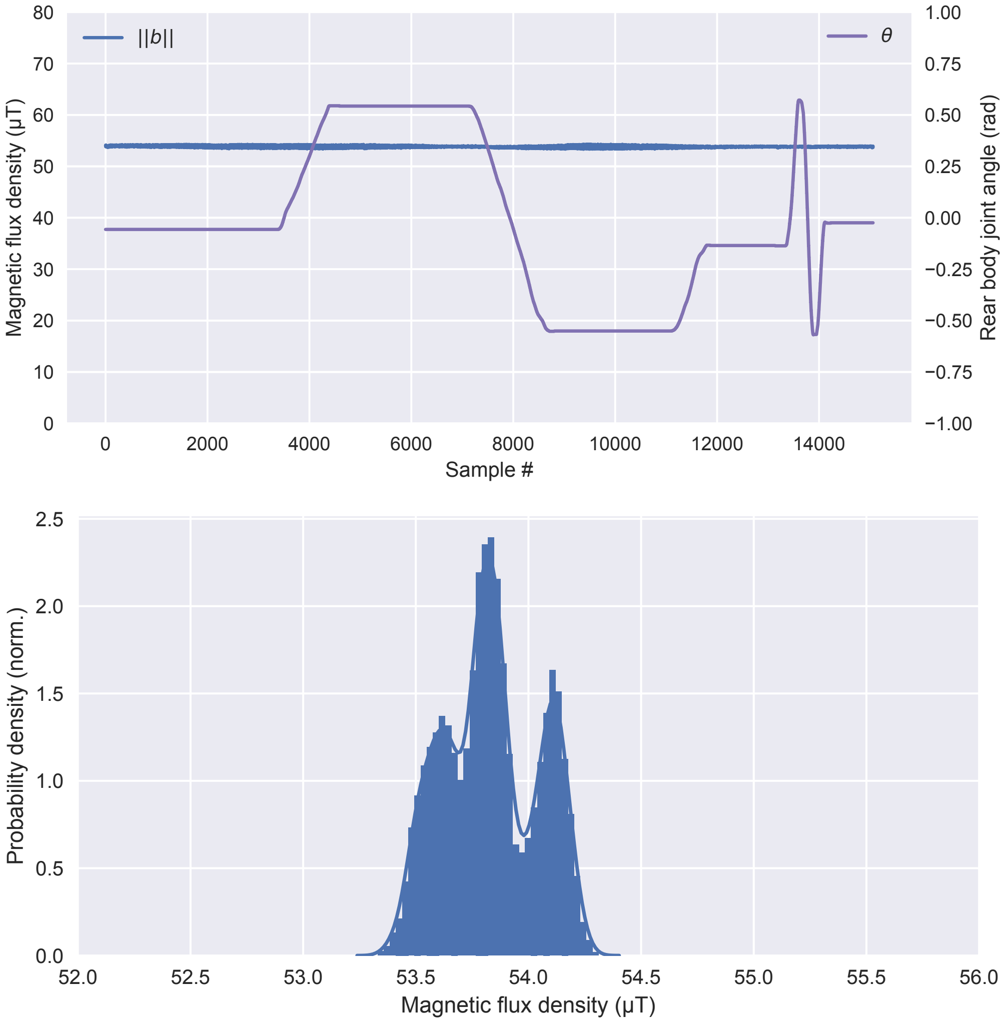

Figure 5.8: *Total magnetic field strength variations on rover ASGUARD II during rotation of the rear body part from limit to limit and the according magnetic flux density distribution*

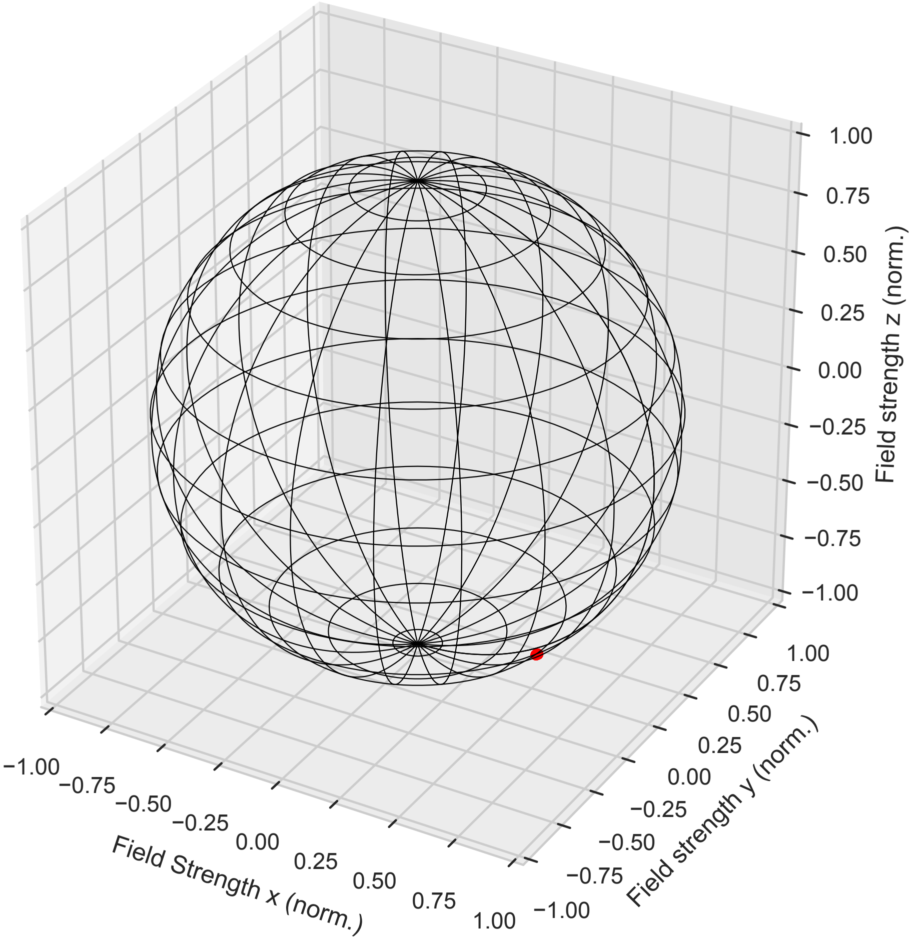

Figure 5.9: *3d scatter plot of magnetic field directions while rotating the rear body of ASGUARD II*

5.3 Passive Suspension Rover - *ARTEMIS*

A rigid body robotic system with additional DoF compared to *ASGUARD* is the terrestrial rover *ARTEMIS* [Schwendner et al., 2014b], which was designed and built to compete in the SpaceBot competition of the DLR. This rover has a weight of $75\,\mathrm{kg}$, a size of $120\,\mathrm{cm} \times 80\,\mathrm{cm} \times 107\,\mathrm{cm}$ and can drive at a maximum speed of $0.5\,\mathrm{m\,s^{-1}}$. It was chosen in this work due to the triple bogie suspension system for extra mobility in rough terrain, which is expected to exhibit deviation effects on the local magnetic field due to the moving ferromagnetic parts in the attached motors. One bogie carrying the front axle is oriented perpendicular to the vehicle's longitudinal axis, whereas the left and right bogies carrying the other four wheels in a twin setup, can passively turn around the lateral axis of the robot (see figure 5.10). For the purpose of this work, the attached manipulator was deactivated and its posture fixed.

Figure 5.10: *The ARTEMIS rover with triple bogie suspension system and manipulator designed for the DLR SpaceBot competition (left) and marked IMU placement (right)*

To assess only the influences of the system itself with its triple bogie system on the local magnetic field, the rigid body pose of *ARTEMIS* was again fixed during the data recording. This ensures that no local variations of the ambient magnetic field due to position changes of the robot interferes with the assessment of the system-inherent distortions. As with *ASGUARD*, the magnetometer used to record the magnetic field changes was the internal sensor of the vehicle's IMU attached to the top of its sensor pole with a distance to the bogie joints of approximately $60\,\mathrm{cm}$.

Figure 5.11 depicts the magnetic flux density variations in the individual b_x, b_y and b_z components of the local magnetic field measured at the IMU's position mentioned above, while the suspension bogies of *ARTEMIS* were rotated 50° from limit to limit separately and in combination in this data set. The bogie angles are integrated with a separate axis on the right side into the same plot.

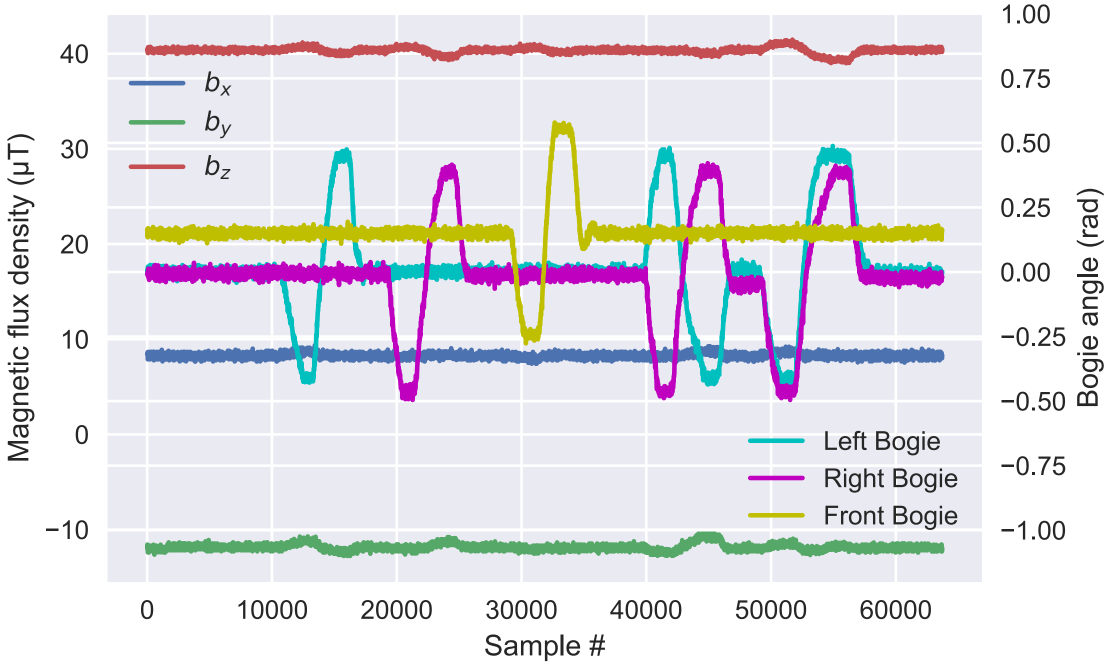

Figure 5.11: *Magnetic flux density variations in each axis of the magnetometer while the suspension bogies of ARTEMIS were rotated from limit to limit*

The first impression on the whole dataset is, that the general level in each individual component remains quite stable during turning of the bogies, where one would have expected stronger deviations due to the ferromagnetic material inside the motors mounted to the bogies. This impression is relativized, when looking more closely at a subset of the sequence in figure 5.12: A significant correlation between the bogie joint angles and the magnetic field flux density becomes visible, with variations up to 2 µT in parallel with the joint rotations.

The total field strength is again reflecting this correlation, with an overall distribution around the median of 42.89 µT, narrowly concentrated with a lower quartile of 42.72 µT and upper quartile of 43.04 µT (figure 5.13).

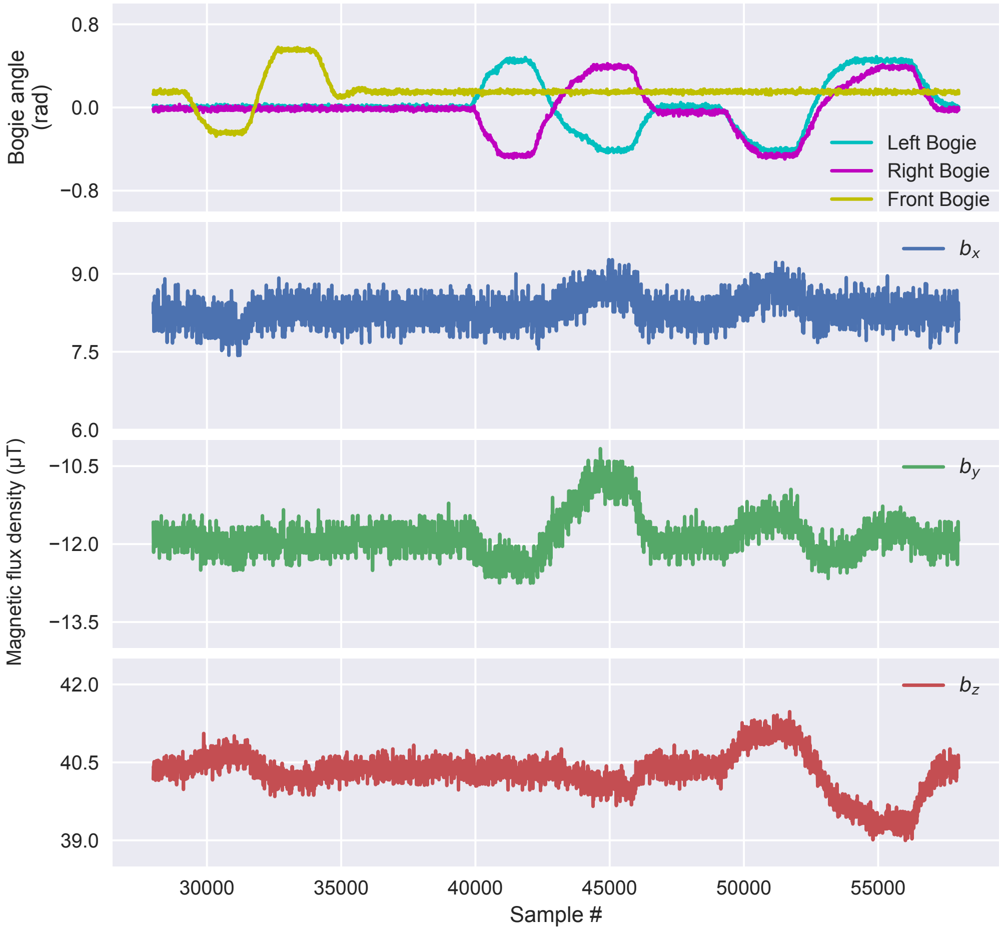

Figure 5.12: *Magnetic flux density variations in each axis of the magnetometer while the suspension bogies of ARTEMIS were rotated from limit to limit, zoomed-in subset*

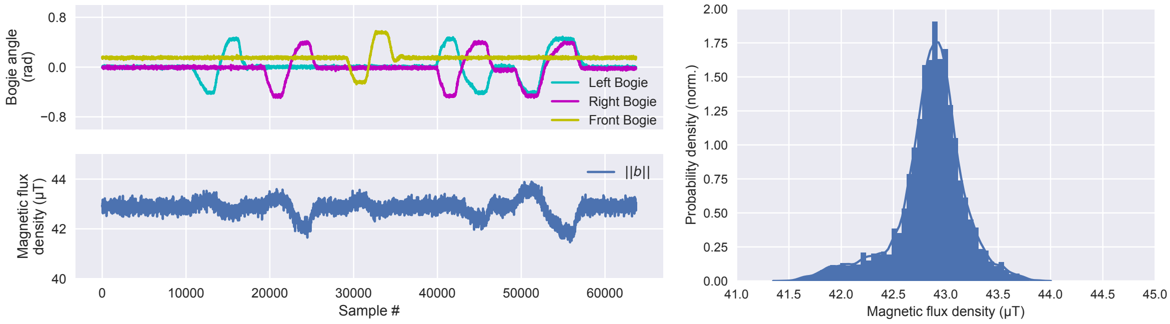

Figure 5.13: *Total magnetic field strength variations on rover ARTEMIS during rotation of the bogies from limit to limit (left) and the according magnetic flux density distribution (right)*

Zooming deeper into a subset from sample 47500 to the end of the data set at sample 63710, a shape similar to that of the *ASGUARD* rover can be identified, with two noticeable modes to the left and right side of the median, correlating to the magnetic field strength peaks at the bogie joint limits (figure 5.14).

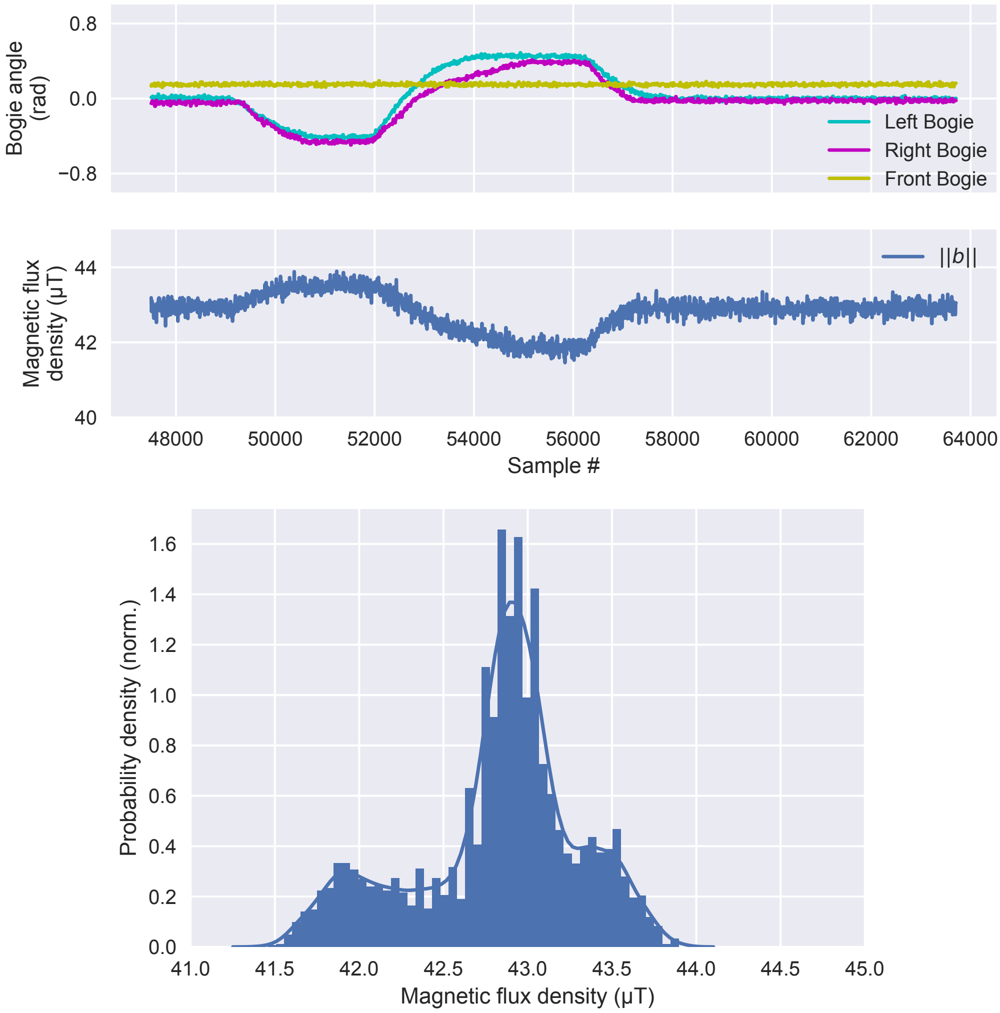

Figure 5.14: *Total magnetic field strength variations on rover ARTEMIS during rotation of the bogies from limit to limit (left) and the according magnetic flux density distribution (right), zoomed-in subset*

Considering absolute numbers, the amount of magnetic flux density deviation is ranging from 41.46 to $43.90\,\mu\mathrm{T}$. This span of only $2.44\,\mu\mathrm{T}$ is rather small in comparison with the total field strength of $49.46\,\mu\mathrm{T}$ in Bremen. The direction of the magnetic field thus remains very stable despite the deviation effect of the turning suspension bogies, as depicted in figure 5.15.

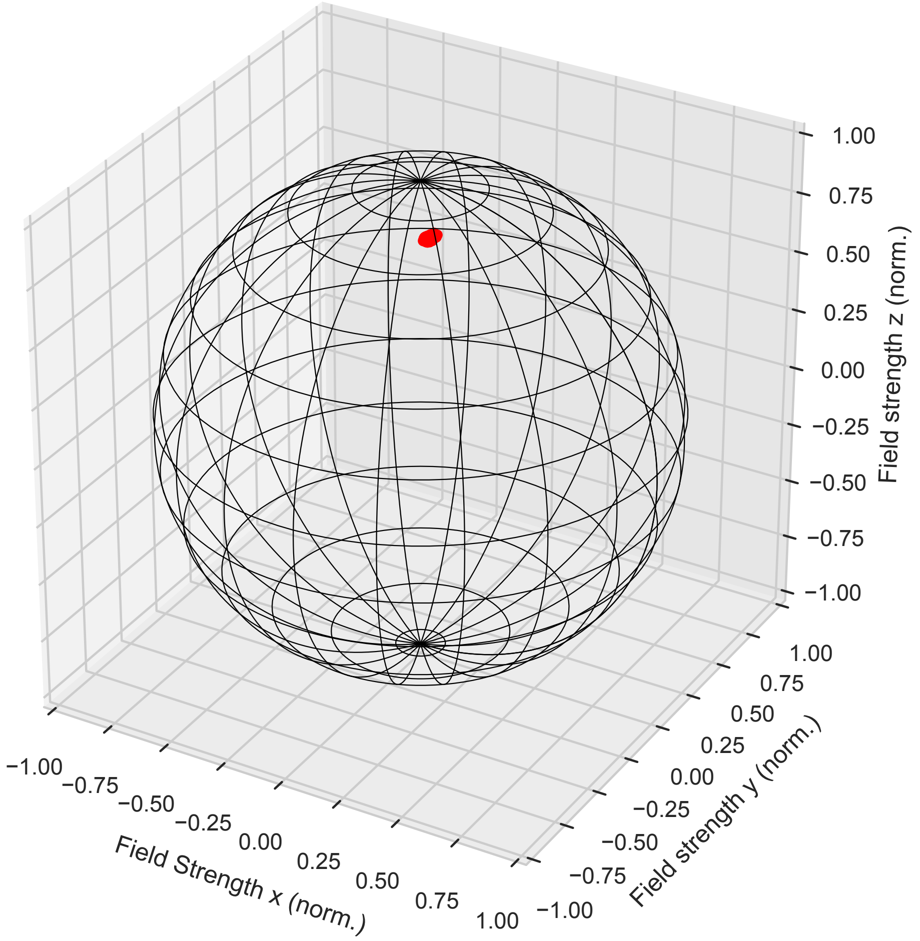

Figure 5.15: *3D scatter plot of magnetic field direction changes while rotating the suspension bogies of the robot ARTEMIS*

5.4 Legged Walking Robot - *CHARLIE*

Again increasing the number of degrees of freedom and thus the expected amount of system-induced magnetic field distortions, the system evaluated in this section is the robot *CHARLIE*. The bioinspired hominid robot features an active artificial spine of 6 DoF and a sophisticated lower limb system with two legs of 7 DoF each and two multi-contact feet. In addition to that, the head can be actuated with 6 DoF and the two arms both with 5 DoF. The robot was designed, among other things, to study the possible transition from four-legged walking to upright bipedal walking behaviors and is equipped with a huge amount of sensors integrated over the whole robot structure [Kühn, 2016]. In the context of this work, *CHARLIE* stands for a class of legged walking robots featuring a massive amount of DoF.

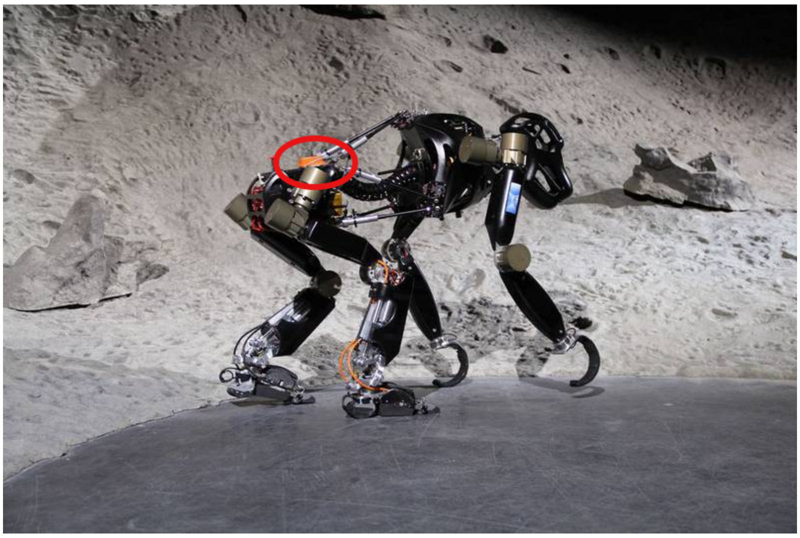

Figure 5.16: *The four-legged robot CHARLIE with sophisticated lower limb system for increased mobility in unstructured terrain. The red circle indicates the mounting position of the IMU on the lower spine.*

To assess the amount of local magnetic field distortions for the robot *CHARLIE*, data from the IMU mounted at the end of the lower spine was recorded, while the robot was executing a straight walking pattern with four subsequent lift- and stance phases for each leg, with a duration of one full cycle of 4.8 s (see figure 5.17).

As depicted in figure 5.18, the magnetic field flux density components show a very strong correlation with the rear legs lift- and stance phases and also with the currents of the spine motors at that point in the cycle of the straight walking pattern.

The total magnetic field strength depicted in figure 5.19 has a level of $\sim 42\,\mu\mathrm{T}$ at the start and at the end of a walking pattern cycle, followed by very strong, seemingly

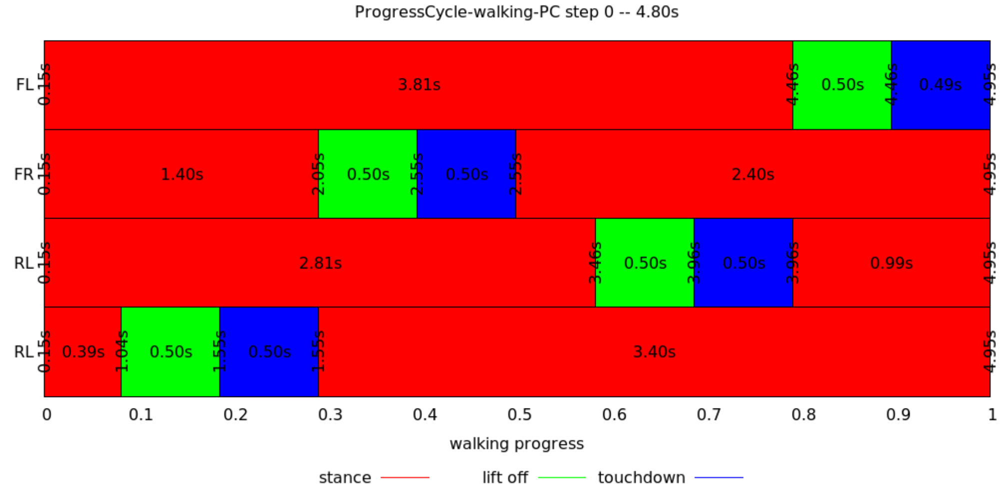

Figure 5.17: *One cycle of the straight walking pattern of the robot CHARLIE with indicated lift- and stance phases for each leg (front left(FL), front right (FR), rear left (RL) and rear right (RR))*

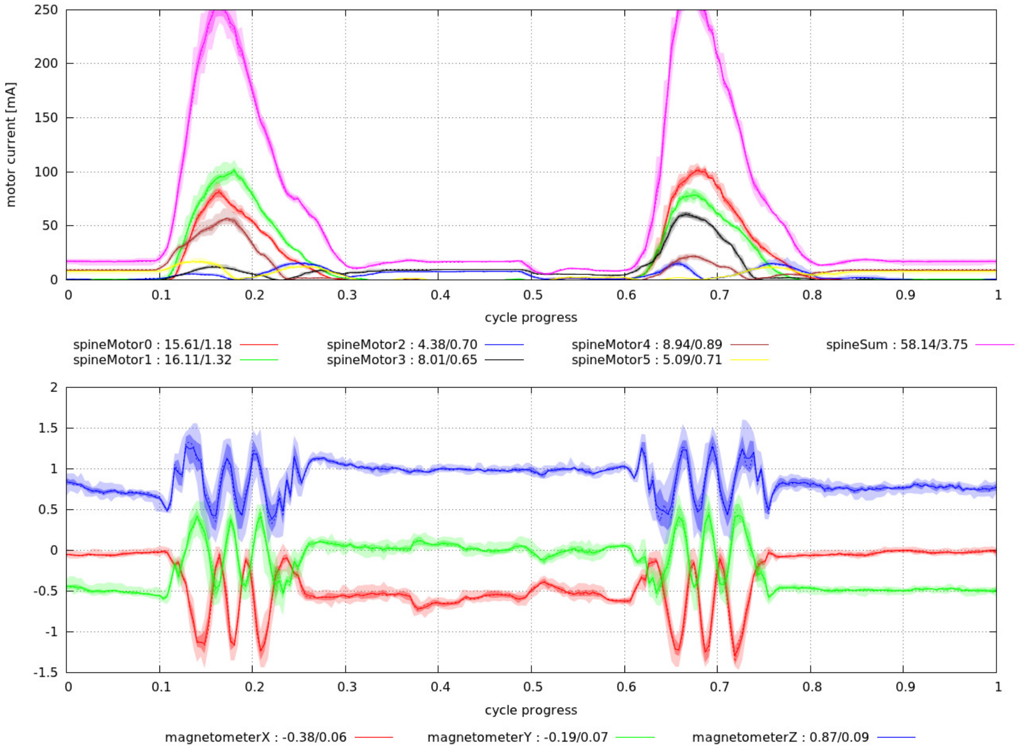

Figure 5.18: *Spine motor currents (above) and component-wise magnetic flux density (below) during a straight walking cycle of robot CHARLIE. Y axis of magnetic field plot is showing normalized magnetic flux density, with 1 equal to* 49.0 µT *(source: Martin Zenzes, DFKI).*

erratic, peaks when the rear legs are used and a huge offset in the middle phase of the cycle. Inspecting the strength distribution, a spread orders of magnitude larger than in the robotic systems discussed above can be seen, with a lower quartile at 40.81 µT, an upper quartile at 84.47 µT and the median at 57.95 µT. The distribution shows two distinct modes corresponding to the main levels at rest (start and end of a cycle) and in the middle phase of the cycle.

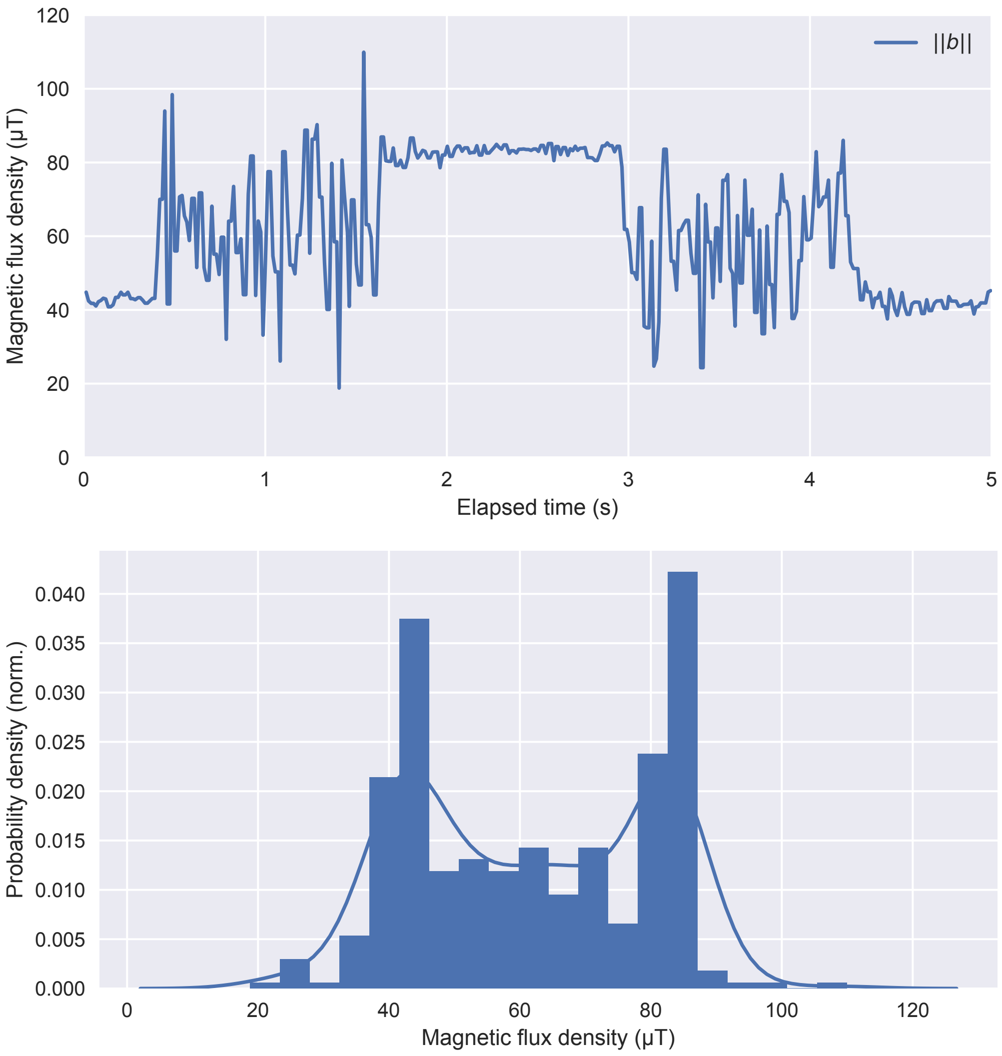

Figure 5.19: *Strong variations of the total magnetic field strength during a straight walking pattern cycle of robot CHARLIE and according spread out distribution*

The changes in the magnetic field direction are equally strong, as shown in figure 5.20. The directions are spread out over the whole lower hemisphere, which denotes a full direction reversal in the most extreme cases.

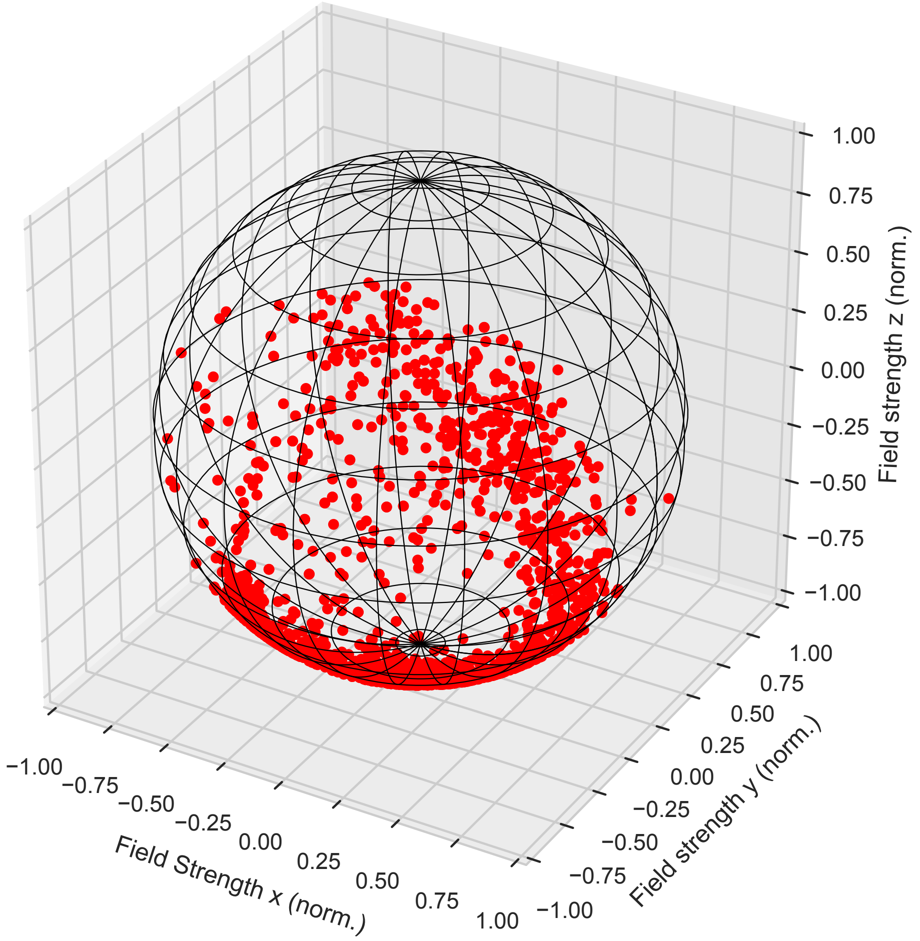

Figure 5.20: *3D scatter plot of magnetic field direction changes during a straight walking pattern cycle of robot CHARLIE*

5.5 Assessment Comparison

To compare the distributions of the total magnetic field strength for the individual robots, which were selected as representatives of a certain class of robots with increasing DoF, figure 5.21 shows boxplots for the systems discussed above. As described earlier (see Chapter 4), the line in the middle of each individual box represents the median of the data set, whereas the lower bound of each box indicates the lower quartile (Q_1, 25th percentile) and the upper bound accordingly the upper quartile (Q_3, 75th percentile). The distance between the lower and upper quartile defines the IQR, a measure of statistical dispersion, estimating the spread (variability) of the distribution. The 'whiskers' are indicating the limits of $Q_1 - 1.5IQR$ and $Q_3 + 1.5IQR$, commonly denoting the outlier boundaries. The dots above and below those boundaries indicate the samples outside of these boundaries.

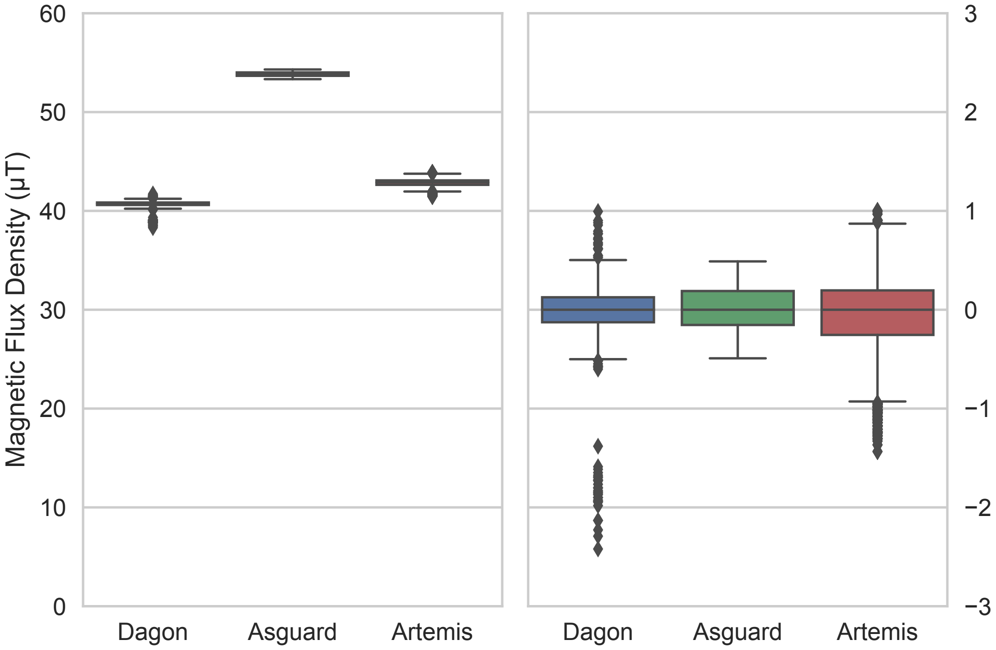

Figure 5.21: *Boxplots of the total magnetic field strength distortion distributions for the individual systems chosen as a representative for a certain class of robots with increasing DoF. On the right side, the distributions where shifted to zero, for better range comparison.*

When comparing the amount of variation in the systems in figure 5.21, one can see a similar spread of the three robots *DAGON*, *ASGUARD* and *ARTEMIS* with slightly increasing interquartile range, parallel to the increasing DoF of theses systems. The marked outliers in the case of the AUV *DAGON*, due to the single spikes in the magnetic field flux density shown earlier, were due to a defect in the electronic grounding of the system, as later identified during robot maintenance. When including the hominid robot *CHARLIE* in the comparison (figure 5.22), the huge amount of increased variation of the magnetic field strength again reflects the drastic rise in DoF of such a mobile walking system. Despite the great variability in some systems, the disturbances that occur are not of a magnitude that makes the underlying magnetic field indeterminable, but rather of a magnitude similar to the features of the ambient magnetic fields evaluated in Section 4.

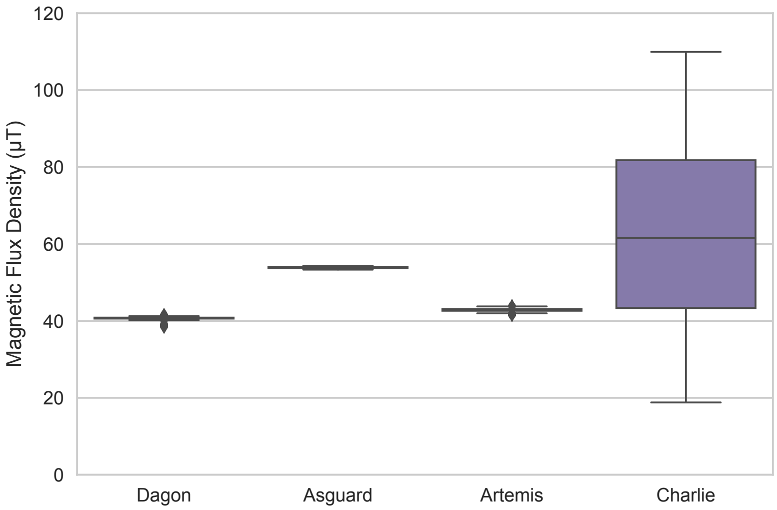

Figure 5.22: *Boxplots of the total magnetic field strength distortion distributions, here including the hominid walking robot CHARLIE with its increased number of DoF and significantly larger spread of the distribution.*

Apart from the assessed robot magnetic fields described here, further robotic systems like underwater crawlers and other types of AUVs have been evaluated in this respect during the course of this work. While the systems discussed here already give a good overview of the range of magnetic field characteristics encountered in different kinds of mobile robots, the additional assessed systems are not described here but are discussed in more depth in the specific context of distortion compensation and localization in the following chapters.

Chapter 6

Distributed Magnetometer for Distortion Compensation

This section describes a new approach combining multiple hardware elements and a corresponding software algorithm to deal with the dynamic distortions of the ambient magnetic field, originating from the mobile robotic systems themselves as described in Chapter 5. These distortions commonly lead to erroneous magnetometer measurements of the ambient magnetic field and thus are the source of many problems in orientation estimation or localization approaches (see the problems of the state of the art in such cases as described in Chapter 3). The approach was first developed for underwater robots [Christensen et al., 2015], especially confined unmanned underwater vehicles, but is also valid for a broader range of mobile robotic systems, that are spatially contrained and are used in rough environments. In such systems, the space to mount magnetometer sensors is strictly limited and the sensors are often in the vicinity of distortion sources like ferromagnetic material, sensor transducers or strong electric currents flowing through nearby supply lines.

The approach to deal with these magnetic field distortions described in this section is threefold: *a*) the use of multiple distributed magnetometers for robustness *b*) the design of very small pressure-neutral sensor modules to get rid of mounting restrictions inside pressure compartments and *c*) the development and application of a multi-magnetometer fusion algorithm using von Mises-Fisher (vMF) distributions [Fisher, 1953] to compute undistorted pose information.

Whereas localization on the surface has found its reference technology in Global Navigation Satellite Systems (GNSS, e.g. GPS), it is not applicable in the underwater domain. This is due to the fact that higher frequency radio signals become unusable once the sensor is submerged because of the water's strong attenuation. System solutions to the subsea localization problem are usually more expensive and, in comparison, require more custom-tailoring to the specific application scenario. In addition to this extra effort, subsea applications often require the the installation of additional infrastructure like long baseline (LBL) positioning systems or the deployment of sophisticated ultra-short baseline (USBL) setups [Christensen et al., 2010].

At the base of every dead-reckoning navigation, there is commonly an IMU, usually consisting of at least accelerometers and gyroscopes to determine orientation. Since gyroscope measurements drift over time, IMUs are often supplemented with a magnetometer to stabilize the heading. The measured magnetic field is subject to significant distortions (soft and hard iron effects), caused for example by nearby ferromagnetic materials or strong electric currents, as described in section 2.2. This specifically applies to compact autonomous underwater vehicles and robots, where mounting options for magnetometers inside pressure housings are strictly limited. Depending on the severity of the system-induced and dynamically changing field distortions in the vicinity of the sensor, a priori calibration techniques can correct the measurements only to a certain point and may fail completely on systems with moving ferromagnetic parts, like underwater gliders with moving battery packs.

The main reasoning behind the approach described in the following is that the *dynamic* distortions are usually *only locally distributed* and most relevant in the direct vicinity of the distortion source (e.g. near strong ferromagnetic material, turning permanent magnets of a motor or near current supply lines, see Section 2.2). Distributing multiple magnetometers across the whole robotic system and by applying the developed vMF-based fusion algorithm to the distributed magnetometer measurements, the developed approach can isolate the main source of interference and subsequently compensate the magnetic field distortion, as shown in the following sections.

6.1 Distributed Magnetometer Hardware Setup

In the setup of the first version of the multi-magnetometer developed in the course of this work, five very small and inexpensive magnetometers (ST LSM303D) and one microcontroller (Atmel ATmega 644P) were individually molded in polyurethane casting compound, resulting in a single cable whip (see figure 6.1) which can be easily and freely distributed outside an underwater vehicles' pressure housings.

Although most of the electronic parts on the microcontroller board are pressure-resistant due to their SMD package type, special care had to be taken of the hermetically sealed crystal oscillator providing the system's clock-signal to avoid col-

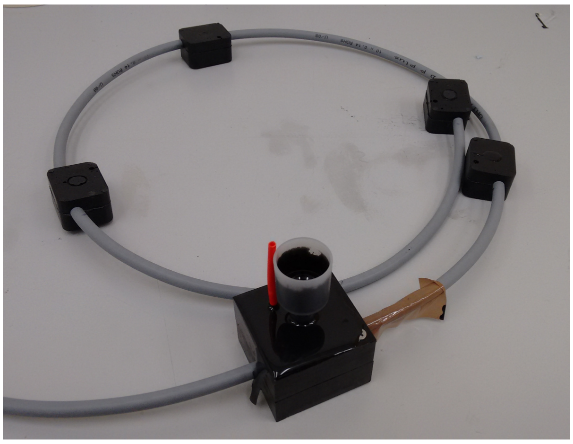

Figure 6.1: *Molding of distributed magnetometers using polyurethane casting compound*

lapse under high pressure [Kampmann et al., 2012]. Since the applied polyurethane is still quite flexible after curing (which is necessary to allow for a good and flexible bond with the cable), it is possible that the polyurethane would exert pressure on the crystal oscillator package. This would prevent the crystal from oscillating freely in a high-pressure surrounding, resulting in wrong clock frequencies or even fatal damage of the oscillator. Therefore, the package was sealed separately in epoxy resin, which is less compressible than polyurethane. To avoid inner tension in the epoxy which could lead to cracks in the material, micro balloons (hollow glass microspheres) were added to the epoxy casting compound, preventing the exertion of pressure on the oscillator housing during the curing process. The cast microcontroller module was integrated directly into the cable to avoid the necessity of another housing (see figure 6.2).

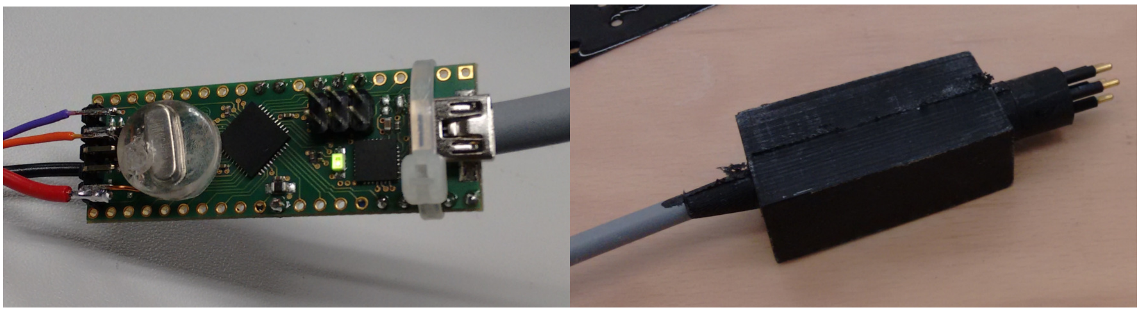

Figure 6.2: *Epoxy-infused crystal oscillator of microcontroller module (left), integrated with industry standard underwater plug (right)*

The ST LSM303D type of MEMS magnetometer that was used in this work can be interfaced using either I^{2}C or SPI. I^{2}C would have been the obvious choice due to the smaller amount of signal wires, however, since the magnetometer only allows two different I^{2}C slave addresses which would have required the integration of an additional multiplexer chip, the SPI interface was used in the first version of the multi-magnetometer.

SPI has several restricting limitations for this application, though: since it was primarily designed for short communication paths in embedded systems, the cable length is recommended to be limited to a few centimeters. However, in the first version of the multi-magnetometer, a maximum cable length of $1.5\,\mathrm{m}$ was possible with an SPI clock at $921.6\,\mathrm{kHz}$, but a longer cable whip led to dropout rates up to 100%, even when significantly reducing the bus clock. Furthermore, since SPI is a full-duplex system with a single master - multiple slave configuration, every additional magnetometer requires a separate slave select wire in the cable whip in addition to the power and communication wires. This was significantly restricting the number of magnetometers for a sensor array, in the first version to 5 sensors.

To overcome these restrictions and to be able to equip more magnetometers to the systems, a second version of the multi-magnetometer was developed, this time with a specific electronic design of the magnetometer modules to counter the experienced restrictions. The new sensor modules feature a dedicated microcontroller and RS485 communication chip on each module together with a voltage regulator allowing for a wider input voltage range from $3.6\,\mathrm{V}$ to $16\,\mathrm{V}$ to accommodate the heterogeneous voltage levels of different robotic systems (figure 6.3). The inter-chip communication between the microcontroller and magnetometer on each module is still SPI, and the communication of the modules with the robot on the RS485 bus at $921\,600\,\mathrm{bit\,s^{-1}}$ is triggered by the endpoint, polling the sensors sequentially for their data packages processed in parallel in the meantime. In addition to cyclic redundancy checking using *CCITT-CRC16*, *Consistent Overhead Byte Stuffing (COBS)* [Cheshire and Baker, 1999] was used to filter fixed start byte sequences in the sensor data.

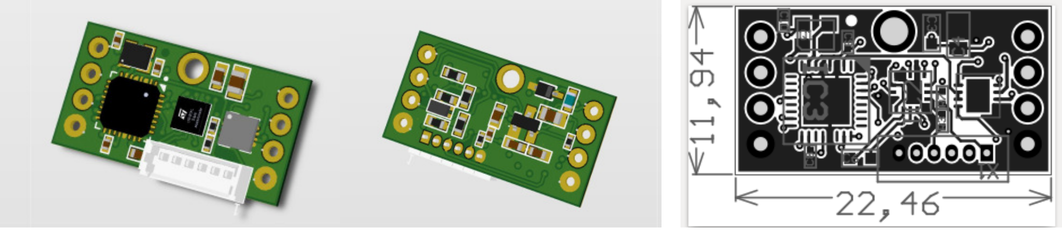

Figure 6.3: *Developed magnetometer sensor module (version 2) for the multi-magnetometer cable-whip setup*

The transition from SPI to the differential multipoint RS485 communication standard, with maximum specified data rates up to $10\,\mathrm{Mbit\,s^{-1}}$ and distances up to $1200\,\mathrm{m}$ at lower speeds [Telecommunications Industry Association et al., 2003], effectively removed the restriction on cable length and on the number of sensors of the first version and also made the extra microcontroller module obsolete. At the same time, the reduced size of the sensor modules of $12 \times 22.5\,\mathrm{mm}$, allowed for lower-profile molded units, further easing the installation on heterogeneous robotic systems. Figure 6.4 shows the multi-magnetometer setup produced for the robot *SherpaUW* with 8 magnetometers integrated into the cable-whip.

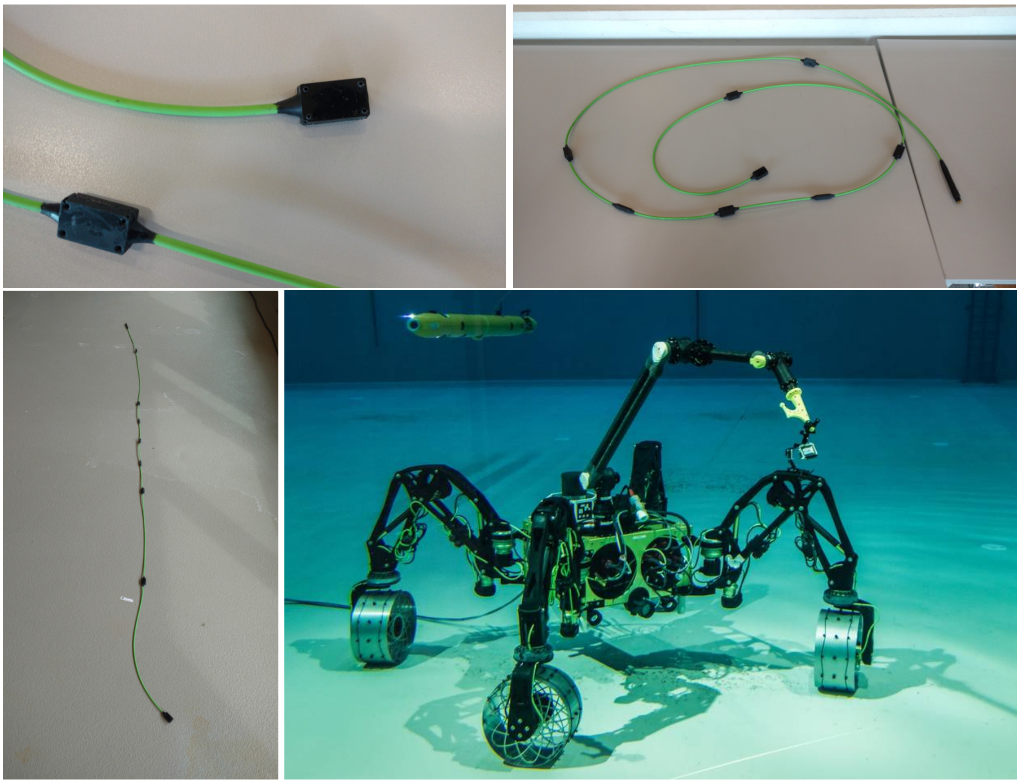

Figure 6.4: *Multi-magnetometer (v2) setup with 8 magnetometers integrated in the cable-whip tailored for and installed on the robot SherpaUW*

The developed distributed magnetometer setup was first deployed to the land-based robotic system *ARTEMIS* (see Section 5.3) and later to the following terrestrial robots and Unmanned Underwater Vehicles (UUVs) during the course of this work:

1. Rover *ARTEMIS*
2. *Pioneer AT* rover
3. Underwater hybrid rover *SherpaUW*
4. AUV *DAGON*
5. AUV *Flatfish*
6. AUV *Leng*

7. Underwater crawler *Wally*

A selection of these systems equipped with the developed multi-magnetometer system is displayed in figure 6.5.

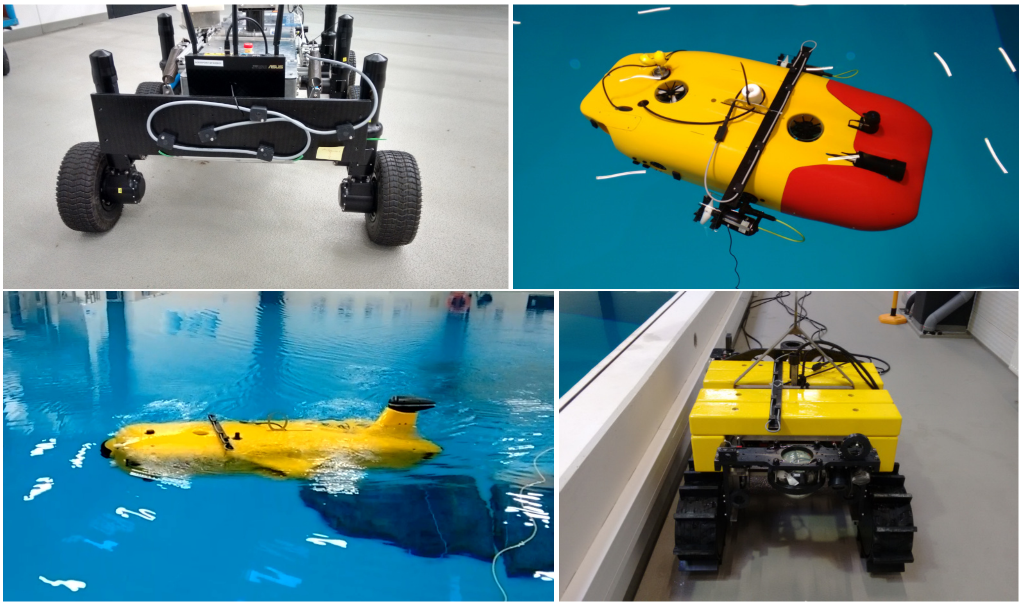

Figure 6.5: *Selection of robotic systems, that have been equipped with the developed multi-mangetometer throughout this work*

6.2 Static calibration

A compass application for heading estimation depends on measuring the horizontal components of the geomagnetic field to determine the direction towards the magnetic north pole. Although the pole's location is changing slowly over time and the magnetic field is significantly distorted locally depending on latitude and longitude of the observer, the declination from magnetic to true north can be computed using analytical models as described in Section 2.3.

Apart from the distortions of the geomagnetic field, the system-immanent distortions created by the vehicle itself must be taken into account, as discussed in sections 2.2 and 5. To recall: hard-iron effects occur due to the magnetic remanence of nearby material (permanent magnets in motors, magnetized iron or steel) and show a constant offset in every field component measured at the sensor position. Without distortions, plotting directions on a S^2 sphere in $\mathbb{R}^3$ would result in measurements of arbitrary direction having the same distance to the origin. In contrast, hard-iron distortions lead to a shift of the center of the sphere from the origin (see figure 6.6) and can be

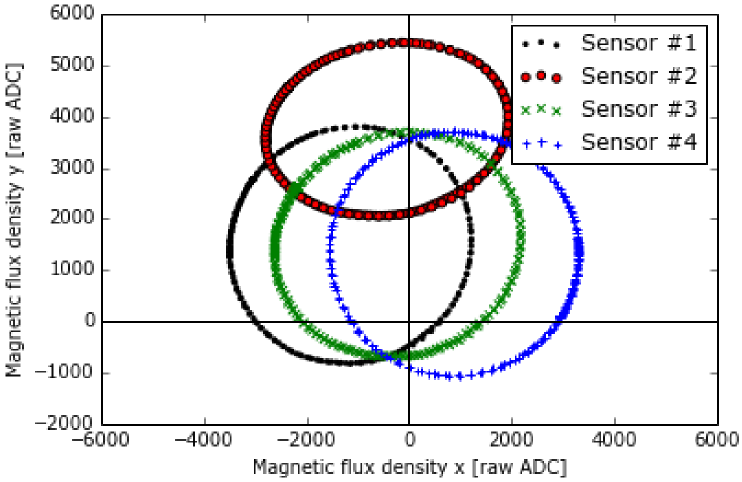

Figure 6.6: *Hard-iron distortion and sensor misalignment on robotic crawler Wally, magnetometer readings projected onto the xy-plane leading to off-center effects of different strength depending on mounting position on the vehicle. Ideally (without distortions), all measurements would result in perfect circles centered at the origin.*

modeled as a 3-component bias vector b_{hi} (one-cycle error):

$$b_{hi} = \begin{pmatrix} x_{hi} & y_{hi} & z_{hi} \end{pmatrix}^T \tag{6.1}$$

Please note, that strong currents flowing through wires near the magnetometers also lead to hard-iron effects, but are usually non-static. How to deal with these dynamic distortions is described in Section 6.3 and in Chapter 7.

Soft-iron effects distort the magnetic field by providing a path of lower impedance while an external field is applied to the ferromagnetic compound. This induces magnetism depending on the orientation of the material with respect to the applied (geomagnetic) field (two-cycle error). As such, soft-iron effects lead to a deformation of the sphere to a 3D ellipsoid, but retaining the origin. The soft-iron effects can be described by a 3×3 matrix M_{si}:

$$M_{si} = \begin{pmatrix} m_{11} & m_{12} & m_{13} \\ m_{21} & m_{22} & m_{23} \\ m_{31} & m_{32} & m_{33} \end{pmatrix} \tag{6.2}$$

Before the application of the proposed vMF-based filter to compensate dynamic distortions of the measured magnetic flux density field, one has to account for the static vehicle hard- and soft-iron distortions. In order to get calibrated sensor readings $\hat{b}_x, \hat{b}_y, \hat{b}_z$ from raw sensor readings b_x, b_y, b_z, the following equation is applied:

$$\begin{pmatrix} \hat{b}_x \\ \hat{b}_y \\ \hat{b}_z \end{pmatrix} = M_{align} \cdot \begin{pmatrix} sc_x & 0 & 0 \\ 0 & sc_y & 0 \\ 0 & 0 & sc_z \end{pmatrix} \cdot M_{si} \cdot \left(\begin{pmatrix} b_x \\ b_y \\ b_z \end{pmatrix} - b_{hi} \right) \tag{6.3}$$

with the misalignment matrix M_{align}, a diagonal scale matrix SC, soft-iron distortion matrix M_{si} and offset vector b_{hi}, which incorporates hard-iron distortions as well as sensor-immanent ADC offset errors. As stated previously, undistorted or perfectly compensated magnetic field flux density readings would cover the surface of an origin-centered sphere, while hard- and soft-iron distortions, as well as sensor errors, lead to an off-centered ellipsoid, which can be modeled as a second-order algebraic surface.

Not taking cross-axis effects into account, this ellipsoid can therefore be described as:

$$\frac{(b_x - x_{hi})^2}{a^2} + \frac{(b_y - y_{hi})^2}{b^2} + \frac{(b_z - z_{hi})^2}{c^2} = R^2 \tag{6.4}$$

In order to apply least-squares ellipsoid fitting methods to discover the correction parameters for hard- and soft-iron distortions, sensor bias and scaling, Equation 6.4 is rewritten to

$$\begin{pmatrix} b_x & b_y & b_z & -b_y^2 & -b_z^2 & 1 \end{pmatrix} \cdot X = b_x^2 \tag{6.5}$$

with

$$X = \begin{pmatrix} 2x_{hi} \\ \frac{a^2}{b^2} 2y_{hi} \\ \frac{a^2}{c^2} 2z_{hi} \\ \frac{a^2}{b^2} \\ \frac{a^2}{c^2} \\ a^2R^2 - x_{hi}^2 - \frac{a^2}{b^2} y_{hi}^2 - \frac{a^2}{c^2} z_{hi}^2 \end{pmatrix} \tag{6.6}$$

which is the linear equation system

$$H \cdot X = w = x^2 \tag{6.7}$$

which can be solved by a least-squares solver.

A set of uncalibrated values of b_x, b_y and b_z would ideally be sampled from every sensor in the multi-magnetometer array in a distortion-free magnetic field environment and evenly cover the full space of 3D directions. Unfortunately, full-circle turns in every vehicle axis (roll, pitch and yaw) usually cannot be performed, since this would involve either sophisticated and huge gimbals for the systems in air and underwater, or vehicles with the possibility to turn around all their axes by themselves, if possible at all (e.g. not possible for stable AUVs or crawlers). Also, this would induce non-static distortions to the static calibration process. However, since the distortion model is already restricted to a quadratic ellipsoid surface, a sparse sampling with a full 360° yaw circle, but only involving roll and pitch movement from -20° to +20°, is sufficient to recover the ellipsoid from the uncalibrated data (see figure 6.7). The turn-and-wiggle motion in case of the static calibration procedure for the crawler *Wally* was conducted as far away from any steel structure as possible while being attached to a crane on a 6m polyester hoisting sling.

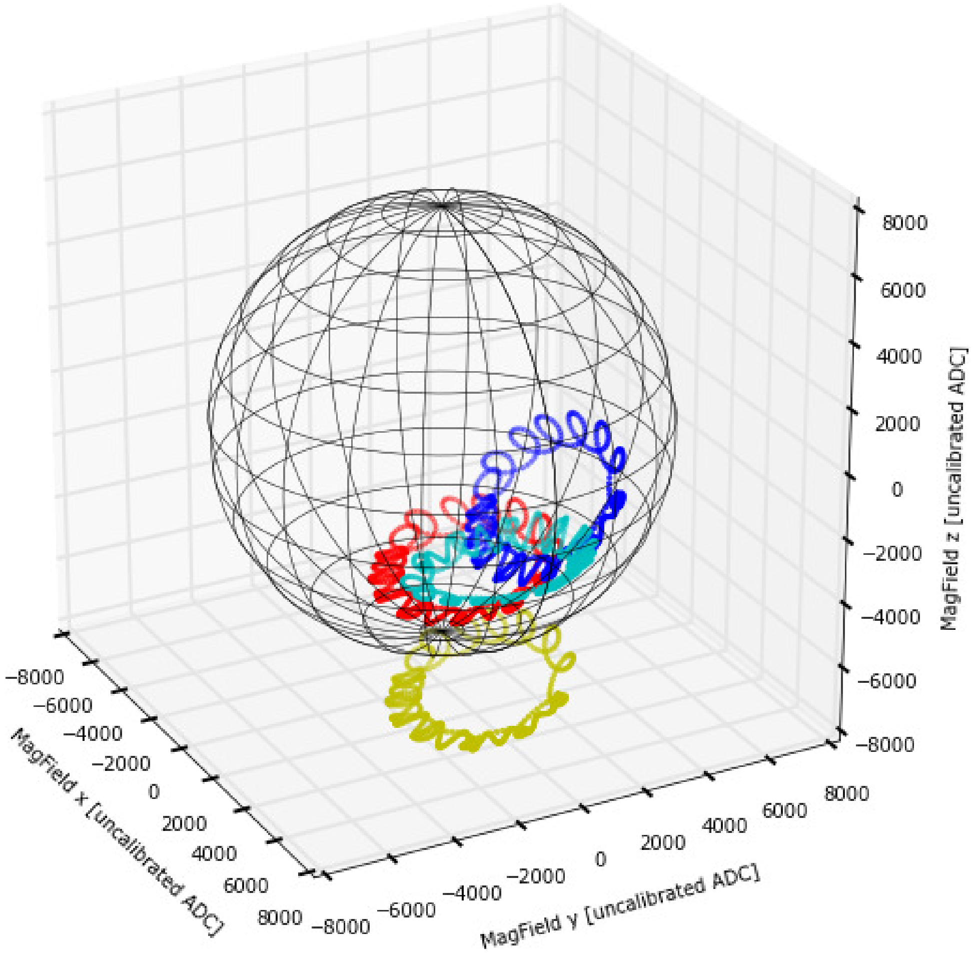

Figure 6.7: *Scatter plot of uncalibrated ADC magnetometer readings on robotic crawler Wally during static calibration procedure*

After solving for the combined scale matrix SC and soft-iron distortion matrix M_{si}, as well as the combined sensor bias and hard-iron offset vector b_{hi}, only the misalignment matrix M_{align} has to be established. To achieve this, several flat turns around the respective vehicle's yaw axis were carried out, avoiding any roll and pitch movements and taking care to do so in the most uniform magnetic field environment available.

Apart from small non-orthogonalities in the sensors themselves, the misalignment matrix is basically a rotation matrix that turns the sensor frame to the fixed body frame of the vehicle. Note, that this step in the calibration process allows to freely distribute the sensors from the multi-magnetometer across the system, without the need for an exactly known position or pose, as long as the sensors are rigidly fixed to the vehicle body. Since a rotation can be described with a minimum of 3 degrees of freedom, direct least-squares solving for all 9 values of the 3×3 rotation matrix would not guarantee a pure rotation matrix, thus Rodriguez' rotation formula is used:

$$\mathbf{v}_{\mathrm{rot}} = \mathbf{v}\cos\theta + (\mathbf{k} \times \mathbf{v})\sin\theta + \mathbf{k}(\mathbf{k} \cdot \mathbf{v})(1 - \cos\theta) \tag{6.8}$$

which rotates a vector v around a unit vector rotation axis k by an angle of θ resulting in $\mathbf{v}_{\mathrm{rot}}$ and least-squares solve for k and θ with v being the distortion-compensated sample from the flat turn around the vehicle's z-axis and $\mathbf{v}_{\mathrm{rot}} = \begin{pmatrix} 0 & 0 & -1 \end{pmatrix}^T$.

From that, the misalignment matrix M_{align} can be computed as:

$$\mathbf{M}_{\mathrm{align}} = \mathbf{I} + (\sin\theta)\mathbf{K} + (1 - \cos\theta)\mathbf{K}^2 \tag{6.9}$$

with

$$\mathbf{K} = \begin{bmatrix} 0 & -k_3 & k_2 \\ k_3 & 0 & -k_1 \\ -k_2 & k_1 & 0 \end{bmatrix} \tag{6.10}$$

Putting everything together, figure 6.8 and figure 6.9 show the compensated and aligned magnetometer readings on the crawler *Wally*.

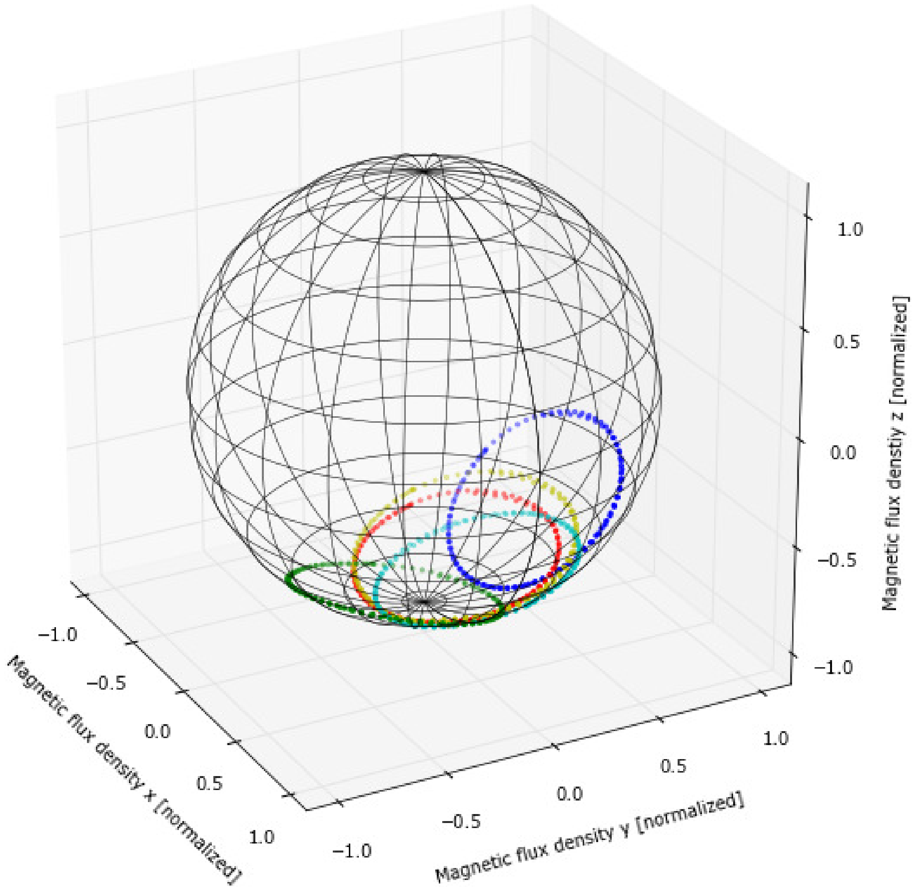

Figure 6.8: *Scatter plot of compensated but still unaligned readings of the magnetometers distributed on crawler Wally during the static calibration procedure (flat turns around yaw axis*

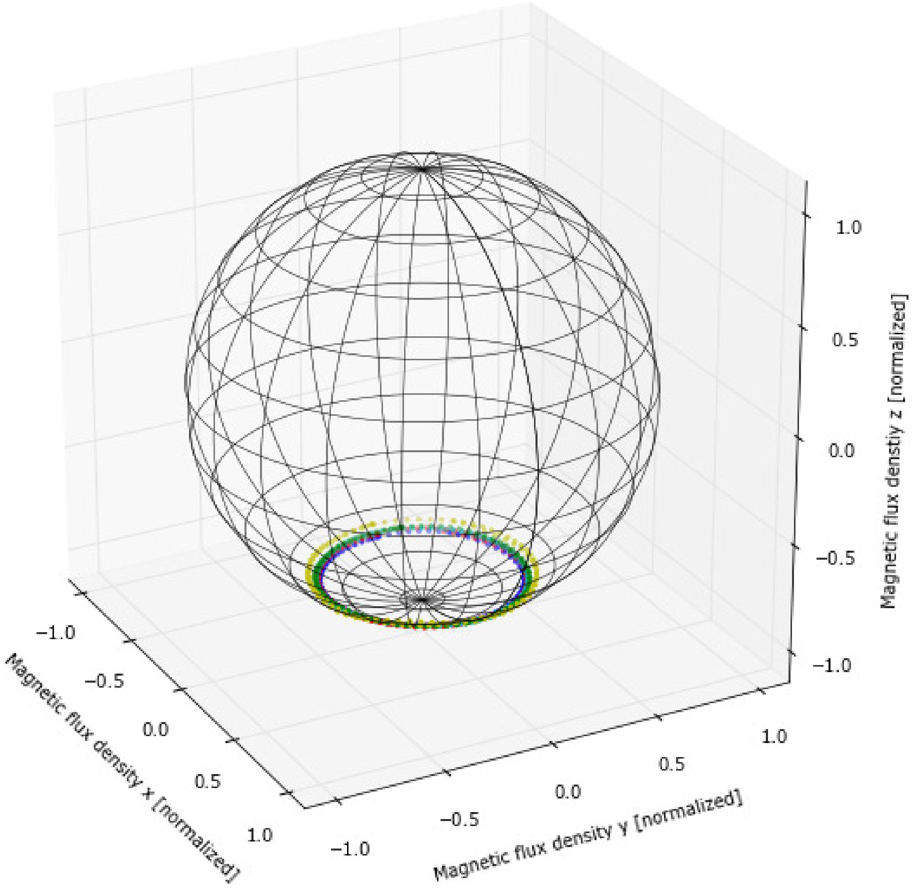

Figure 6.9: *Scatter plot of compensated and aligned readings of the magnetometers distributed on crawler Wally during the static calibration procedure (flat turns around yaw axis*

The described a priori calibration procedure thus demonstrates the ability to account for local *static* distortions of a vehicle as well as the misalignment errors and unknown orientations of the multi-magnetometer sensors distributed over a robot. This drastically reduces the effort and time needed to integrate the developed multi-magnetometer system on a vehicle, compared to finding an appropriate installation location for conventional single-device compasses.

Figure 6.10 shows a zoomed in part of a SLAM generated magnetic map of a large indoor environment inside the RH1 building of the DFKI RIC. The map was generated using the proposed multi-magnetometer system and the described calibrated procedure on the robot *ARTEMIS*. It can be seen, that the magnetic field readings of all magnetometers in the array are still coherent with earlier measurements when revisiting previous locations, even when the robot was oriented in the opposite direction.

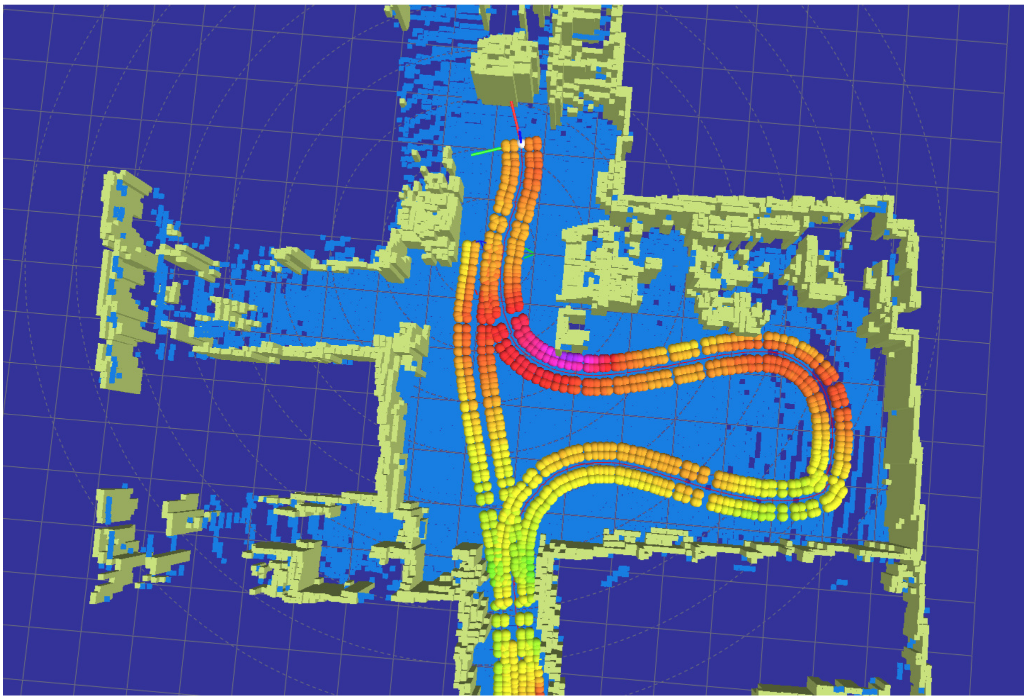

Figure 6.10: *SLAM generated map of larger indoor environment inside building RH1 of the DFKI RIC using the proposed multi-magnetometer setup on robot ARTEMIS. Please note the coherent readings when revisiting previous locations, even when oriented in the opposite direction*

6.3 vMF Consensus Filter Algorithm

Apart from *static* distortions local to the vehicle, which can be accounted for by an *a priori* calibration procedure (see Section 6.2 above), the local *dynamic* distortions have to be compensated online.

In the approach described in this section, the idea is to filter these dynamic effects by means of multiple small sensors freely distributable on the vehicle. This makes it not only possible to mount the sensors farther away from the distortion source than a single large high-precision IMU, but since the dynamic distortions of the magnetic field are usually locally distributed and show up only in a subset of the sensors, this setup is suitable for the application of statistical filtering.

vMF Distribution

Since the magnetic field is a vector field, dynamic distortions have an effect both on the magnetic flux density (strength component) as well as on its direction. Sometimes even strong distortions only result in a variation of the field strength (maintaining the direction), while other distortions don't change the magnetic field strength, but result in large direction deviations. This characteristic due to the inherent physics suggests to use a spherical representation with individual direction and strength component, rather than the 3 isolated components of a cartesian representation.

Thus, to determine the extent to which one sensor in the array is disturbed with respect to the rest of the magnetometer sensors on the vehicle, the probabilistic density functions of two different 3-dimensional multivariate probabilistic distributions are used, one for the strength and one for the directional component. Interested in the probability of a measurement $\mathbf{x}_i$ of sensor i given a set of measurements of the rest of the sensors, we model the strength component as a Gaussian distribution of the $L2$-norm with mean μ_{st} and standard deviation σ. The probability density function for the strength component is therefore defined as

$$p(\mathbf{x}_i|\mu_{st},\sigma) = \frac{1}{\sigma\sqrt{2\pi}}\, e^{-\frac{(x-\mu_{st})^2}{2\sigma^2}} \tag{6.11}$$

To model the three-dimensional direction component, this work makes use of the vMF distribution [Fisher, 1953], originating from directional statistics and commonly used in paleomagnetics, analog to circular wrap-around distributions in the one-dimensional case. The vMF distribution is defined on the S^{p-1}-dimensional sphere in

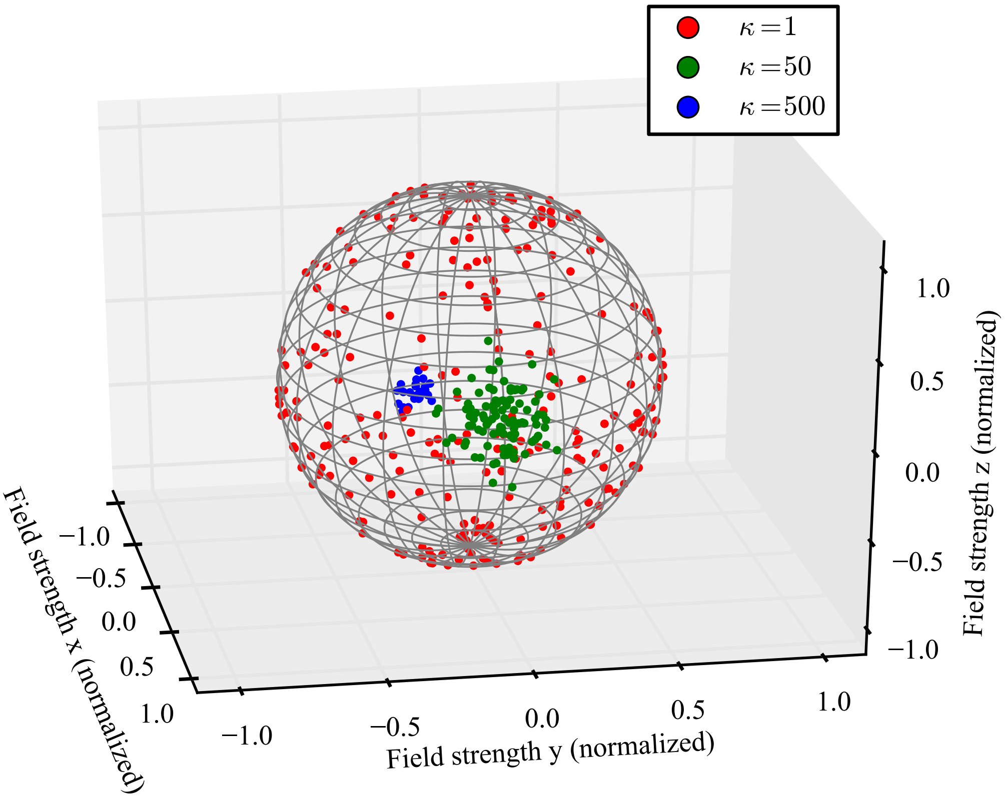

Figure 6.11: *Samples from three different vMF-distributions on S^2 with different mean and $\kappa = 1$ (red), $\kappa = 50$ (green) and $\kappa = 500$ (blue)*

$\mathbb{R}^p$. The probability density function of a vMF distribution on S^2 is given by

$$p(\mathbf{x_i}|\mu_{dir}, \kappa) = \frac{\kappa}{4\pi \sinh \kappa} \exp(\kappa \mu_{dir}^T \mathbf{x_i}) \tag{6.12}$$

with mean direction μ_{dir} and concentration parameter κ for a unit direction vector x. In case of $\kappa = 0$, the distribution is uniform while it is more concentrated with higher κ (see figure 6.11).

μ_{dir} can be approximated as

$$\hat{\mu}_{dir} = \frac{\mathbf{r}}{\|\mathbf{r}\|} = \frac{\sum_{i=1}^{n} \mathbf{x_i}}{\|\sum_{i=1}^{n} \mathbf{x_i}\|} \tag{6.13}$$

and κ according to [Banerjee et al., 2005] and as proposed for small dimensions by [Sra, 2012] as

$$\hat{\kappa} = \frac{\bar{r}p - \bar{r}^3}{1 - \bar{r}^2} \tag{6.14}$$

with

$$\frac{\|\mathbf{r}\|}{n} = \bar{r} \tag{6.15}$$

Combining both strength and direction components, the probability of a measurement x_i of sensor i given the current Gaussian distribution of the strength (magnetic field flux density) and the actual vMF distribution of the direction can then be computed as:

$$p(\mathrm{x}_i|\mu_{st},\sigma)\cdot p(\mathrm{x}_i|\mu_{dir},\kappa) = \frac{1}{\sigma\sqrt{2\pi}}\, e^{-\frac{(x-\mu_{st})^2}{2\sigma^2}} \cdot \frac{\kappa}{4\pi\sinh\kappa}\exp(\kappa\mu_{dir}^T\mathbf{x_i}) \tag{6.16}$$

Equation 6.16 is representing the general probabilistic measurement model for magnetic field measurements used not only for the following compensation algorithm, but for all probabilistic estimators and localization filters in this work.

Filter Implementation

Now that the probability of the current measurement x_i of sensor i in the sensor array of size n can be computed, every measurement x_i is given a weight w_i according to its probability, so that measurements strongly deviating from the rest of the measurements influence the result less.

```
function VMF_CONSENSUS_FILTER
    for $i \leftarrow 1$ to $n$ do
        $\mathrm{x}_i \leftarrow readout\_magnetometer(i)$
    end for
    $\mu_{st}, \sigma \leftarrow$ mean and std of strength (L2 norm)
    $\mu_{dir}, \kappa \leftarrow$ mean and concentration parameter of vMF distribution
    $w_i \leftarrow p(\mathrm{x}_i|\mu_{st},\sigma)p(\mathrm{x}_i|\mu_{dir},\kappa)$
    return normalized weighted sum of x
end function
```

The result can either be used standalone as the normalized weighted sum or each sensor can be integrated as a single measurement in a higher level sensor fusion algorithm (see section 3.1) with per-sensor confidence values according to the computed weight.

6.4 Results

Experiments to validate the multi-magnetometer approach were conducted on the unmanned underwater crawler *Wally* and the hybrid AUVs *Dagon* and *FlatFish* at the DFKI underwater robot test facilities. Several data acquisition runs were carried out, amongst them static setups, straight driving, circling and wall following.

Figure 6.12 shows the calculated heading of the first 5 sensors after static calibration during a manually steered straight run with *DAGON* in the DFKI underwater test basin of 1.5 minutes duration. Also plotted is the heading calculation of a high-precision FOG as reference. As can be seen, strong dynamic distortions occur in sensor number 0, due to the mounting position near a sonar transducer with strong current peaks during active acustic pulses. Please note that the proposed hardware setup of the multi-magnetometer system (with the availability of several sensors at different positions outside the pressure hull and farther away from possible disturbance sources) already allows for much less distorted magnetometer readings of other sensors (here sensors 1-4).

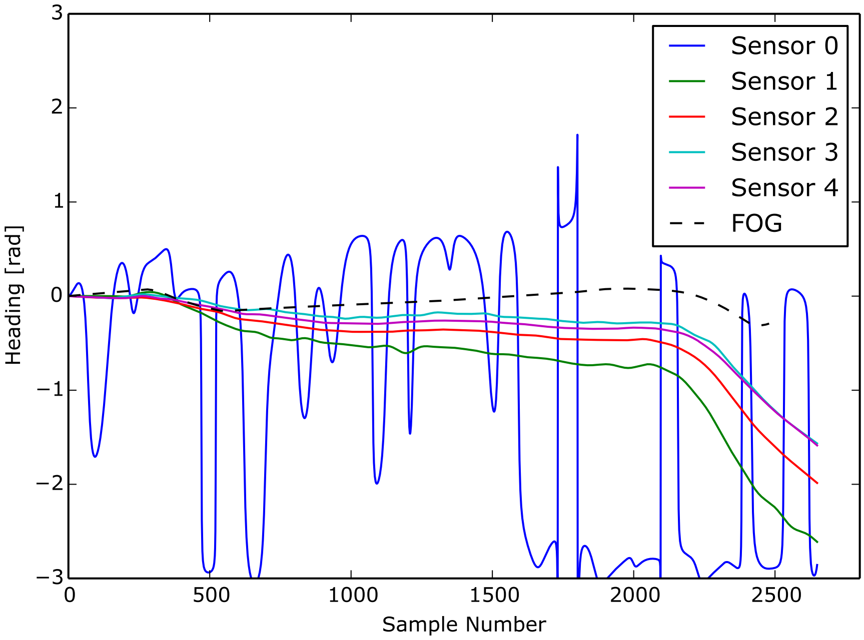

Figure 6.12: *Calculated heading of single sensors after static calibration during Dagon straight run in the DFKI underwater test basin*

Figure 6.13 shows the performance of the proposed method in the presence of local dynamic distortions as they are expected to appear on confined UUVs, in this case on the AUV *Dagon*. As can be seen, the proposed dynamic filter using vMF-distributions performed better as an averaging-filter due to the algorithmic design, which in this case assigns a low weight to the deviating sensor 0 with respect to the confidence from similarity of rest of the sensors (1-4), although there still is a divergence between the reference high-precision FOG-heading and the filtered solution using MEMS sensors of drastically lower costs.

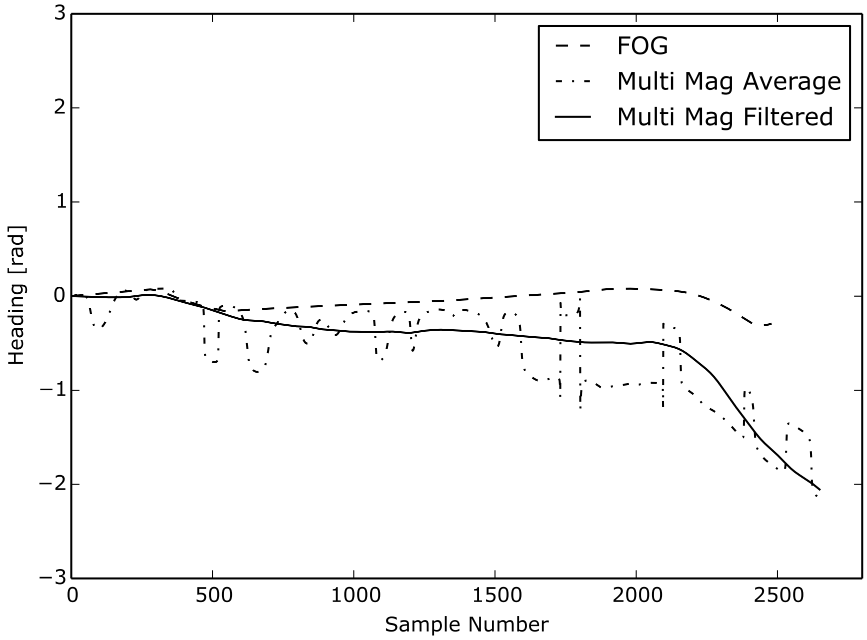

Figure 6.13: *Comparison of averaged and proposed dynamical filtering of the magnetometer array readings during Dagon straight run in the DFKI underwater test basin*

6.5 Conclusion

In this section, a new approach to deal with dynamic distortions of the ambient magnetic field often leading to errors in orientation estimation in confined UUVs was described. A small distributed and pressure-neutral sensor array design to remove mounting restrictions was proposed and was successfully interfaced with several different robotic underwater systems and was evaluated at the DFKI RIC underwater test facility. To improve the robustness of magnetometer/compass readings, a new multi-magnetometer fusion algorithm using von Mises-Fisher (vMF) distributions was applied and showed its performance in the presence of strong local vehicle distortions. In addition to the development of the algorithm, a python software library to handle vMF distributions has been developed and is currently in the process of being made available as open-source.

Considering the performance, one has to keep in mind, that the hardware-based multi-magnetometer approach allows dealing with dynamic distortions, even without access to the internal data of the vehicle. Although the machine learning approach discussed in the next chapter is showing a better overall performance in specific setups (Chapter 7), the ML-approach is strictly dependent on the availability of real-time data of the internal robot state like posture, motor currents, etc. In comparison, the multi-magnetometer system described here can be deployed without much effort as a standalone add-on system, in the simplest case just acting as a pressure-tolerant strap-down compass with enhanced robustness against system distortions.

Chapter 7

Magnetic Field Distortion Learning

This chapter describes the use and evaluation of machine learning techniques like neural networks and support vector regression to learn a model of magnetic field distortions often induced in inertial measurement units using magnetometers by changing currents, postures or configurations of a robotic system as shown in Chapter 5. Such a model is needed in order to compensate the local dynamic distortions, especially for complex and confined robotic systems, and to achieve more robust and accurate ambient magnetic field measurements. This is crucial for a wide variety of autonomous navigation purposes from simple heading estimation over standard SLAM approaches to the more specific magnetic field-based localization techniques addressed in this work. The approach was evaluated both in a laboratory setup and with a complex robotic system in an outdoor environment.

As discussed in the chapters before, in order to fully exploit the benefits of an almost omnipresent geomagnetic field (Section 2.3), or the more specific features of the local ambient magnetic field (Chapter 4), one has to properly deal with the problem of significant dynamic magnetic field distortions (Section 2.2) caused by ferromagnetic materials or strong electric currents near the magnetometer originating from the robotic system itself (Chapter 5). This specifically applies to systems with restricted sensor mounting options far away from distortion sources, for example on very compact robots or autonomous underwater vehicles with pressure housings, but also on complex systems with a lot of moving parts or reconfiguration options like the hominid walking robot *CHARLIE*. As shown in Section 5.4, the magnetic field readings on such a system can be significantly distorted, both in the strength and in the direction component, in the worst cases (depending on the walking pattern) up to complete direction reversals. A single IMU with an integrated magnetometer mounted near a source of such distortions would render any pose estimation based on that information useless.

One approach to tackle such disturbances is the use of a multi-magnetometer sensor array with according filter algorithms as discussed in Chapter 6. However, especially for systems where there is realtime access to the proprioceptive data or *embodied information* (for terminology see [Schwendner and Kirchner, 2010, Schwendner, 2013]), for example the limb positions and motor currents, this extra information should be used. For this purpose, a solution using machine learning techniques to learn a model of magnetic field distortions was proposed by the author of this work in [Christensen et al., 2017] and is described in more detail in the following sections.

7.1 Hybrid Legged-Wheeled Intervention Rover *SherpaTT*

Figure 7.1: *The hybrid legged wheeled robot SherpaTT with a high amount of degrees of freedom and therefore high amount of magnetic field distortion sources during field trials in the desert of Utah, US*

To evaluate the machine learning approach to compensate dynamic distortions based on embodied data, the hybrid legged-wheeled intervention rover *SherpaTT* was used (figure 7.1). *SherpaTT* is a hybrid walking and driving rover with 4 active suspension units with 5 DoF each, casted from aluminium (the "legs" of the system) and a 6 DoF manipulator on equipped on the top. *SherpaTT* was developed for high mobility in irregular terrain, and can adapt its posture and execute walking patterns to overcome

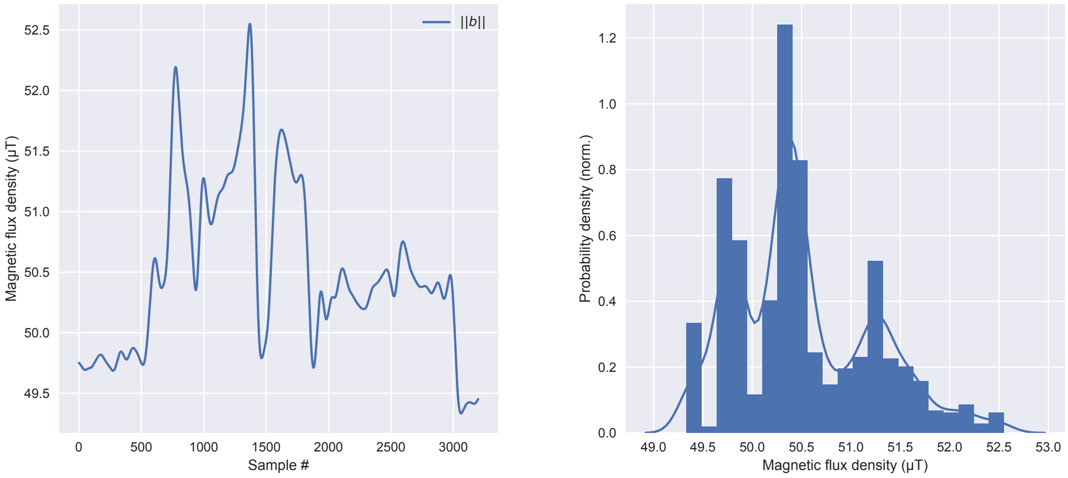

Figure 7.2: *Total field strength variations (left) and according distribution (right) on rover SherpaTT during magnetic field distortion data set gathering in the desert of Utah, US*

obstacles [Cordes and Babu, 2016, Cordes et al., 2018]. The rover also features multiple electro-mechanical interfaces, where modular payloads can be docked to. The rover was chosen in this work because of this flexible configurations, different kinds of locomotion and the massive amount of DoF, all of which can substantially distort the local magnetic field.

Figure 7.2 shows the variations of the total magnetic field strength, with *SherpaTT* executing changes of its stance (for details on the experiments see section 7.3 below).

Although the distribution, in comparison with the walking robot *CHARLIE* (see Section 5.4), is not significantly spread out with a lower quartile of $49.87\,\mu\mathrm{T}$ and an upper quartile of $51.02\,\mu\mathrm{T}$ around the median of $50.39\,\mu\mathrm{T}$, the changes in the direction are severe, as depicted in figure 7.3.

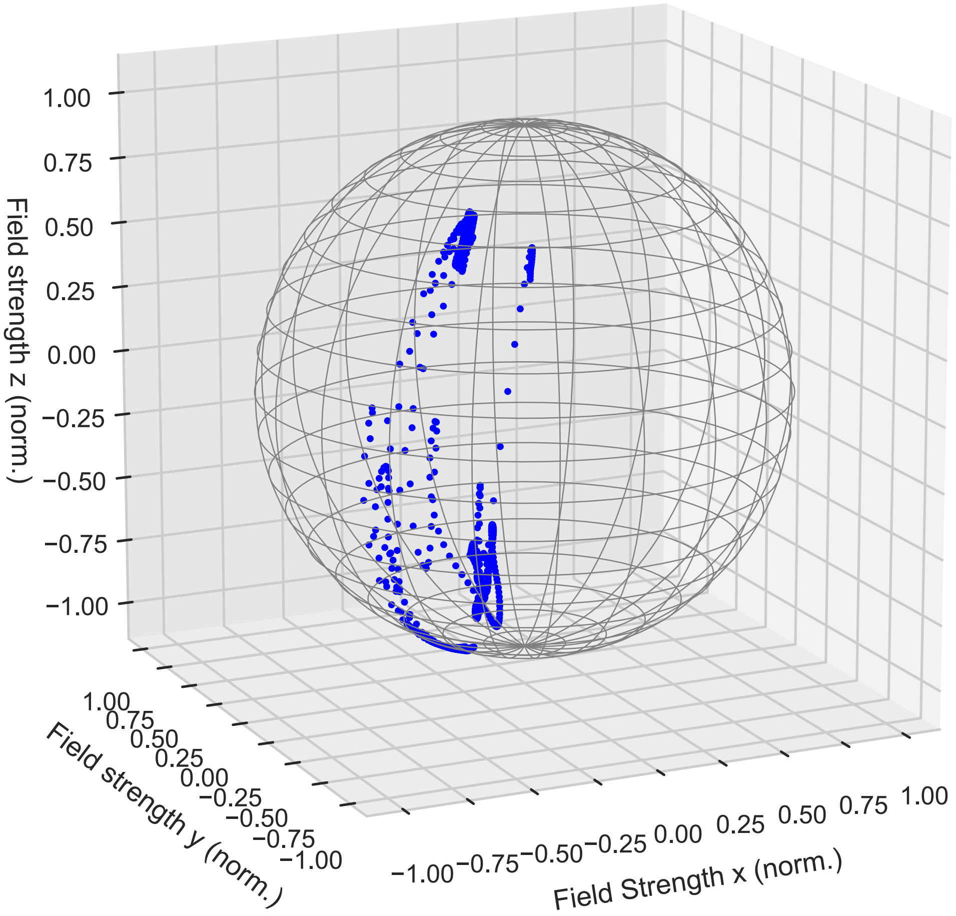

Figure 7.3: *3D scatter plot of dynamically distorted directions on SherpaTT while changing the stance posture*

7.2 Dynamic Distortion Model Learning

System-immanent dynamic disturbances are a strong contributor to distortions of the otherwise evenly distributed ambient magnetic field, especially in complex and confined robotic systems, as just shown for the rover *SherpaTT* and discussed in general in Section 2.2. To be able to use the ambient magnetic field for orientation or localization purposes in the first place, the dynamic distortions have to be compensated for.

The rationale behind the chosen approach is, that in most recent robotic systems there is a huge amount of proprioceptive sensor data available at runtime that can help to deduct the magnetic field distortions emanating from the system. For example, one often has means to measure the actual currents flowing through wires or torques applied to the motors. Apart from full reflex-driven robots, most of the time there is quite accurate data on the relative position of extremities and appendages of the robotic system (e.g. in legged robots) as well as current state information (e.g. attached payloads or robot configuration) in reconfigurable robots. While it is possible to facilitate some simplifications and model certain distortions as bar magnets, the sheer amount of contributing and intertwined magnetic field distortion sources in the systems in consideration almost always renders the formulation of an analytical solution impossible. The approach here is therefore to learn a function f of the resulting and superimposed distortions at the point of the magnetometer sensor from the proprioceptive sensor data of a robotic system (figure 7.4).

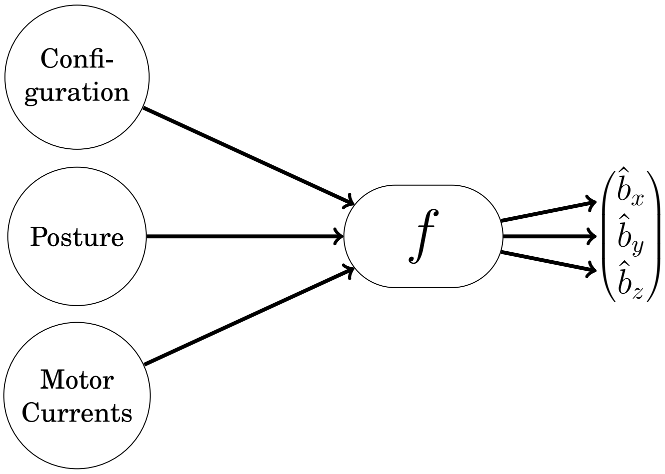

Figure 7.4: *Multi-target function regression approach with robot posture, motor currents and present configuration (e.g. attached payloads, etc. in case of reconfigurable robots)*

The target to be learned is in our case a 3D offset vector of the magnetic field, combining hard- and soft-iron distortions. The problem falls therefore in the class of multi-target function regression. To evaluate the approach with different regression techniques and meta-parameter optimization, the *scikit-learn* framework [Pedregosa et al., 2011] in combination with the robotic framework *Rock* [Rock, 2013] was used.

In this approach, two different popular regression methods, a) Support Vector Regression (SVR) and b) Multilayer Perceptron Regression (MLP) were chosen. The SVR primarily due to the limited number of hyperparameters that have to be tuned and their guaranteed global optimum, and the MLP due to their flexibility and capability to directly train multi-target regressors.

Support Vector Regressor

The basic concept of SVR is similar to the more commonly known approach of Support Vector Classification (SVC). With SVC, a linear function to separate the features is searched for, in nonlinear cases by projection into higher dimensions. An SVR attemps to approximate a function by finding the narrowest ϵ-tube centered around the data, i.e. the distances between the learned function and the given values in the training data should be less than epsilon [Vapnik, 2000], while minimizing the prediction error (see figure 7.5).

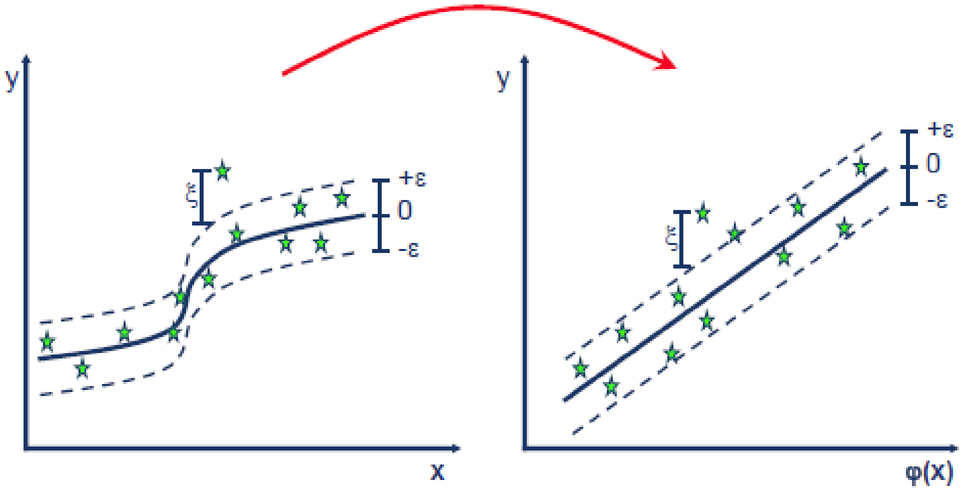

Figure 7.5: *Principle of non linear support vector regression (SVR), trying to find the narrowest ϵ-tube around the training data while minimizing the prediction error [Sayad, 2019]*

Larger errors are linearly penalized. Furthermore, a regularization term is preferring smooth functions with small weights. The weighting between error (loss) and regularization (small weights) is done with a regularization constant C. For modeling complex functions, the so-called *kernel trick* is applied [Smola and Schölkopf, 2004, Chang and Lin, 2011], using a Radial Basis Function (RBF) kernel with an additional hyperparameter γ, that defines the influence of a single training example:

$$e^{(-\gamma \cdot \|x_i - x_j\|^2)} \tag{7.1}$$

With the standard SVR approach being single-target, one has to train one support vector machine for each of the three dimensions of the target offset vector, which somewhat neglects the fact, that these 3 components are inherently coupled, because they describe a magnetic flux density vector, incorporating field orientation and strength.

Multilayer Perceptron Regressor

A neural network in the form of a multilayer perceptron regressor (MLP) can innately represent coupling between components and directly be trained for multi-target regression in contrast to an SVR. In our case, the input layer represents the different commands and sensor inputs that can influence the magnetic field measurement and the output is a representation of the different deflected components of the magnetic field like directions and strength. The core components of an MLP are perceptrons that linearly weight the different inputs and apply a gating/activation function afterward [Hinton, 1989]. Each layer of an MLP consists of several perceptrons that are not connected to each other but to all perceptrons in the preceding and the follow-up layer. For learning the weights of the single perceptrons, numerous optimization strategies can be used that are often able to handle huge amounts of data [Glorot and Bengio, 2010].

7.3 Experiments

In order to evaluate the overall compensation performance of the chosen approach, e.g. how well the learned model can keep the directional component of the magnetometer measurements stable in the presence of local dynamic magnetic field distortions, experiments with an artificial distortion turntable setup as well as with the hybrid wheeled-legged robot *SherpaTT* were conducted. The tests were performed in a very noise-free environment in the Mars-like desert of Utah, US, as part of an extended field trial period with a team of heterogeneous robotic systems [Sonsalla et al., 2015, Sonsalla et al., 2017, Cordes et al., 2018].

As introduced in Chapter 6, two different probabilistic distributions for strength and direction are used, this time to compare the compensation performance.

To recall, the strength component is modeled as a Gaussian distribution of the $L2$-norm with mean μ_{st} and standard deviation σ, with the corresponding probability density function defined as

$$p(\mathbf{x}_i|\mu_{st},\sigma) = \frac{1}{\sigma\sqrt{2\pi}}\, e^{-\frac{(x-\mu_{st})^2}{2\sigma^2}} \tag{7.2}$$

To model the direction component, the *von Mises Fisher* (vMF) distribution is used as explained in Section 6.3 and defined on the S^{p-1}-dimensional sphere in $\mathbb{R}^p$ with the probability density function of a vMF distribution on S^2 by

$$p(\mathbf{x_i}|\mu_{dir},\kappa) = \frac{\kappa}{4\pi \sinh \kappa} \tag{7.3}$$

with mean direction μ_{dir} and concentration parameter κ for a unit direction vector x. $\kappa = 0$ means uniform distribution, while it is more concentrated with higher κ (see figure 6.11), in our application, higher kappa means better directional compensation.

Magnetic Field Distortion Turntable

In order to test the approach with very defined and separable distortion sources, an artificial turntable setup as shown in figure 7.6 was developed.

To resemble hard-iron distortions a neodymium magnet was mounted to a lever-arm (denoted ’1’ in figure 7.6), moving $90°$ arc-wise towards the magnetometer mounted in the center of the turntable. To emulate soft-iron distortions, a $1\,\mathrm{kg}$ $99.9\,\%$ pure iron block (2) was moved $6\,\mathrm{cm}$ linearly towards and away from the sensor. And finally, to

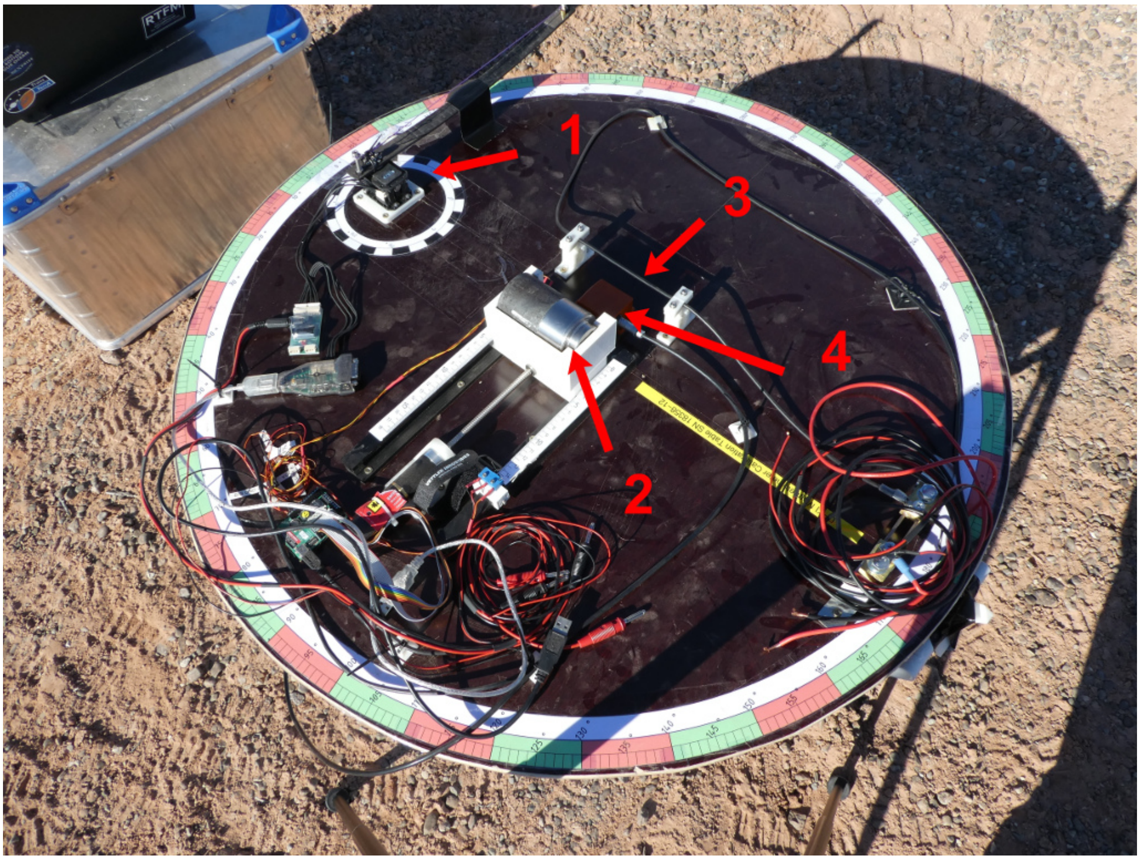

Figure 7.6: *Magnetic distortion turntable setup with individually engageable distortion sources: arcwise movable neodymium magnet for hard-iron effects (1), linearly displaceable pure iron block for soft-iron effects (2) and a copper conductor wire (3) for electromagnetic effects. (4) indicates the position of the mangetometer.*

simulate electromagnetic distortions from motor supply currents, a $6\,\mathrm{mm}^2$ wire (3) was fixated close to the sensor (4). The material of the setup was chosen in order to minimize magnetic distortion sources different from those named above. Furthermore, every piece of equipment brought to the experimental site was validated to not interfere with the experimental setup (figure 7.7).

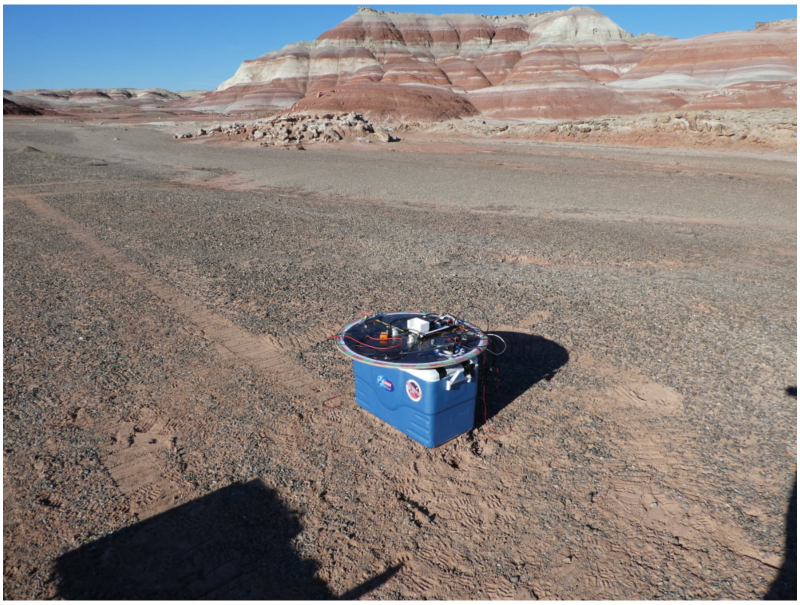

Figure 7.7: *Magnetic distortion turntable experiment setup in the nearly magnetic noise-free desert of Utah, US*

During data recording, every distortion source activity was activated individually and then simultaneously. In each trial, the hard iron source lever was moved 90° twice in an arc towards the sensor. The soft iron source was moved once towards the sensor and then back, while the current was raised from $0\,\mathrm{A}$ to $20\,\mathrm{A}$ and back to $0\,\mathrm{A}$ to simulate electromagnetic disturbances from supply lines. After each trial, the turntable was rotated by 20° to eventually achieve a full circle. Whereas the hard iron source, as expected, had the strongest impact on the magnetic field when coming near to the sensor, all other distortion sources were clearly also superimposing the ambient magnetic field (see figure 7.8). Before testing the different Machine Learning (ML) techniques, a second-order Butterworth filter depending on the Nyquist frequency to filter out high-frequency noise was applied (7.9).

For evaluation, the turntable dataset was randomly split into a training set ($60\,\%$) and a test set ($40\,\%$). Afterward, a k-fold cross-validation grid search with 5 splits on the training set to prevent leakage of knowledge about the test set into the model during hyperparameter tuning was applied. The search grid for the hyperparameters had the following ranges: 1×10^{-3} to 1×10^{-7} for α, number of hidden layers between

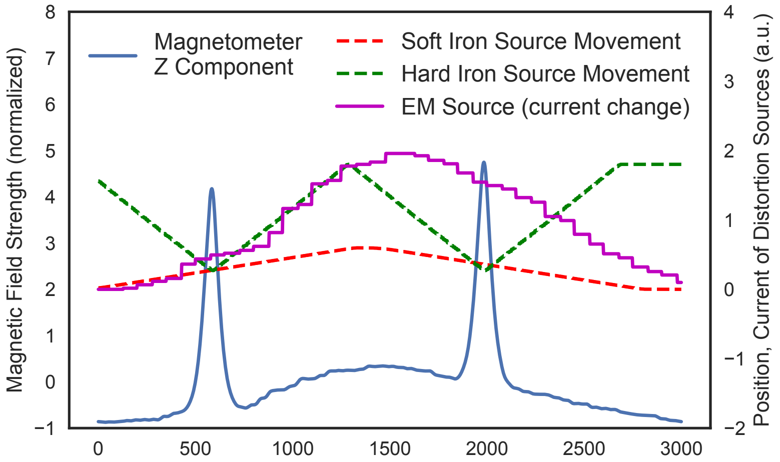

Figure 7.8: *Magnetometer z component plotted against the superimposing distortion source activities (turntable trials, heading* 80°*)*

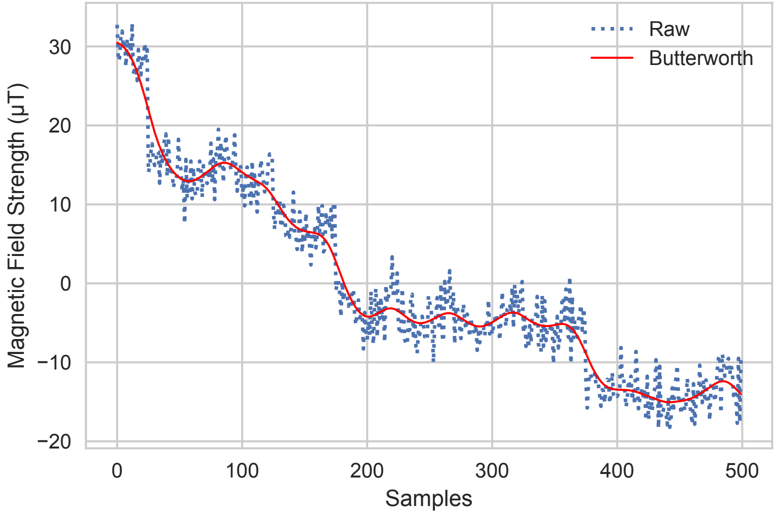

Figure 7.9: *Second order Butterworth filter applied to magnetometer raw readings of turntable data set*

1 to 3 with 5 to 100 perceptrons per layer, solvers *Adam* [Kingma and Ba, 2014] and *LBFGS* [Liu and Nocedal, 1989], and activation functions *logistic*, *ReLU*, and *tanh*.

Training the MLP regressor with 4 inputs (3 distortion sources plus heading) and 3 outputs, the best performance was achieved using 2 hidden layers of size 10 (first) and 20 (second), an α value of 1×10^{-4}, *relu* as activation function and *LBFGS* as a solver. The prediction and compensation quality on the turntable data set is shown in figure 7.10.

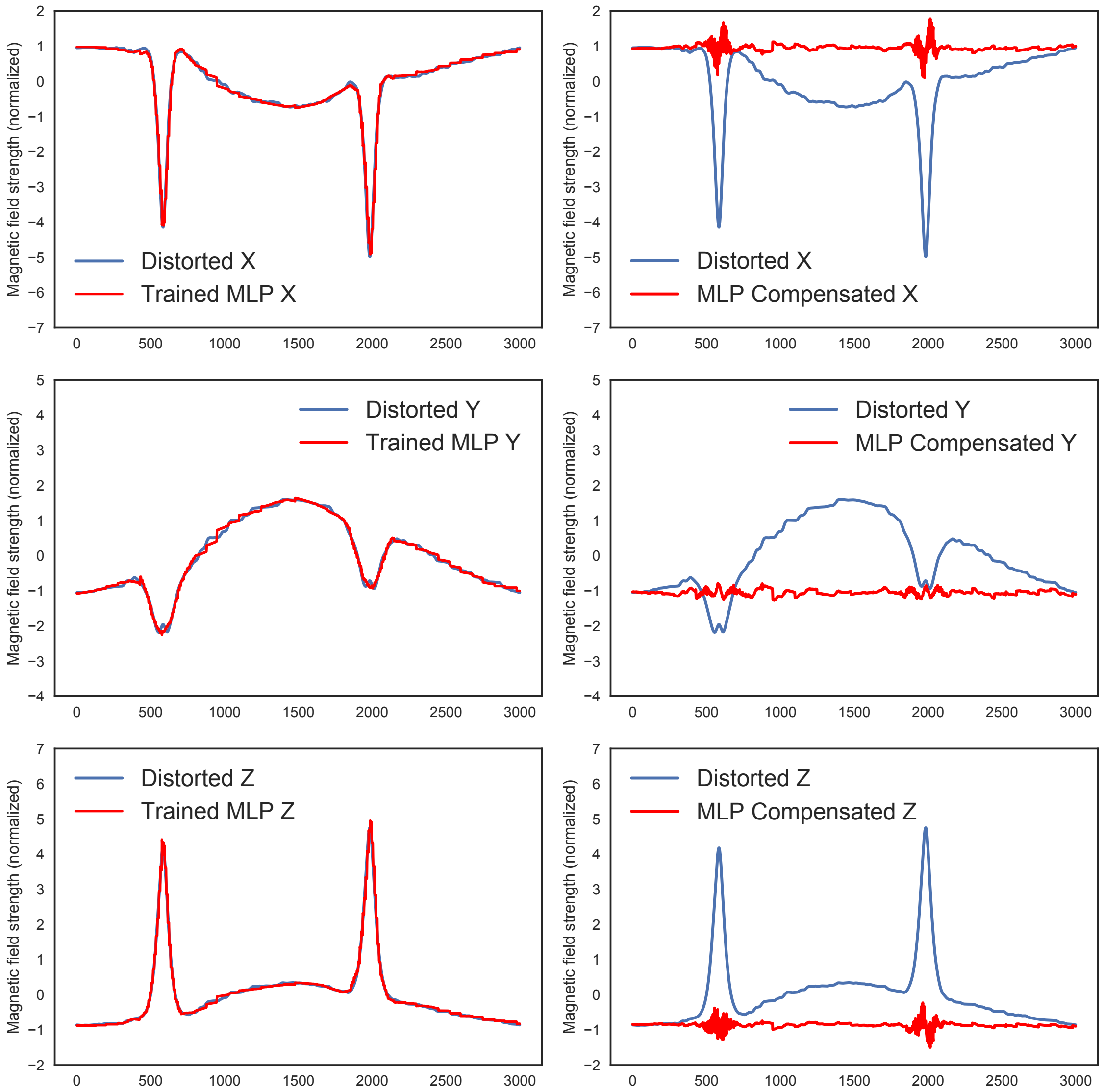

Figure 7.10: *Component-wise MLP prediction (left) and compensation (right) of magnetic field distortions (turntable trials, heading* 80°*)*

The MLP Regressor with the parameters presented above achieved an R^2-score [Anderson-Sprecher, 1994] of 0.986. Finally, using the MLP Regressor to predict the magnetic field distortions at the point of the magnetometer sensor given only the values of the activity for the various distortion sources, a significant reduction of the deviation due to dynamic distortions in the direction component was achieved, reflected in an increase in the κ concentration parameter from 0.86 to 618.2. See figure 7.10 for a component-wise comparison and figure 7.11 for a 3D directional scatter plot. However, randomly sampling from continuous measurements for the training set will, in general, give a preference of the model for accurate interpolating than for extrapolating (generalizing). Therefore it is best to include as many possible states of the robot as possible in the training data.

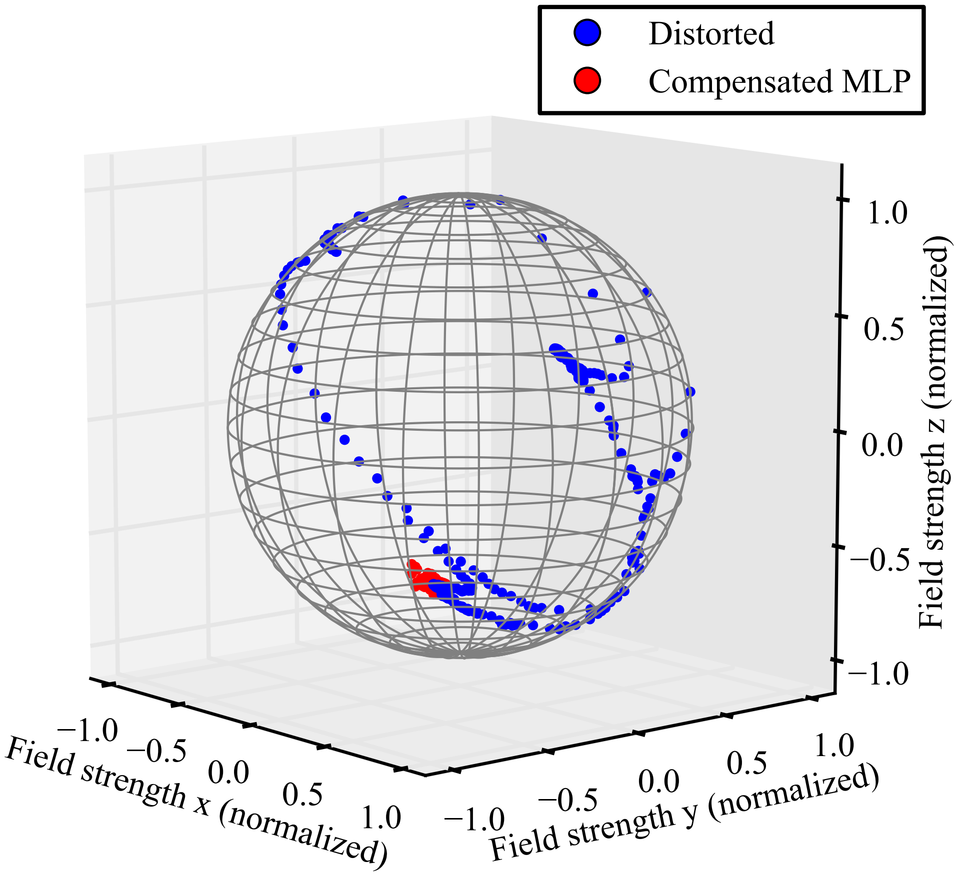

Figure 7.11: *3D scatter plot of dynamically distorted vs. MLP compensated directions (turntable trials, heading* $80°$*). Every dot represents the direction of a magnetic field direction measurement. Undistorted measurements would stay on the same spot on the sphere's surface.*

SherpaTT **dataset and evaluation**

Apart from the turntable experiment, the approach was also evaluated by a series of experiments with the complex hybrid wheeled legged robot *SherpaTT*, to analyze to what extent it is transferable to real robotic systems. The idea, as in the turntable setup, was to try to keep the orientation of the magnetometer stable in the ambient magnetic field and then activate as many measurable distortion sources as possible, both solitary and in combination, and record the induced vector field deviation from the sensor baseline. This was done by repeating a sequence of leg movements of the robot, first trying to cover most of the robot's DOF workspace, and second varying the single joint ranges while maintaining the central body pose. Furthermore, strong changes in the supply current were generated by defined movements of the robot. Since soft-iron types of distortion are depending on the orientation in the ambient magnetic field, the data set was recorded in 45° steps, covering a full 360° spot turn circle. Extra care was taken to prevent external disturbances during the data gathering.

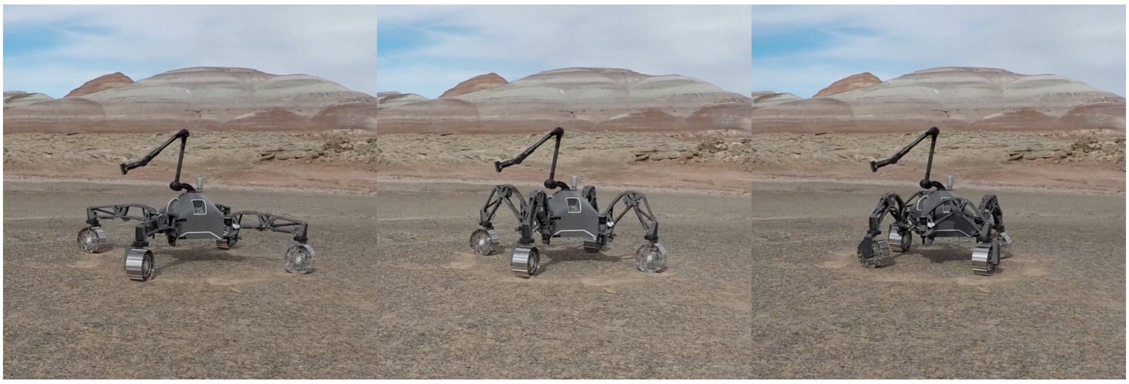

Figure 7.12: *SherpaTT during magnetic field distortion data set gathering in the desert of Utah, US*

Whereas there were few distinct and strong distortion sources in the turntable experiment (7.3), a multitude of permanent magnets moving around in each actuated robotic leg joint and the manipulator as well as multiple power supply lines in varying distance from the sensor and the robotic arm were influencing the magnetic field in the experimental setup using the robot *SherpaTT*.

Considering the absolute values, the observed deviations of the magnetic field measurements were orders of magnitude smaller than the deviations that occurred during the turntable experiment. This was expected since the magnetometer was positioned further away from possible distortion sources inside the robot's main body housing than in the turntable experimental setup, where the distortion sources were intentionally moved or placed very close to the sensor.

In addition to the MLP regressor, an SVR with two different kernels (linear and RBF) was trained for comparison using this more complex dataset. The MLP had an input layer of size 25 (5 joint positions and one supply line per leg plus heading) and again 3 outputs representing the deflected magnetic field offset vector. To obtain the best parameters for the SVR and MLP, a grid search was again applied, over the same ranges as in the turntable experiment for MLP and from 0.1 to 25 for the SVR penalty parameter C and 0.01 to 0.8 for the SVR epsilon tube.

The SVR γ parameter was determined with

$$\gamma = \frac{1}{n * VAR(X)} \tag{7.4}$$

with n the number of features and $VAR(X)$ the variance in the input data.

As with the turntable data set, the *SherpaTT* deviation dataset was randomly split into a training set using $60\,\%$ and a test set of $40\,\%$. A k-fold with 5 splits on the training set was applied for hyperparameter tuning. The best performance was achieved using the following hyperparameters: 3 hidden layers with 100, 50 and 25 units respectively, an α value of 1×10^{-4}, *tanh* as activation function and again *LBFGS* as a solver (which is common for small training datasets) for MLP and $C = 1.5$ for SVR with an RBF kernel.

The resulting predictions on the test data are shown in figure 7.13 for the SVR and in figure 7.14 for the MLP.

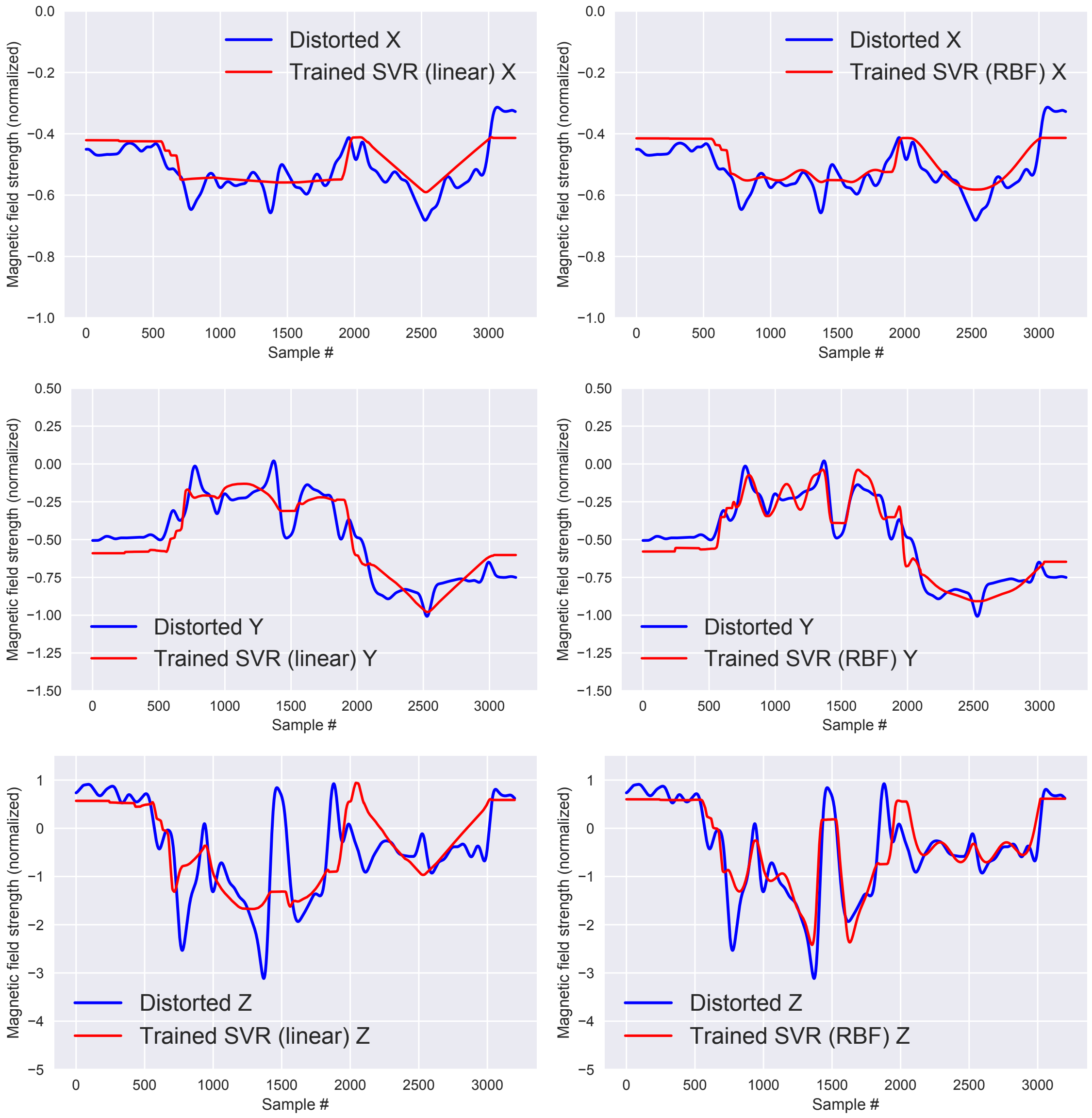

Figure 7.13: *Component-wise SVR prediction of magnetic field distortions with linear (left) and RBF (right) kernel (SherpaTT trials, heading* 180°*)*

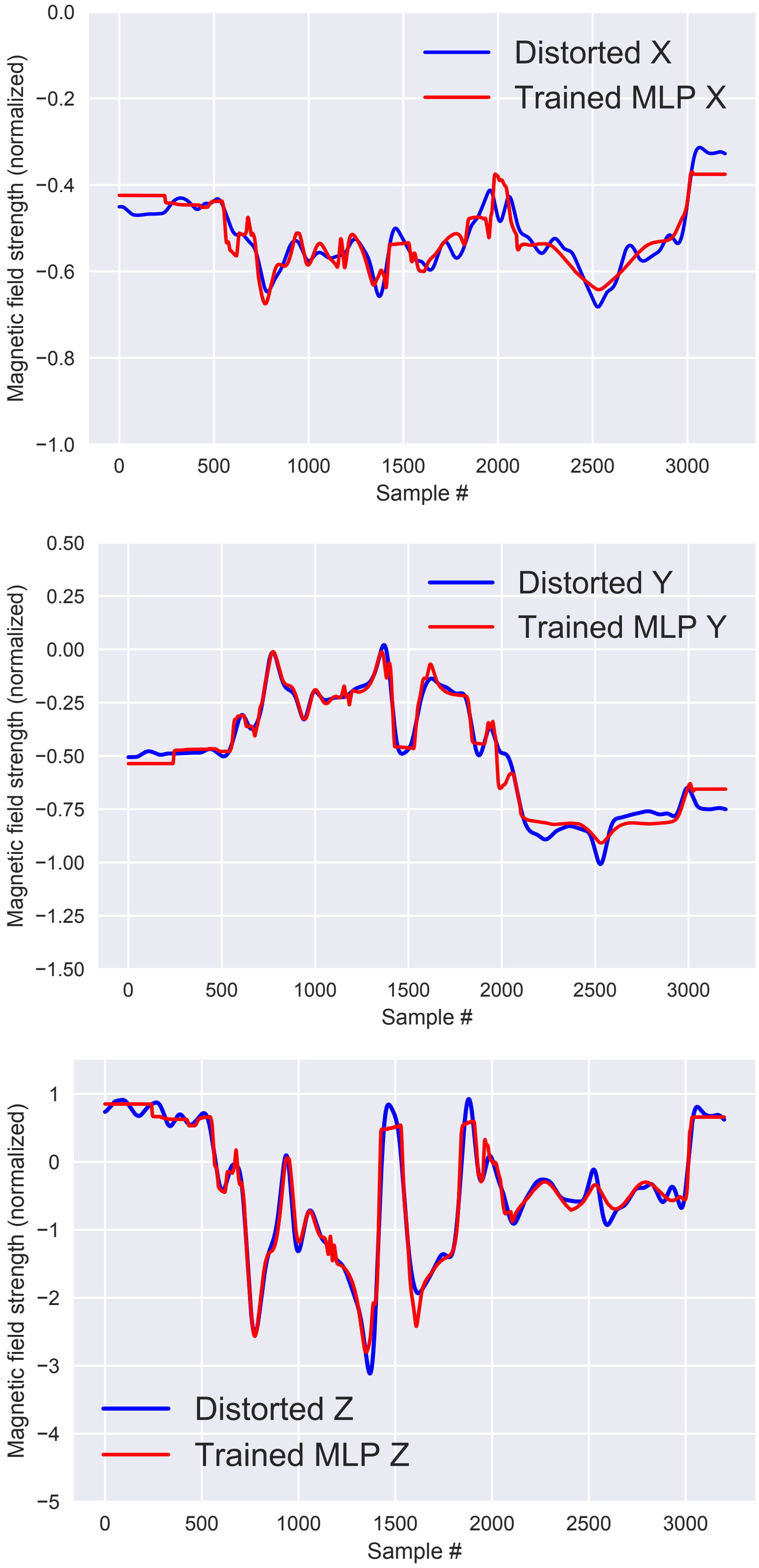

Figure 7.14: *Component-wise MLP prediction of magnetic field distortions (SherpaTT trials, heading* 180°*)*

The multi-target MLP model with its optimized meta parameters was able to achieve a significantly better fit on the test data set with R^2 training scores of 0.96 compared to the single component SVR models with 0.60, 0.84, 0.46 (X, Y, Z linear kernel) and 0.63, 0.91, 0.80 (X, Y, Z RBF kernel). This is also reflected in the compensation quality of the directional component of the magnetic field: the SVR based compensation (figure 7.15) was not able to stabilize the direction to the same extent as the MLP based compensation (figure 7.16), with the respective compensation parameters $\kappa = 8.21$ for SVR with linear kernel, $\kappa = 15.91$ for SVR with RBF kernel and $\kappa = 114.50$ for MLP compared to the distorted directions with concentration parameter $\kappa = 3.64$.

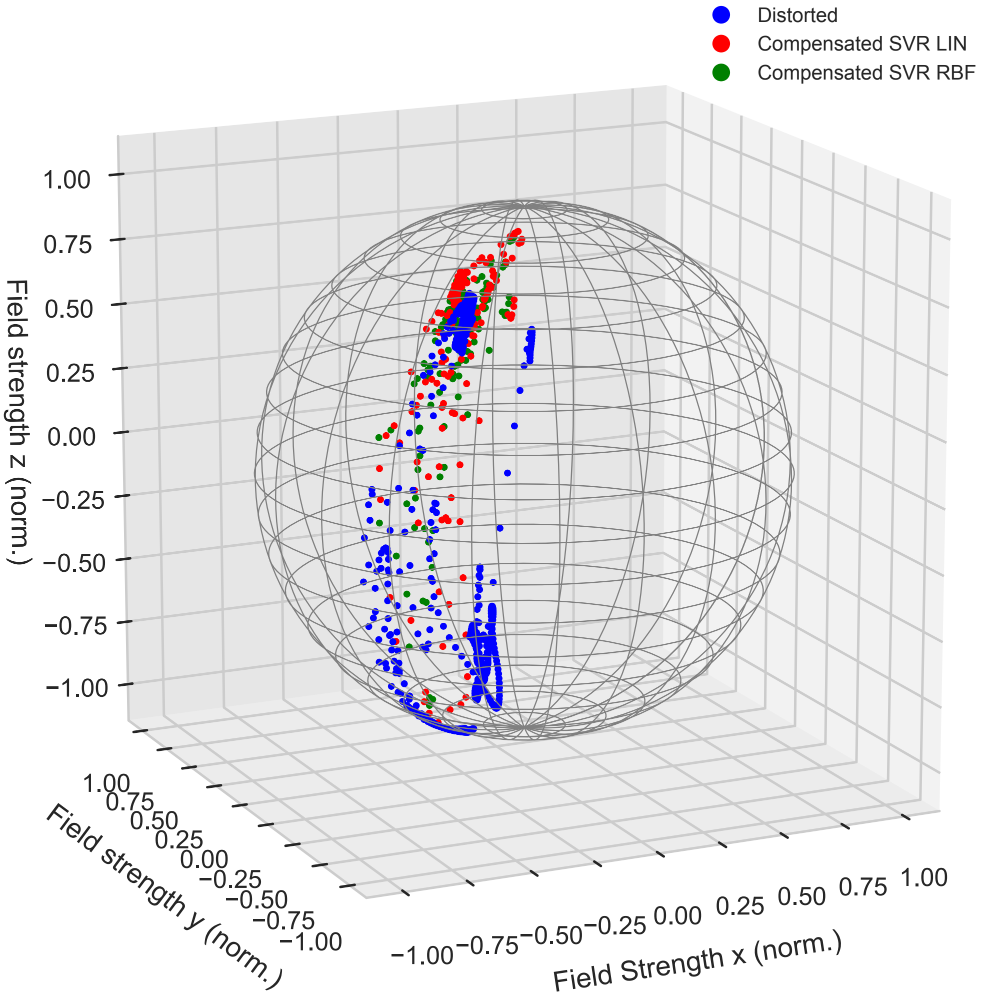

Figure 7.15: *3D scatter plot of dynamically distorted and SVR compensated directions (SherpaTT trials, heading* 180°*)*

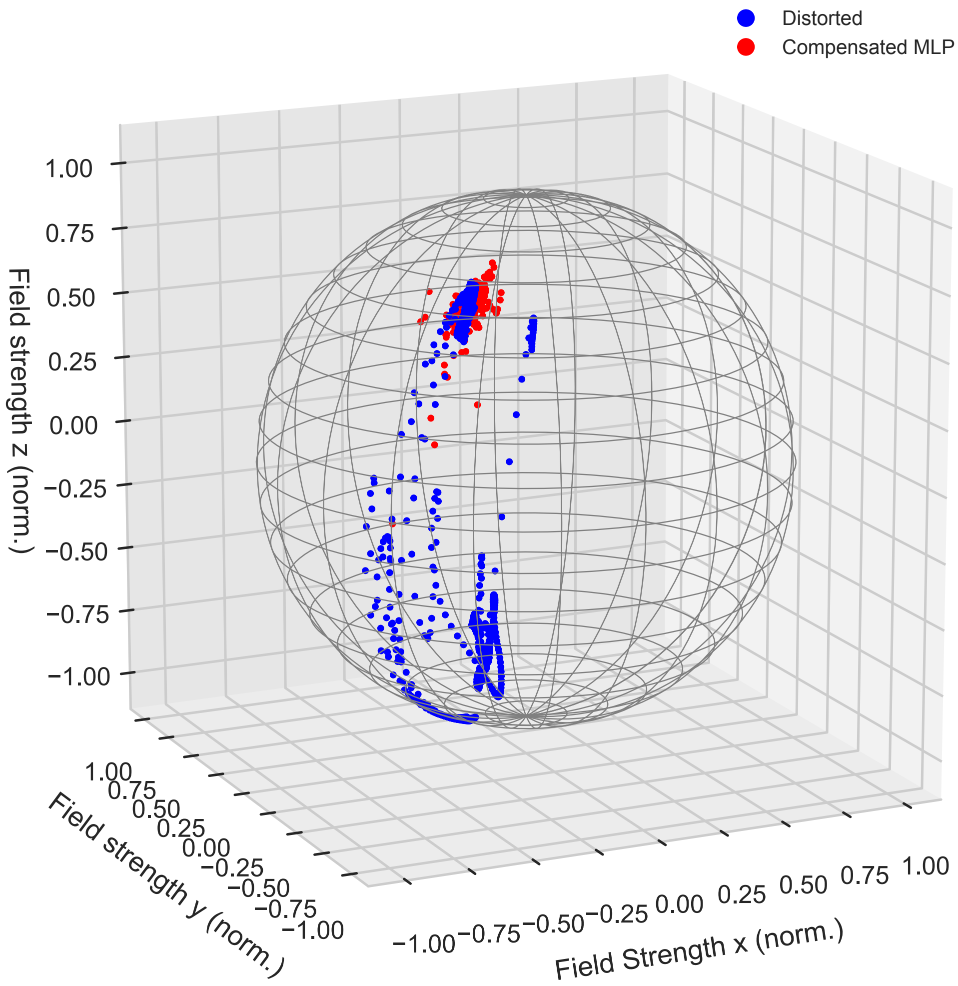

Figure 7.16: *3D scatter plot of dynamically distorted and MLP compensated directions (SherpaTT trials, heading* 180°*)*

7.4 Conclusion

This chapter presented and discussed several machine learning approaches to model magnetic field distortions often induced in inertial measurement units using magnetometers by changing currents, postures or configurations of a robotic system as shown in Chapter 5. Such models are needed in order to compensate the local dynamic distortions, especially for complex and confined robotic systems, and to achieve more robust and accurate ambient magnetic field measurements.

The evaluation showed, that MLP regressors with LBFGS solvers are especially capable of predicting the magnetometer deviations, and results of direction compensation based on such an approach were shown not only in a laboratory setup, but also for a complex real robot like *SherpaTT*. The results indicate, that for modeling the magnetic field, simple interpolation approaches like SVR with linear kernels and even with RBF kernels are insufficient and more complex functions like those represented by a 3-layer MLP are required.

Chapter 8

Localization in Magnetic Fields

After having shown that significant features of the ambient magnetic field are available in a lot of robotic application environments (Chapter 4), Chapter 6 and Chapter 7 then introduced approaches to compensate for magnetic field distortions caused by activity and structure of the robots themselves. Such proper calibration and dynamic compensation provided, this chapter discusses the actual exploitation of magnetic field distortions for localization purposes.

8.1 Visual-Magnetic Close Range Navigation

Multiple tasks require a very precise close-range vehicle localization when approaching structures or other vehicles, for example during handing over probes in sample-and-return missions with a team of cooperative robots [Sonsalla et al., 2014, Sonsalla et al., 2017]. Typical examples in maritime applications are docking with a submerged asset infrastructure or with another vehicle, maintenance or georeferencing.

While a number of different sensors have been used for this purpose in the past, the approach developed in this work features a bimodal system fusing magnetic data of 3-axis-magnetometers and visual camera data, first published in [Hildebrandt and Christensen, 2017]. The deployment of fundamentally different modalities for data acquisition is intended to significantly increase the fault-tolerance, since the disturbance of one source of information is unlikely to affect the other. For example, poor visual conditions might hinder only the camera, while *non-modeled dynamic external* magnetic fields like moving metallic structures might just interfere with the magnetic sensors.

There are a number of different docking systems for AUVs, which can be roughly categorized by the vehicle's approach strategy: AUVs which rely on forward-motion for depth-keeping (dynamic diving AUVs) usually feature a rather large passive guidance funnel, which serves both as guidance mechanism and breaking system [Hobson et al., 2007]. Docking stations for hovering-enabled AUVs have a higher degree of diversity, ranging from garage-type stations [Albiez et al., 2015] [Brighenti et al., 1998], stations resembling a cradle [Wirtz et al., 2012] to miniature docking stations [Hildebrandt et al., 2013]. Typical approach strategies include acoustic homing [Eustice et al., 2007] and visual approaches [Kim, 2007] [Murarka et al., 2009]. Due to the high positioning accuracy of vision-based sensors, they usually are the preferred method for the final docking approach. Magnetometers on AUVs up to now have mostly been used as strap-down compasses (see discussion in Chapter 1).

8.2 Visual-Magnetic Docking

The developed close-range navigation system for subsea docking consists of sensors mounted on the robotic vehicle as well as markers attached to the docking station. The sensors on the robotic vehicle are a monocular camera and a multi-magnetometer array as described in 6, this time with the amount of four 3-axis magnetometers. The docking station is equipped with a visual marker as well as a strong NdFeB magnet, to resemble the expected larger steel structures in a real scenario for the scaled-down laboratory setup. The basic idea of the approach is to track the visual marker with the monocular camera as well as to detect the magnetic field of the rare-earth magnet using the magnetometers. The basic setup is depicted in figure 8.2. The position estimates of both sensor modalities are fused, resulting in a single estimate of relative position which can be used for navigation, although both methods can also provide an independent estimate of the position.

Extracting relative position data with a camera-marker setup is relatively simple and has been used numerously for similar purposes (for an overview see for example [dos Santos Cesar et al., 2015]). Given the utilization of robust markers such as April-Tags [Olson, 2011], Aruco-Markers [Garrido-Jurado et al., 2014] or similarly encoded 2-d visual markers, a calibrated monocular camera can extract the marker's 3d position and orientation if the size of the marker is known. The limiting factors of this approach are usually image and processing rate on the one hand and precision with respect to the field of view, distance and resolution of the camera on the other hand. Typical cameras run with approximately 30 Hz, which is suffi-

Figure 8.1: *Experimental setup with multi-magnetometer (version 1) attached to the pressure housing of a subsea camera*

cient for most navigation purposes. Processing complexity is directly proportional to the camera's resolution, but it has been shown that even with moderate processing hardware and typical cameras, processing rates of 30 Hz are well achievable [dos Santos Cesar et al., 2015]. Precision is more complex, as it depends on three factors: the camera's field of view, resolution of the camera and distance or size of the marker. For the case of close-range navigation of interest in our application, sub-centimeter accuracy can be achieved.

While marker-tracking and other vision-based approaches tend to have high accuracy in position estimation in proper visibility conditions, they lack robustness and are prone to errors in demanding environments, especially in turbid waters (e.g. river deltas, harbor basins, subsea production/mining fields, etc.). Another sensor modality often used on AUVs are therefore acoustic approaches to complement the optical methods. But acoustic systems usually don't have the accuracy of the optical systems and also have to struggle with changing sound propagation characteristics due to varying salinity, conductivity and temperature in the water column.

Opposed to that, the earth magnetic field is not disturbed by these effects. As discussed in Section 2.1, the pole's location is changing over time and the magnetic field is locally distorted depending on latitude and longitude of the observer, but the declination from magnetic to true north can be computed using analytical models like the WMM [Chulliat et al., 2015]. Apart from this variation coming from the main magnetic field density contributors (the earth core with its geodynamo effect

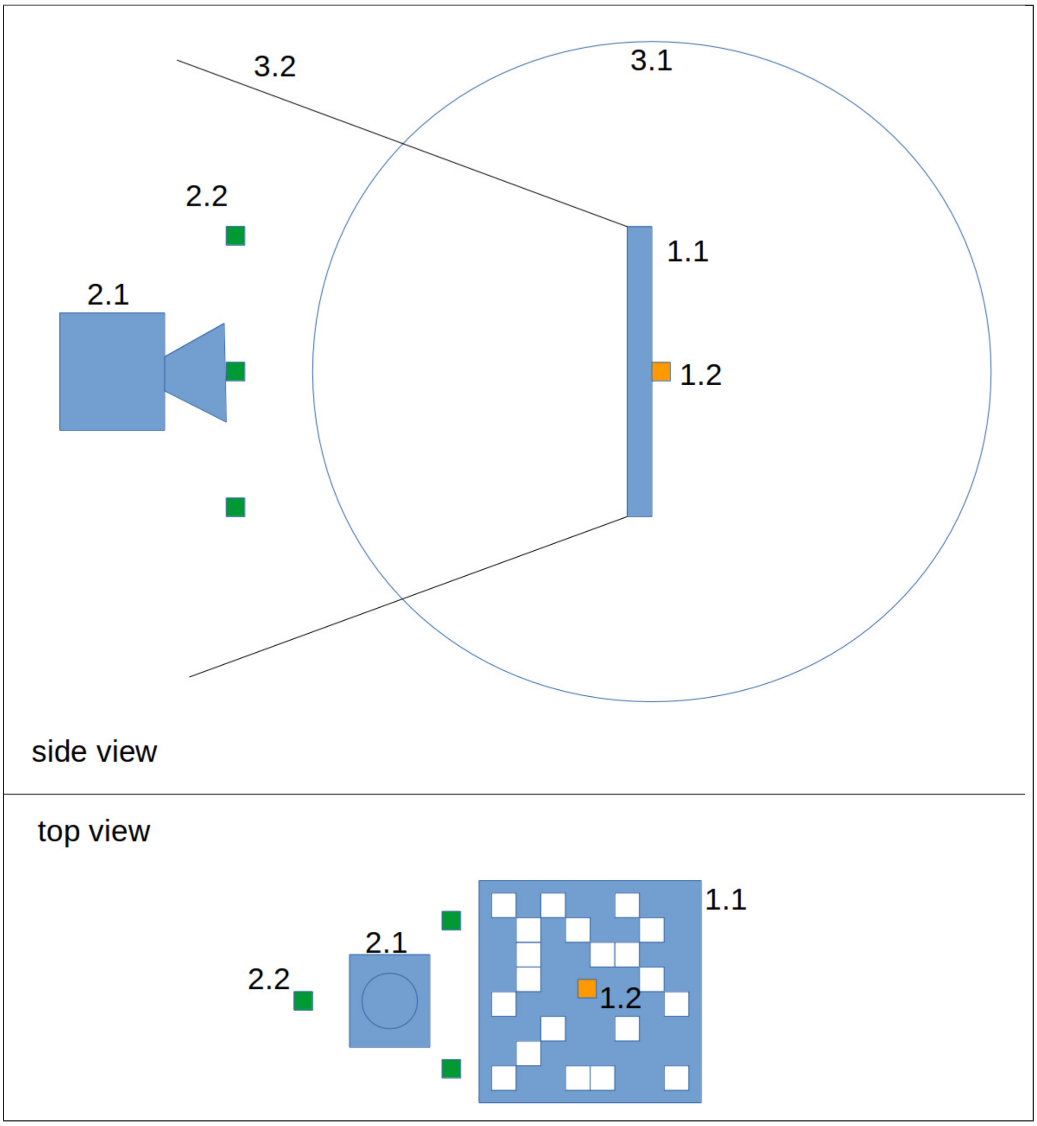

Figure 8.2: *Basic setup of the navigation system: base station (1), 1.1: visual marker, 1.2: rare-earth magnet; sensors on robotic vehicle (2), 2.1: monocular camera, 2.2: 3-axis magnetometers; working-areas of sensors (3), 3.1: magnet detection radius, 3.2: visual marker detection area.*

and the earth crust), the earth magnetic field can be considered sufficiently stable in the temporal domain for the purpose of close-range navigation (see Section 2.3 and [Christensen et al., 2017]). System-induced local magnetic field distortions may occur due to the magnetic remanence of the vehicle's material or strong electrical currents, but Section 6 and Section 7 of this thesis presented calibration and compensation approaches to counter both static and dynamic vehicle-immanent distortions (see also [Christensen et al., 2015, Christensen et al., 2017, Renaudin et al., 2010]).

The remaining distortions of the ambient magnetic field caused by the docking structure carry the information, that is utilized in the proposed method of relative vehicle position estimation here. The proposed method again utilizes machine learning techniques, exploiting the fact that with the cameras, there is at least a temporarily available modality for direct measurements of the relative vehicle position to the docking structure. This enables the dataset collection of magnetometer data in the navigation workspace while in parallel recording position data from the cameras if the turbidity in the water column allows doing so. This dataset is used to train an Support Vector Machine (SVM) for function regression (SVR) or an Artificial Neural Network (ANN), in this case a multilayer perceptron regressor network (MLP, for details see Section 7). After function regression, the trained SVR or MLP regressor is used in realtime to estimate the position of the docking structure relative to the magnetometers.

Limiting factors for this modality apart from proper a priori calibration are the distance between the ferromagnetic structure and the magnetometers, the strength of the rare-earth magnet in the laboratory setup and the dynamic range of the magnetometers. Since all three are dependent, it is important to select the strength of the magnet and the dynamic range of the magnetometers according to the size of the work-space in order to achieve maximum precision. In addition, workspace coverage and marker tracking accuracy will have a huge effect on the usability of the training data, as shown in the following.

8.3 Experiments

All experiments were performed with the following sensor setup: an Allied Vision Prosilica GC 1380h digital camera with a 1280×1024 resolution using an $87°$ optical lens in a waterproof pressure housing and four ST LSM303D 3-axis magnetometers in a circular arrangement around the camera lens, using the proposed multi-magnetometer setup described in Section 6.1. The base station consisted of a $10 \times 10\,\mathrm{cm}$ Aruco-type marker and a neodymium magnet cube with 1 cm edges and high magnetic remanence of $1.45\,\mathrm{T}$ and an approximated maximum energy product of $400\,\mathrm{kJ\,m^{-3}}$ (grade *N52*). The experiment system setup in one of the test basins at DFKI RIC is shown in figure 8.3. Figure 8.4 depicts the computer vision extraction of the used Aruco-type markers during data aquisition.

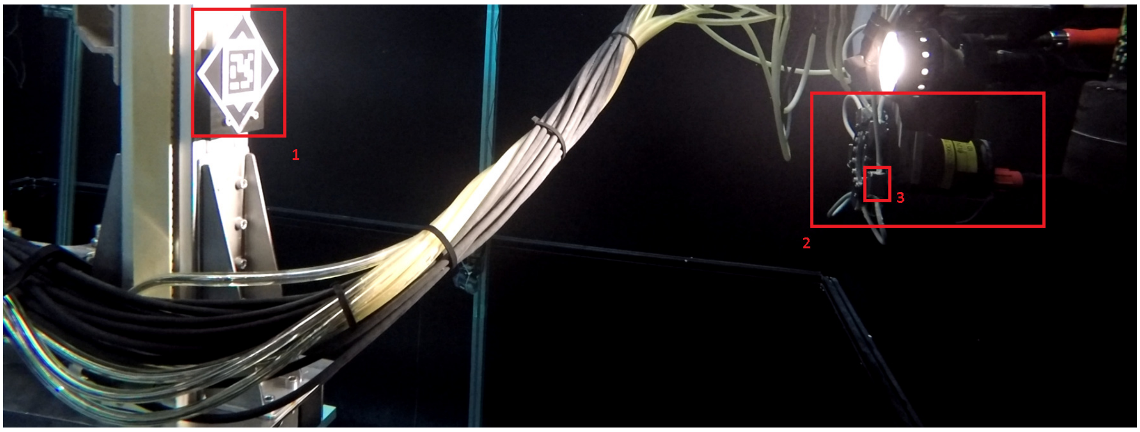

Figure 8.3: *Setup of the test-system consisting of the docking-station mounted on the z-axis of the gantry crane (1), the camera (2) and magnetometer sensors (3) as proposed in Section 6.1*

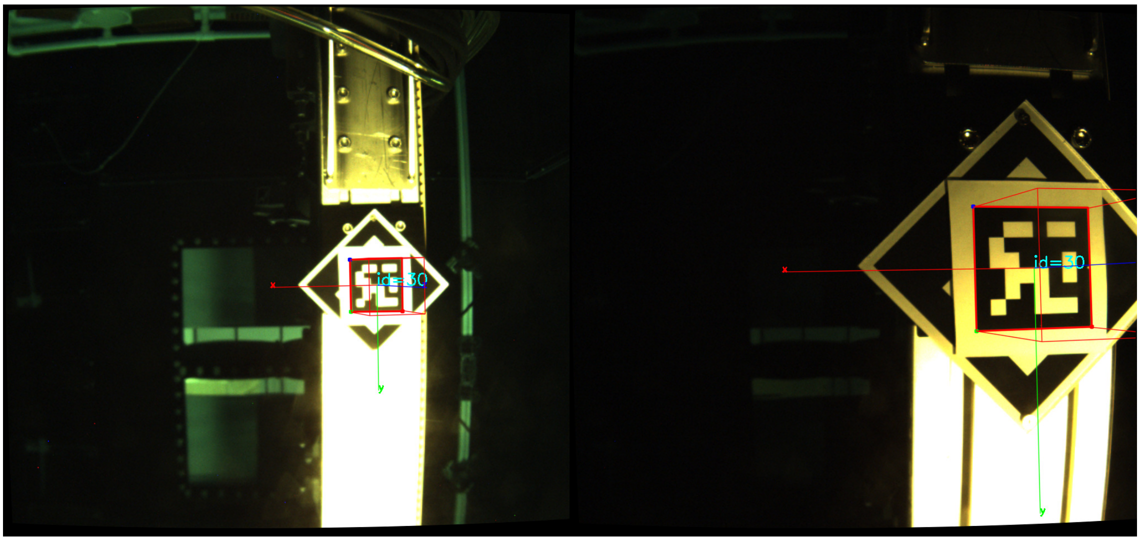

Figure 8.4: *Camera images of the marker and its extracted position during the test trajectory*

Positioning Accuracy of Camera/Marker Tracking with Gantry Crane

In order to estimate the accuracy of the camera-based marker tracking, an experiment was conducted, where the base station was fixed and the test-setup moved externally by a 3-axis gantry crane. The resulting dataset is used to characterize the optical tracking system (following the principles described in [Hildebrandt et al., 2014]), since the marker tracking is used later to gather training data for the magnetometer-based localization. The gantry crane has a positioning accuracy of $< 0.2mm$ [Christensen et al., 2009], its position is considered as the ground-truth with minimal uncertainty for the purpose of the data set generation. The workspace for the camera test setup of $0.4 \times 0.4 \times 0.2\,\mathrm{m}$ was discretized into a $5\,\mathrm{cm}$ grid, a camera image was taken at every of the resulting 256 cell positions with a corresponding automated trajectory of the gantry crane (see figure 8.5).

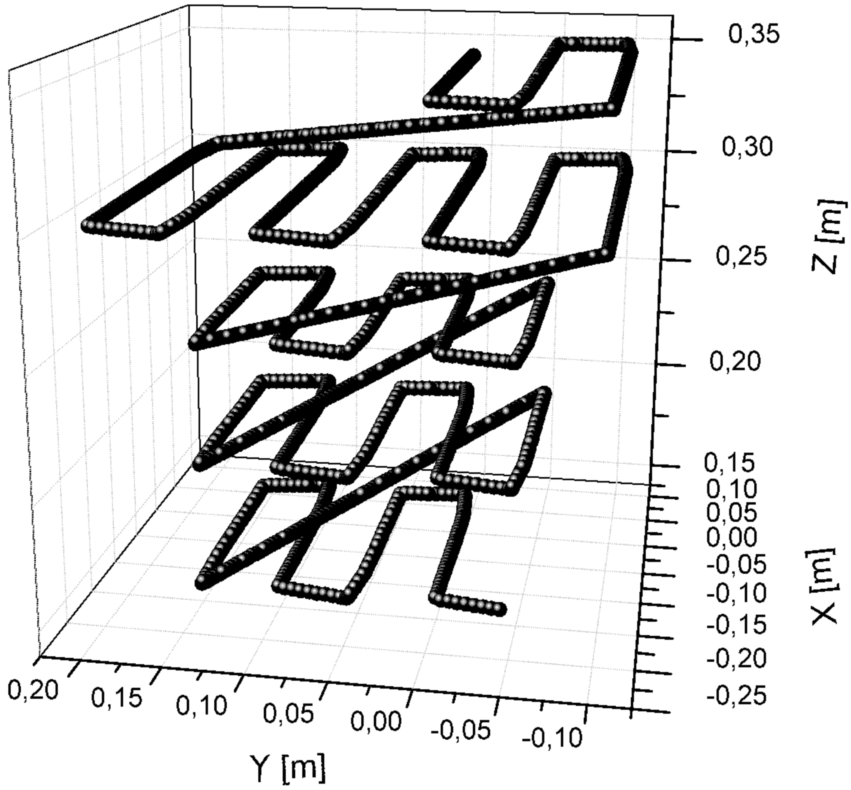

Figure 8.5: *Trajectory of the gantry crane to sample the navigation workspace*

While the marker tracking accuracy for the x- and y-axis remains stable apart from marker tracking drop-outs at the edges of the camera image (figure 8.6), the tracking accuracy standard deviation for the z-axis improves with reduced distance, ranging from a standard deviation of $1.23\,\mathrm{cm}$ at a distance of $0.35\,\mathrm{m}$ to a standard deviation of $0.54\,\mathrm{cm}$ at a distance of $0.15\,\mathrm{m}$ (figure 8.7). This is in accordance with the expected tendency, since the effective resolution for size estimation of the marker improves at close distances.

The docking adapter was designed for an accuracy of $> 1cm$, and the results presented in Section 8.3 meet that requirement. The fact, that z-axis accuracy improves

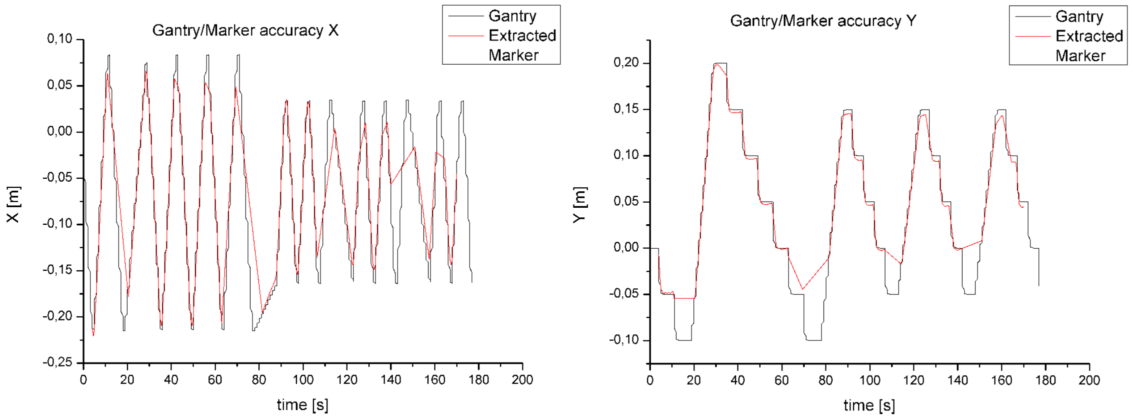

(a) *Gantry-X vs Marker-X* **(b)** *Gantry-Y vs Marker-Y*

Figure 8.6: *The Graph shows the position of the gantry crane in x and y direction and the extracted marker positions. Note the drop-outs at the edges of the image.*

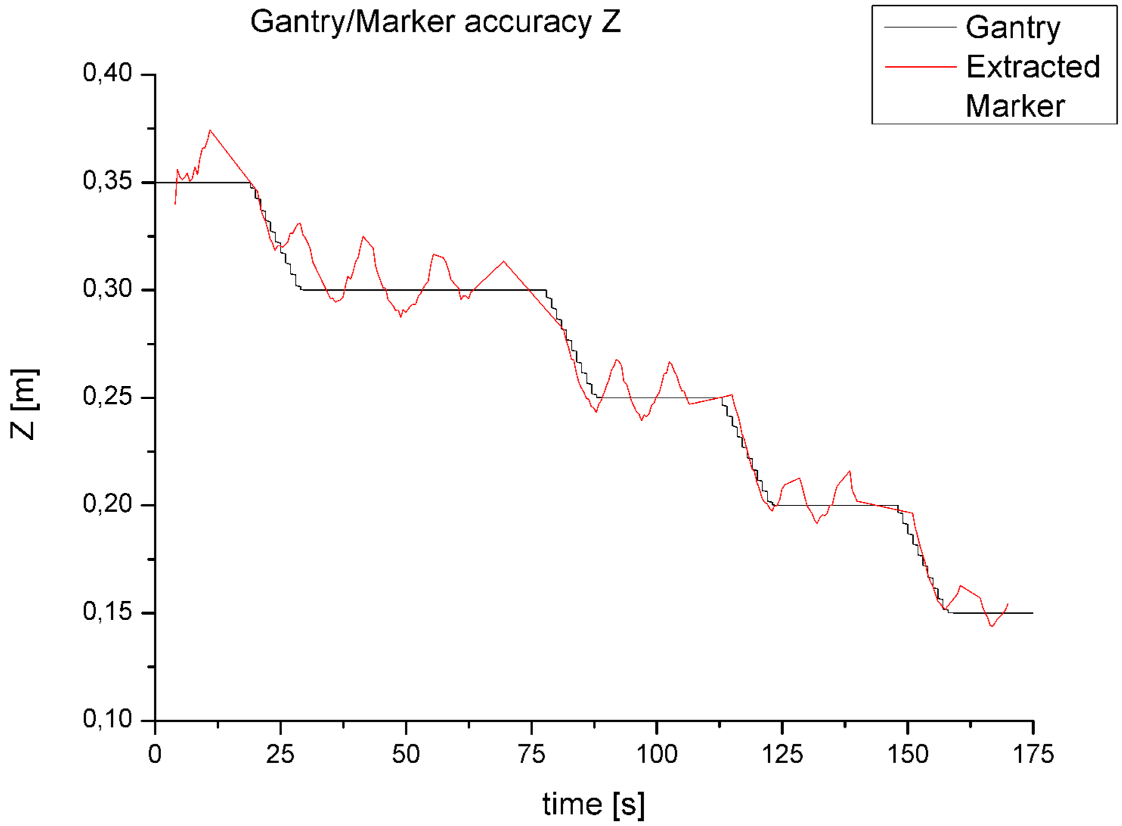

Figure 8.7: *Results of the camera / marker tracking experiment. The graph shows the gantry crane z-axis position relative to the camera over time as well as the extracted marker position.*

when the marker was closer to the camera fits a docking scenario in the sense, that higher precision is needed when the vehicle closes in towards the docking station.

Machine Learning Positions from Magnetic Field Data

The data set to evaluate the ML-based magnetic field localization approach, was gathered with the same setup as described above, and consists of 442 samples with $4 \times 3 = 12$ magnetometer readings and 3 position components from the camera-based marker detection each. The magnetometers where sampling at $100\,\mathrm{Hz}$ and the estimation frequency of the camera-based marker tracker was $0.72\,\mathrm{Hz}$. All magnetometer readings except those occurring when a marker pose was estimated where discarded. In order to filter out high-frequency noise, a second-order Butterworth filter depending on the sampling Nyquist frequency was applied (figure 8.8).

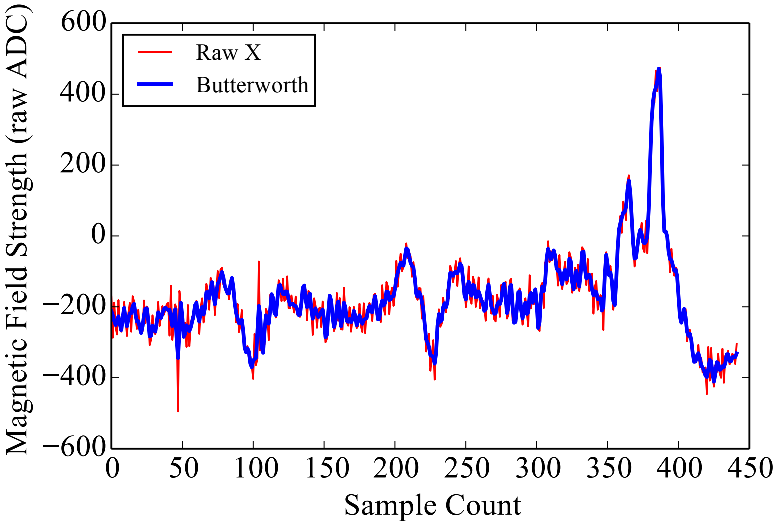

Figure 8.8: *Second order Butterworth filter applied to magnetometer raw measurements*

The lowpass-filtered magnetometer values, the input for the models to be trained, were standardized to have zero mean and unit variance. In order to prevent overfitting, the data was split using random permutation into a training data set of 60% and a test data set of 40%. Before training the SVR and MLPR, grid search was applied, using the training data set to find the optimal meta parameters. The grid search resulted in a C-value of 1.0 and an ϵ-value of 0.1 for the SVR (see Section 7 for an explanation of the hyperparameters). With the SVR approach being single-target, one support vector machine for each of the three dimensions of the target position had to be trained (figure 8.9).

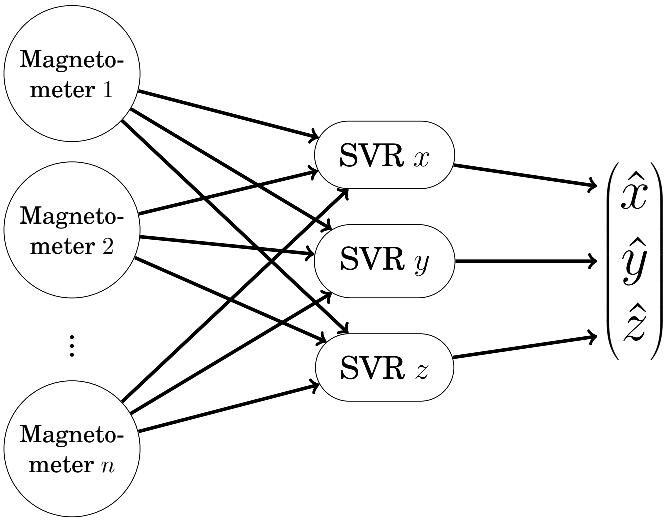

Figure 8.9: *Single target function regression approach with n magnetometer sensor readings as input and single position component output*

For comparison, also a linear kernel was applied with the SVR aside from the more capable radial basis function (RBF) kernel. Initial parameters for the MLPR after an exhaustive grid search over the hyperparameters space were an α-value of 0.01 and 3 hidden layers of size 40, 30 and 20 neurons. The grid search also favored *LBFGS* over *Adam* as a solver and the rectified linear unit function over the logistic sigmoid and hyperbolic tan functions for activation. For a detailed description of these hyperparameters, see [Vapnik, 2000, Smola and Schölkopf, 2004, Chang and Lin, 2011, Hinton, 1989, Glorot and Bengio, 2010].

After training with these meta parameters, the single component SVR models achieved a R^2-score [Anderson-Sprecher, 1994] of 0.33, 0.73, 0.93 (X, Y, Z linear kernel) and 0.65, 0.97, 0.97 (X, Y, Z RBF kernel), reflected in the fitting curves depicted in figure 8.10. As expected, in the case of the support vector regressor, the linear kernel is not able to fit the data to the extent of the RBF kernel, due to the inherent non-linearity of the magnetic field measurements.

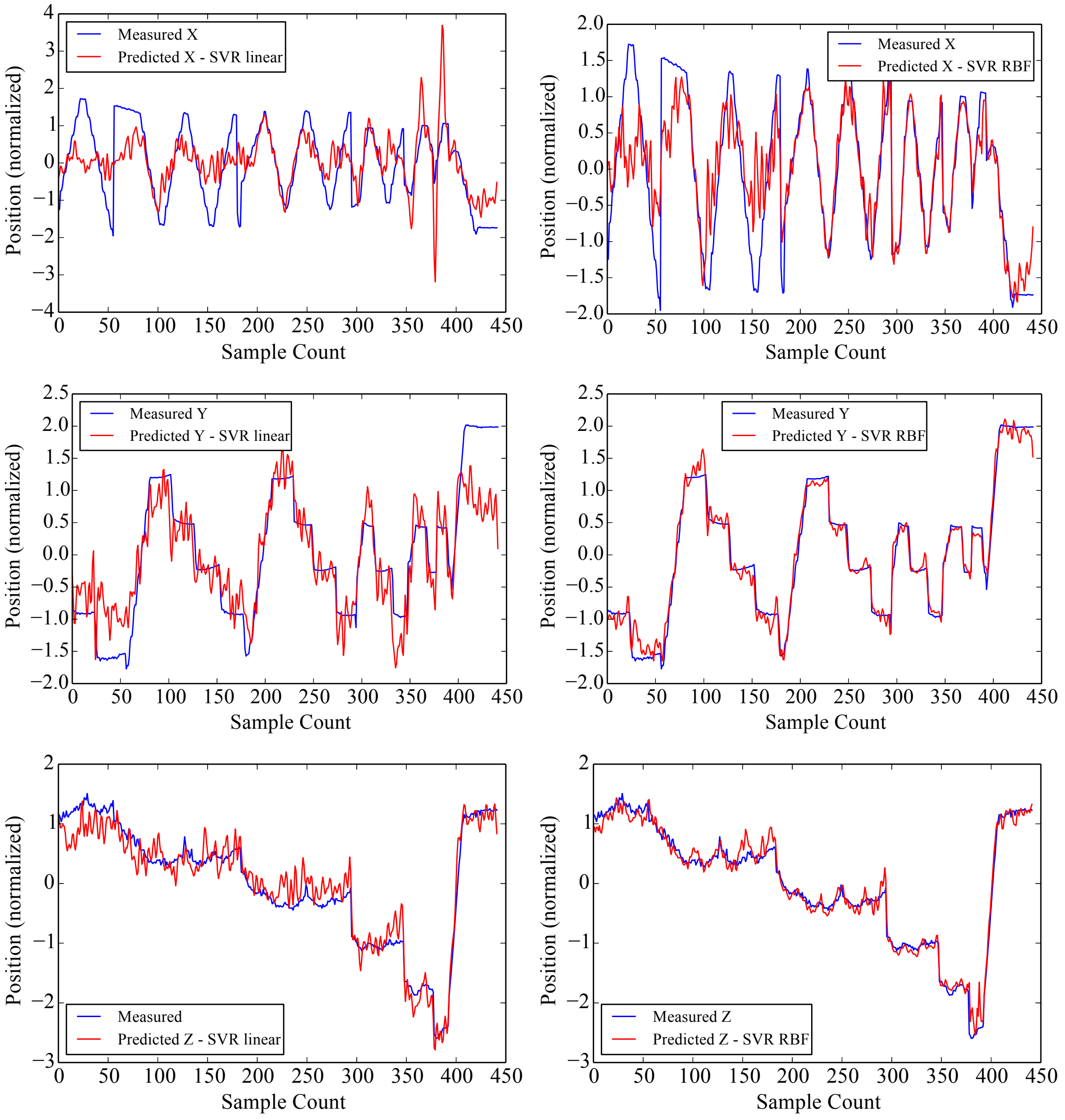

Figure 8.10: *Component-wise Support Vector Regression on evaluation part of the data set with linear kernel (left) and RBF kernel (right)*

Better than the trained SVR with RBF kernel was the performance of the artificial neural network in form of an MLP, which is capable of multi-target learning, thus training all three position dimensions in one go (8.11). The MLP Regressor with the parameters presented above achieved an overall R^2-score of 0.97, which is reflected in the predicted values closely following the measured values in the test set depicted in figure 8.12 and figure 8.13.

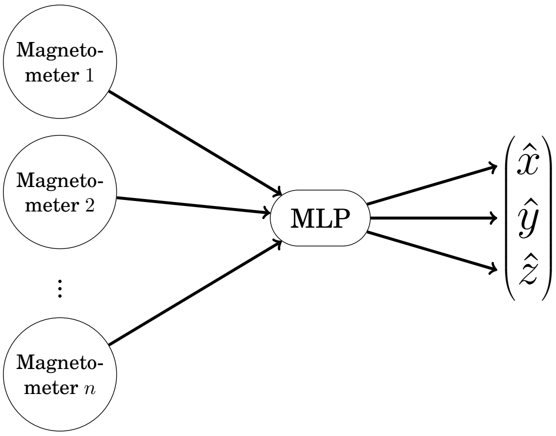

Figure 8.11: *Multi target function regression approach with n magnetometer sensor readings as input and combined position output*

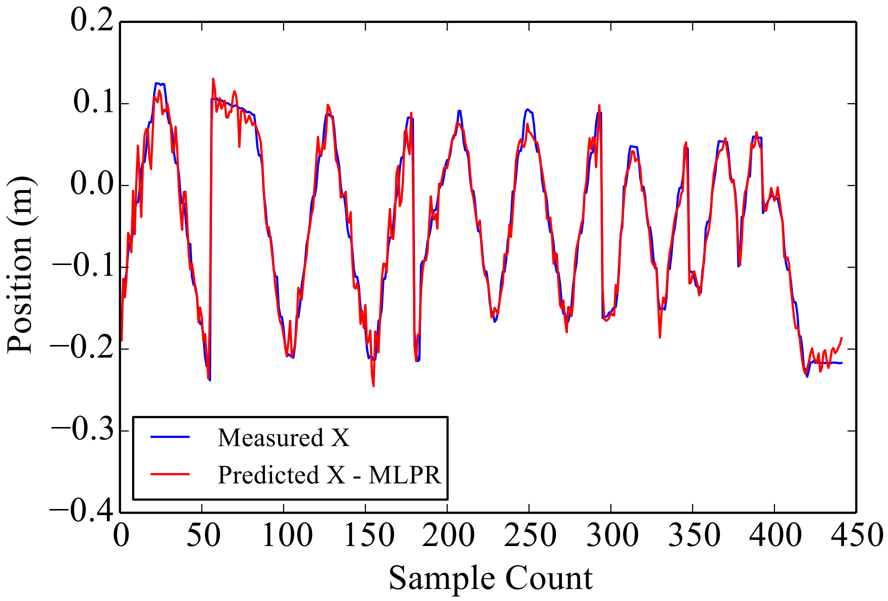

Figure 8.12: *Prediction of the x component on the evaluation part of the data set using multi-target MLP regression, LBFGS solver*

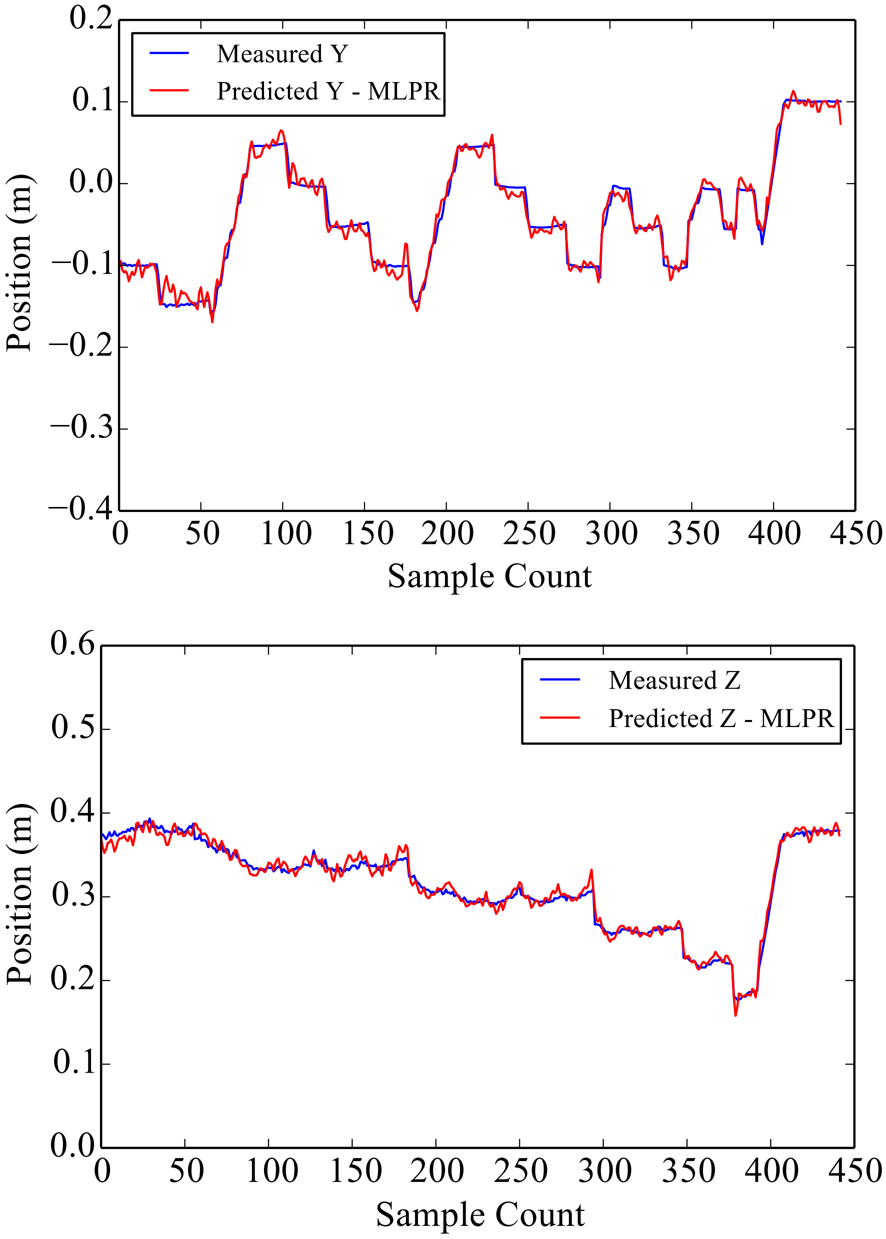

Figure 8.13: *Prediction of the y and z component on the evaluation part of the data set using multi-target MLP regression, LBFGS solver*

To further evaluate these trained models and check for overfitting, a completely different path than the training and evaluation data sets presented above was driven: a straight through the navigation workspace was executed, while trying to predict the position just using the magnetometer readings from the ambient magnetic field. As shown in figure 8.14 and figure 8.15, both the trained SVR RBF and the MLPR were able to estimate the position given just the magnetometer readings. Although the MLPR had a better R^2-score during fitting, it seems that the SVR RBF has better capabilities to generalize or interpolate at regions with no training data, as it shows smaller errors at the beginning of the trajectory. As expected, both SVR and MLPR predictions are getting significantly better, the closer the distance between the magnet and magnetometer gets.

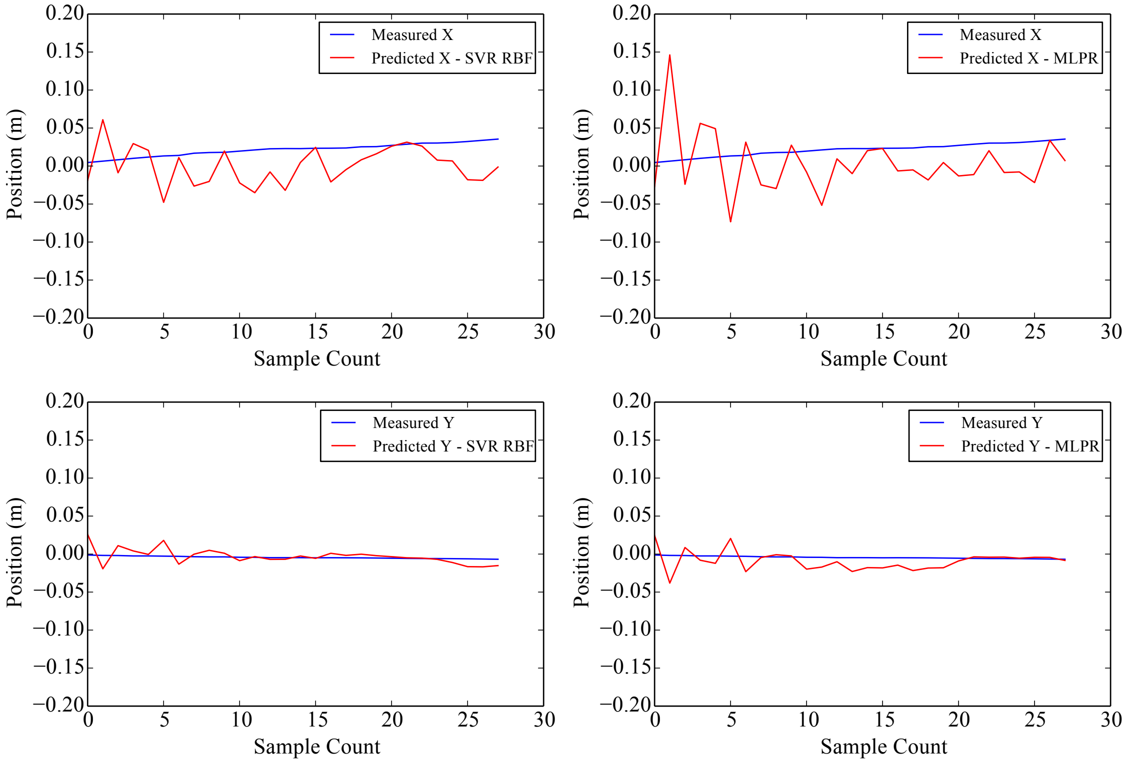

Figure 8.14: *Position prediction for the x and y component from magnetic field measurements during straight evaluation run, based on trained SVR-RBF (left) and MLPR (right) models*

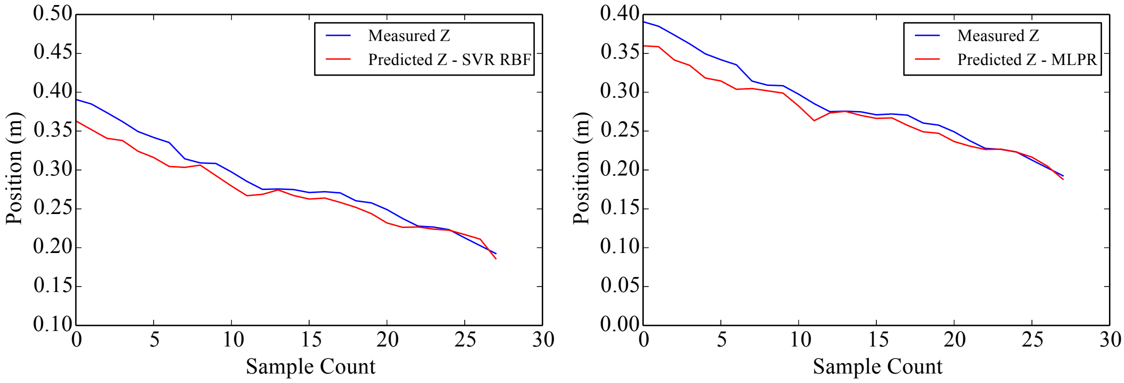

Figure 8.15: *Position prediction of the z component from magnetic field measurements during straight evaluation run, based on trained SVR-RBF (left) and MLPR (right) models*

AUV Docking Scenario

After the laboratory evaluation, the visual-magnetic approach for docking was transferred to the AUV Leng to further verify the feasibility of the approach. After a preliminary setup with the first version of the multi-magnetometer attached to the front of the AUV, a new front body part with directly integrated magnetometers was manufactured (see figure 8.16).

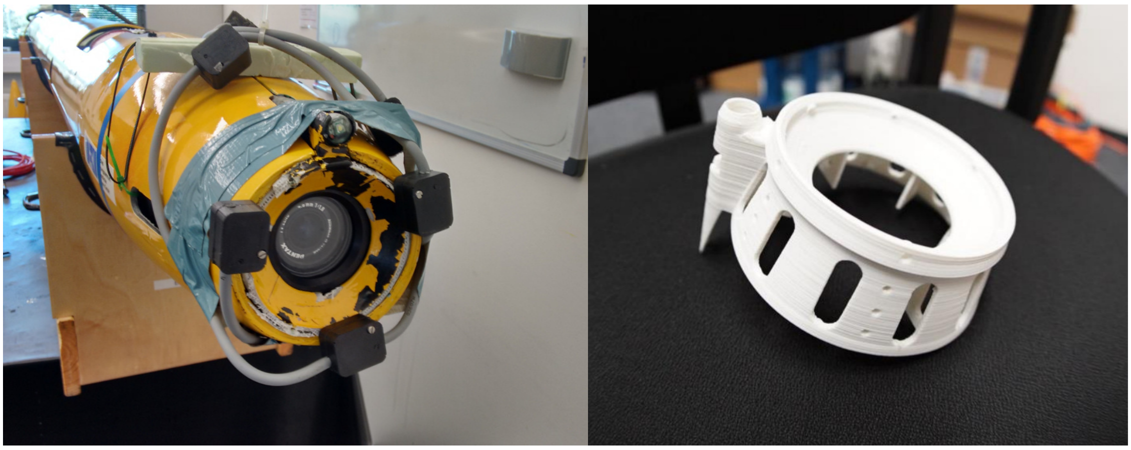

Figure 8.16: *AUV Leng with preliminary attached multi-magnetometer (v1) (left) and multi-magnetometer (v2) with 3d-printed sensorring (right)*

The experimental setup is shown in figure 8.17. The docking station fitted with both visual marker and magnet was placed in front of the AUV *Leng*, with a distance of 40 cm. It was then manually moved 10 times towards the camera, until the end docking position was reached to train a support vector machine regressor with an RBF kernel, which was identified to be the preffered machine learning approach in

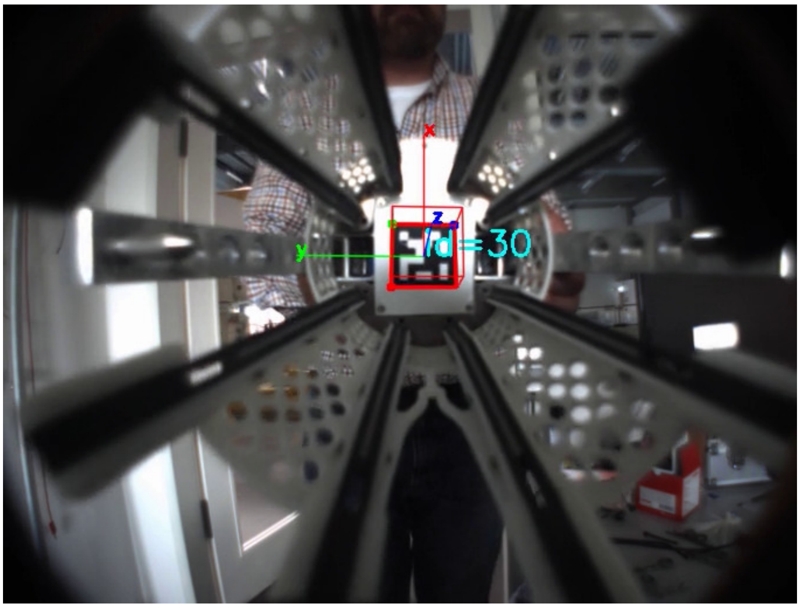

Figure 8.17: *Camera view of AUV Leng during dry docking experiment*

the laboratory experiment described before.

The ability to predict a position only using the magnetometers deployed at the nose of the AUV as a close-range localization solution is demonstrated in figure 8.18, comparing the standalone SVR-RBF predictions with the camera-based marker tracking. As can be seen, the difference in the magnetometer-predicted path stays below 10 cm and is getting smaller while the AUV approaches the docking station, down to a centimeter range.

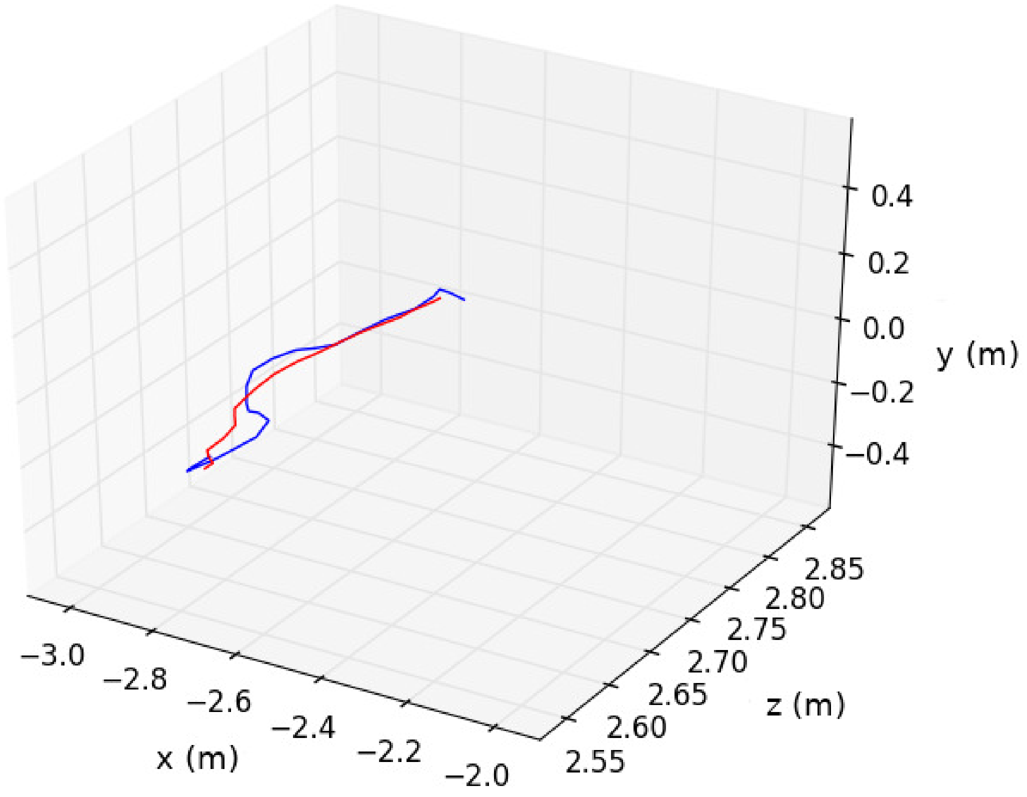

Figure 8.18: *Trajectory of the docking-approach during the AUV docking scenario as estimated by marker tracking (red) and magnetometer tracking (blue)*

8.4 Conclusion

After having shown that significant features of the ambient magnetic field are available in a lot of robotic application environments in Chapter 4 and introducing approaches to compensate for magnetic field distortions caused by activity and structure of the robots themselves in Chapter 6 and Chapter 7, this chapter discussed the actual exploitation of magnetic field distortions for localization purposes. An integrated visual-magnetic localization system utilizing machine learning for subsea docking applications has been described, that was first thoroughly tested in a laboratory environment and then transferred to a real AUV. Reflecting on the outcomes, it can be concluded that the magnetic field can be used both in combination and as a standalone source for localization in a close-proximity scenario, where turbidity may prevent the usage of visual sensors like cameras. While the experiments with the AUV *Leng* only allows for episodic insight due to the limited availability of the robot, the docking experiment with the AUV is in line with the findings of the laboratory experiment described earlier and with prior work of the author on magnetic field based localization using particle filters as described in Chapter 3, further supporting the feasibility of a general magnetic field based localization approach.

Chapter 9

Conclusions and Outlook

9.1 Thesis Summary

Present-day society envisions the help of AI systems in the near future in a variety of areas, ranging from daily tasks like packet delivery, public transport and healthcare to search-and-rescue missions or planetary exploration, to name just a few. Apart from pure artificial intelligence software systems, which are already taking an increasingly prominent role in day-to-day scenarios, more and more embodied intelligent systems, *robots*, are leaving the development labs and scientific office environments, and then have to cope with unstructured terrain and changing environmental conditions. Since robots cannot sense their environment directly, but have to infer information about it from noisy sensor information, it is crucial, that they do not depend on a narrow subset of possible sensor modalities, like visual information.

The underlying thought of this work was to deliberately steer away from the classical sensing modalities of robots towards an underutilized physical phenomenon for robot perception, the *ambient magnetic field*.

Two main assumptions were thus stated at the beginning of this work: a) The ambient magnetic field carries more information than we currently make use of, as indicated by animal magnetotaxis, and b) Since the ambient magnetic field is unaffected by a lot of effects that restrict commonly deployed localization sensors, magnetometers can play a crucial role both as an additional sensor modality for increased performance as well as robustness in mobile robot navigation

To substantiate these assumptions, this work first outlined the general principles of magnetism as well as types of magnetic distortions and then discussed the specific characteristics of the Earth's magnetic field and its main contributors with regard to robot localization. It was clarified, that temporal disturbances of the Earth's magnetosphere caused by solar storms, even though they may have a severe effect on electronics because of geomagnetically induced currents, are multiple orders of magnitude weaker than the geomagnetic field. Although the field is not entirely uniform and also not completely stable, this work presented several existing models for the spatial distribution and secular variations, so that for the purpose of robot navigation, the information on how the geomagnetic field should look like can be extracted for a given position and point in time.

After laying out the state of the art in robot localization, especially in relation to magnetic fields, this work then discussed the question, if and to what extent there is exploitable information in the individual features of local ambient magnetic fields. Therefore multiple possible robot application environments were assessed. Special care was taken to not only measure the strength component, as commonly done in the state of the art due to the convenient rotation-invariant property, but to use the full information content of vector field structures. Therefore, the directional component was coherently recorded in each assessed environment and the relationship between strength and direction in such magnetic fields was discussed. All evaluated environments were showing significant features in comparison to the locally uniform geomagnetic field due to ambient features of the environment, especially in environments with artificial structures and material of high magnetic permeability. But also more evenly distributed fields lend themselves to exploit the magnetic field features for navigation purposes, depending on the distribution of the features with respect to the scale of the navigation task, as long as the field is not uniform.

Given that there is exploitable information in ambient magnetic fields, this thesis then addressed the question, to what extent robot systems themselves distort the ambient magnetic field, and if typical sources of self-induced magnetic distortions for different classes of mobile robots can be identified. It became clear, that there are huge differences in the amount of the variations, typically increasing with the degrees of freedom of the robots and strongly influenced by the material choice of the systems and sensor placement. But despite this great variability over the range of assessed systems, the disturbances that occur were not of a magnitude that makes the underlying magnetic field indeterminable, but rather similar in scale to the features of the ambient magnetic fields evaluated before.

Nonetheless it became clear, that self-induced dynamic distortion is one of the main obstacles for magnetic field-based navigation, especially in confined mobile robots and thus one of the reasons for the alleged unreliability of magnetometers, even for simple compassing applications.

Hence, two possible approaches to compensate these effects have been introduced in this thesis: The first presented and evaluated approach combines specially developed hardware with a statistical approach based on von Mises-Fisher distributions. Alongside with the development of the algorithm, two versions of waterproof and pressure-tolerant multi-magnetometer sensor arrays and a software library to handle vMF distributions were developed and put to use in the course of this work.

As a second approach to compensate self-induced dynamic distortions, this thesis describes the use and evaluation of machine learning techniques like neural networks and support vector machine regression to learn a model of the magnetic field distortions in case there is embodied data available. The approach was evaluated both in a laboratory setup with separable distortion sources and with the complex robotic system *SherpaTT* in an outdoor environment. It was shown, that using proprioceptive information on the motor currents, body posture and current configuration, the deviations even of complex systems can be predicted by a trained MLP regressor, which is crucial for a wide variety of autonomous navigation purposes from simple heading estimation over standard SLAM approaches using IMUs to more specific magnetic field-based localization techniques.

Finally, this work presented and evaluated a method for close-proximity localization in a subsea docking scenario using the ambient magnetic field. It was shown, that the magnetic field can provide sufficient information for localization even in the case when magnetometers are the only sensory input left available to a robotic system.

9.2 Lessons Learned and Future Work

Although recent scientific evidence has made it into the news lately, that a geomagnetic field reversal is about to start or has already begun, this process will have no immediate impact on us or the next generations to come. The geomagnetic field is a fascinating phenomenon, which has huge influences on Life on Earth. This said, it is all the more astonishing that we humans only use the earth's magnetic field to a very small extent. Probably because humans, unlike some animal species, don't have the ability to perceive the surrounding magnetic field, lacking the senses needed for magnetoreception.

Although invisible, the magnetic field surrounding us provides valuable information for localization purposes. However, depending on the scale of the localization and precision requirements, not all environments are equally well suited for that purpose. For example, a busy steel trading warehouse would not be the first choice to enhance localization solutions with magnetometers, due to the expected significant changes of the magnetic field originating from the frequent movement of material with strong soft iron characteristics. At the other end of the spectrum are very large and nearly uniform ambient magnetic fields like the seafloor or a desert, that would not be suitable for close-range navigation in the centimeter range. Since the magnetic field cannot be sensed over a distance, robot navigation using magnetometers will be primarily useful in applications, where a robot passes through the same areas more than once, for example when setting up or sustaining a logistic chain, rather than during an exploring mission.

It also has become clear, that system distortion compensation is crucial and maybe one of the reasons, why magnetometers have not played a prominent role until now. After the years working with complex robots in magnetic fields, it is the author's firm conviction that machine learning methods are the most appropriate way to handle the complex intertwined magnetic fields of real-world scenarios, although the ML-approaches should be combined with clever hardware design to have the most benefit. In that sense, some of the more complex robots will require substantial effort to be eligible for the proposed approaches utilizing the magnetic field. IMU and magnetometer placement should be integrated into the design process of a robot, not only the determination of the actual placement, but also the consideration of the surrounding materials. Still, robots like the hominide robot *CHARLIE* will be less suited for magnetic field navigation than more rigid-bodied systems.

To further enhance the robustness of magnetometer readings on confined robotic systems in the future, it seems promising to use *Fisher-Bingham*-distribution instead of the vMF distribution in order to better account for per-axis dispersion on the unit sphere. In addition, as with deep learning in general and especially with artificial neural networks, future work on machine learning for magnetic field models should focus on getting more insight into the trained solutions, especially with respect to generalization as well as inter- and extrapolation capabilities. Nonetheless, an ML-based tool to establish magnetic field distortion models as presented in this work may become relevant in a lot of upcoming real-world scenarios in robotics, since it widens the usability of magnetometers as one of the core sensors in many navigation applications.

While the magnetic field can yield additional useful information for navigation, it cannot be sensed remotely, only directly at the point of the magnetometer. Furthermore, there is no direct mapping between the surrounding geometry and the expected magnetic field readings. While approaches like EmbodiedSLAM may be able to map things or geometry seen earlier in the sensory input to later experienced proprioceptive data, e.g. from tactile sensing, there is no direct mapping from pure geometry

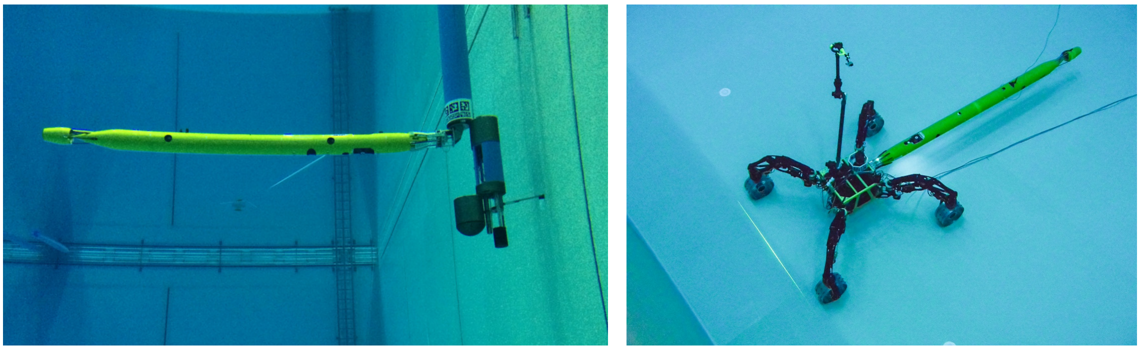

Figure 9.1: *The AUV Leng docking to the ice-shuttle Teredo and the subsea crawler SherpaUW*

to the magnetic field. Even if much more semantic information on the surroundings would be available, for example the expected material and the inner rigid structure of certain objects, there are no realtime analytical or numerical solutions currently available to deduct the surrounding magnetic field from that. The same holds true for the other way round: deducting shapes or objects in the surrounding only from magnetometer readings cannot be done at the moment, but may be worth looking into in the future.

Regarding the multi-magnetometer system, larger quantities of the developed magnetometer boards are currently in production and are planned to be permanently integrated for example in sensory platforms at the bottom of the North Sea and in current robot developments like a dual-arm intervention AUV. With the robot *SherpaUW* and the AUV *Leng* being already equipped with the proposed magnetometer array, the next steps here are to improve the robustness of the docking process depicted in figure 9.1 with the approach presented in this work. Another goal to be addressed in the near future concerning the multi-magnetometer system is to increase its usability also for applications outside robotics science.

Bibliography

[Akai and Ozaki, 2015] Akai, N. and Ozaki, K. (2015). Gaussian processes for magnetic map-based localization in large-scale indoor environments. In *2015 IEEE/RSJ International Conference on Intelligent Robots and Systems (IROS)*, Hamburg.

[Albiez et al., 2015] Albiez, J., Joyeux, S., Gaudig, C., Hilljegerdes, J., Kroffke, S., Schoo, C., Arnold, S., Mimoso, G., Alcantara, P., Saback, R., et al. (2015). Flatfish-a compact subsea-resident inspection auv. In *OCEANS'15 MTS/IEEE Washington*, pages 1–8. IEEE.

[Anderson-Sprecher, 1994] Anderson-Sprecher, R. (1994). Model comparisons and R^2. *The American Statistician*, 48(2):113–117.

[Banerjee et al., 2005] Banerjee, A., Dhillon, I. S., Ghosh, J., and Sra, S. (2005). Clustering on the unit hypersphere using von Mises-Fisher distributions. In *Journal of Machine Learning Research*, pages 1345–1382.

[Barnert et al., 2000] Barnert, S., Delbrück, M., Eis, R., Fischer, N., Greulich, W., Heinisch, C., Nagel, S., Radons, G., Schilling-Benz, L., and Schüller, J. (2000). Magnetisches Feld. In Greulich, W., editor, *Lexikon der Physik*. Spektrum Akademischer Verlag Heidelberg.

[Brighenti et al., 1998] Brighenti, A., Zugno, L., Mattiuzzo, F., and Sperandio, A. (1998). EURODOCKER-A universal docking-downloading-recharging system for AUVs: Conceptual design results. In *in Proc. Oceans 98, Oct*, page 1463.

[Caruso, 2000] Caruso, M. (2000). Applications of magnetic sensors for low cost compass systems. In *Position Location and Navigation Symposium, IEEE 2000*, pages 177–184.

[Chang and Lin, 2011] Chang, C.-C. and Lin, C.-J. (2011). LIBSVM. *ACM Transactions on Intelligent Systems and Technology*, 2(3):1–27.

[Cheshire and Baker, 1999] Cheshire, S. and Baker, M. (1999). Consistent overhead byte stuffing. *IEEE/ACM Transactions on networking*, 7(2):159–172.

[Christensen et al., 2011a] Christensen, L., Fischer, N., Kroffke, S., Lemburg, J., and Ahlers, R. (2011a). Cost-effective autonomous robots for ballast water tank inspection. *Journal of Ship Production and Design*, 27(3):127–136.

[Christensen et al., 2010] Christensen, L., Fritsche, M., Albiez, J., and Kirchner, F. (2010). USBL pose estimation using multiple responders. In *Proceedings of OCEANS 10 IEEE Sydney, Showcasing Advances in Marine Science and Engineering. Sydney, Australia*.

[Christensen et al., 2015] Christensen, L., Gaudig, C., and Kirchner, F. (2015). Distortion-Robust Distributed Magnetometer for Underwater Pose Estimation in Confined UUVs. In *Proceedings of MTS IEEE OCEANS '15*, pages 1–8, Washington DC, USA. IEEE.

[Christensen et al., 2009] Christensen, L., Kampmann, P., Hildebrandt, M., Albiez, J., and Kirchner, F. (2009). Hardware rov simulation facility for the evaluation of novel underwater manipulation techniques. In *OCEANS 2009-EUROPE*, pages 1–8. IEEE.

[Christensen et al., 2017] Christensen, L., Krell, M., and Kirchner, F. (2017). Learning magnetic field distortion compensation for robotic systems. In *Intelligent Robots and Systems (IROS), 2017 IEEE/RSJ International Conference on*, pages 1–6, Vancouver, Canada.

[Christensen et al., 2011b] Christensen, L., Lemburg, J., Vögele, T., Kirchner, F., Fischer, N., Ahlers, R., Psarros, G., and Etzold, L.-E. (2011b). Tank inspection by cost effective rail based robots. In *Proceedings of the 15th International Conference on Computer Applications in Shipbuilding, (ICCAS-11)*, Trieste.

[Christensen et al., 1998] Christensen, U., Olson, P., and Glatzmaier, G. A. (1998). A dynamo model interpretation of geomagnetic field structures. *Geophysical Research Letters*, 25(10):1565–1568.

[Chulliat et al., 2015] Chulliat, A., Macmillan, S., Alken, P., Beggan, C., Nair, M., Hamilton, B., Woods, A., Ridley, V., Maus, S., and Thomson, A. (2015). The US/UK world magnetic model for 2015-2020. Technical report, NOAA National Geophysical Data Center, Boulder, CO.

[Cole, 2005] Cole, S. B. (2005). Magnetic field-based navigation of a mobile robot. Master's thesis, Oklahoma State University.

[Cordes and Babu, 2016] Cordes, F. and Babu, A. (2016). SherpaTT: A versatile hybrid wheeled-leg rover. In *Proceedings of the 13th International Symposium on Artificial Intelligence, Robotics and Automation in Space (iSAIRAS 2016)*.

[Cordes et al., 2018] Cordes, F., Kirchner, F., and Babu, A. (2018). Design and field testing of a rover with an actively articulated suspension system in a mars analog terrain. *Journal of Field Robotics*, 35(7):1149–1181.

[Cox, 1991] Cox, I. J. (1991). Blanche-an experiment in guidance and navigation of an autonomous robot vehicle. *IEEE Transactions on robotics and automation*, 7(2):193–204.

[dos Santos Cesar et al., 2015] dos Santos Cesar, D. B., Gaudig, C., Fritsche, M., dos Reis, M. A., and Kirchner, F. (2015). An evaluation of artificial fiducial markers in underwater environments. In *OCEANS 2015-Genova*, pages 1–6. IEEE.

[Doucet et al., 2000] Doucet, A., De Freitas, N., Murphy, K., and Russell, S. (2000). Rao-blackwellised particle filtering for dynamic bayesian networks. In *Proceedings of the Sixteenth conference on Uncertainty in artificial intelligence*, pages 176–183. Morgan Kaufmann Publishers Inc.

[Durrant-Whyte et al., 1996] Durrant-Whyte, H., Rye, D., and Nebot, E. (1996). Localization of autonomous guided vehicles. In *Robotics Research*, pages 613–625. Springer.

[Endres et al., 2012] Endres, F., Hess, J., Engelhard, N., Sturm, J., Cremers, D., and Burgard, W. (2012). An evaluation of the rgb-d slam system. In *Proceedings of the IEEE International Conference on Robotics and Automation (ICRA)*, St. Paul - Minnesota, US.

[Eustice et al., 2007] Eustice, R. M., Whitcomb, L. L., Singh, H., and Grund, M. (2007). Experimental Results in Synchronous-Clock One-Way-Travel-Time Acoustic Navigation for Autonomous Underwater Vehicles. *Proceedings 2007 IEEE International Conference on Robotics and Automation*, pages 4257–4264.

[Finlay et al., 2010] Finlay et al., C. C. (2010). International geomagnetic reference field: the eleventh generation. *Geophysical Journal International*, 183:1216–1230.

[Fisher, 1953] Fisher, R. A. (1953). Dispersion on a sphere. In *Proc. Roy. Soc. London*, volume 217 of *A*, pages 295–305.

[Gabriel et al., 2010] Gabriel, G., Vogel, D., Wonik, T., Pucher, R., Krawczyk, C., Scheibe, R., and Lindner, H. (2010). Anomalien des erdmagnetischen totalfeldes der bundesrepublik deutschland. In *Jahrestagung der Deutschen Geophysikalis-*

chen Gesellschaft (DGG) 2010, Bochum. Leibniz-Institut für Angewandte Geophysik, Hannover.

[Garcia-Soto et al., 2017] Garcia-Soto, C., van der Meeren, G., Busch, J., Delany, J., Domegan, C., Dubsky, K., Fauville, G., Gorsky, G., Juterzenka K., v., Malfatti, F., G, M., Mchugh, P., Monestiez, P., J, S., Weslawski, J., and Zielinski, O. (2017). Advancing citizen science for coastal and ocean research. *Position Paper 23 of the European Marine Board, Ostend, Belgium, V., Kellett, P., Delany, J., McDonough, N. [Eds.], ISBN: 978-94-92043-30-6*, page 112pp.

[Garrido-Jurado et al., 2014] Garrido-Jurado, S., Muñoz-Salinas, R., Madrid-Cuevas, F., and Marín-Jiménez, M. (2014). Automatic generation and detection of highly reliable fiducial markers under occlusion. *Pattern Recognition*, 47(6):2280 – 2292.

[Gilbert, 1600] Gilbert, W. (1600). *De Magnete, Magneticisque Corporibus, et de Magno Magnete Tellure*. Peter Short, London.

[Girault et al., 2013] Girault, B., Bartsch, S., and Kirchner, F. (2013). Multifunctional robot test facility for on-orbit and extraterrestrial surface exploration. In *Proceedings of Ground-based Space facilities symposium, (GBSF-2013)*, Paris.

[Glatzmaier and Roberts, 1995] Glatzmaier, G. A. and Roberts, P. H. (1995). A three-dimensional self-consistent computer simulation of a geomagnetic field reversal. *Nature*, 377(6546):203–209.

[Glorot and Bengio, 2010] Glorot, X. and Bengio, Y. (2010). Understanding the difficulty of training deep feedforward neural networks. In *Aistats*, volume 9, pages 249–256.

[Grand and Thrun, 2012] Grand, E. L. and Thrun, S. (2012). 3-axis magnetic field mapping and fusion for indoor localization. In *Multisensor Fusion and Integration for Intelligent Systems*, Hamburg.

[Grisetti et al., 2007] Grisetti, G., Stachniss, C., and Burgard, W. (2007). Improved Techniques for Grid Mapping with Rao-Blackwellized Particle Filters. *IEEE Transactions on Robotics*, 23:34–46.

[Hildebrandt et al., 2013] Hildebrandt, M., Albiez, J., Wirtz, M., Kloss, P., Hilljegerdes, J., and Kirchner, F. (2013). Design of an Autonomous Under-Ice Exploration System. In *In MTS/IEEE Oceans 2013 San Diego, (OCEANS-2013)*, pages 1–6. IEEE.

[Hildebrandt and Christensen, 2017] Hildebrandt, M. and Christensen, L. (2017). Combining cameras, magnetometers and machine-learning into a close-range localization system for docking and homing. In *OCEANS 2017-Anchorage*, pages 1–6. IEEE.

[Hildebrandt et al., 2014] Hildebrandt, M., Gaudig, C., Christensen, L., Natarajan, S., Carrio, J. H., Paranhos, P. M., and Kirchner, F. (2014). A validation process for underwater localization algorithms. *International Journal of Advanced Robotic Systems*, 11.

[Hildebrandt et al., 2012] Hildebrandt, M., Gaudig, C., Christensen, L., Natarajan, S., Paranhos, P. M., and Albiez, J. (2012). Two years of experiments with the AUV Dagon - a versatile vehicle for high precision visual mapping and algorithm evaluation. In *Proceedings of IEEE/OES Autonomous Underwater Vehicles. Southampton, United Kingdom*.

[Hildebrandt and Hilljegerdes, 2010] Hildebrandt, M. and Hilljegerdes, J. (2010). Design of a versatile AUV for high precision visual mapping and algorithm evaluation. In *2010 IEEE/OES Autonomous Underwater Vehicles (AUV). Monterey, CA, USA*. IEEE/OES, IEEE.

[Hinton, 1989] Hinton, G. E. (1989). Connectionist learning procedures. *Artificial Intelligence*, 40(1-3):185–234.

[Hiscock et al., 2017] Hiscock, H. G., Mouritsen, H., Manolopoulos, D. E., and Hore, P. J. (2017). Disruption of Magnetic Compass Orientation in Migratory Birds by Radiofrequency Electromagnetic Fields. *Biophys. J.*, 113(7):1475–1484.

[Hobson et al., 2007] Hobson, B. W., McEwen, R. S., Erickson, J., Hoover, T., McBride, L., Shane, F., and Bellingham, J. G. (2007). The development and ocean testing of an auv docking station for a 21" auv. In *OCEANS 2007*, pages 1–6. IEEE.

[Johnsen and Lohmann, 2008] Johnsen, S. and Lohmann, K. (2008). Magnetoreception in animals. *Physics Today - PHYS TODAY*, 61.

[Jung et al., 2015] Jung, J., Oh, T., and Myung, H. (2015). Magnetic field constraints and sequence-based matching for indoor pose graph slam. *Robotics and Autonomous Systems*, 70:92–105.

[Kampmann et al., 2012] Kampmann, P., Lemburg, J., Hanff, H., and Kirchner, F. (2012). Hybrid pressure-tolerant electronics. In *Proceedings of the Oceans 2012 MTS/IEEE Hampton Roads Conference & Exhibition. Hampton Roads, Virginia, USA*.

[Kim, 2007] Kim, J. (2007). *Dual Control Approach for Automatic Docking using Monocular Vision*. Phd dissertation, Stanford University.

[Kingma and Ba, 2014] Kingma, D. P. and Ba, J. (2014). Adam: A method for stochastic optimization. *CoRR*, abs/1412.6980.

[Kirschvink et al., 2001] Kirschvink, J. L., Walker, M. M., and Diebel, C. E. (2001). Magnetite-based magnetoreception. *Current Opinion in Neurobiology*, 11(4):462 – 467.

[Kühn, 2016] Kühn, D. (2016). *Design and Development of a Hominid Robot with Local Control in Its Adaptable Feet to Enhance Locomotion Capabilities*. PhD thesis, Universität Bremen.

[Kümmerle and Grisetti, 2011] Kümmerle, R. and Grisetti, G. (2011). g2o: A general framework for graph optimization. In *IEEE International Conference on Robotics and Automation (ICRA)*.

[Kuo, 1088] Kuo, S. (1088). *Dream Pool Essays*. Diederichs Verlag Munich. Reprinted 1997 as *Pinsel-Unterhaltungen am Traumbach. Das Gesamte Wissen des Alten China*.

[Lee et al., 2013] Lee, C., Yoon, G., and Han, D. (2013). A probabilistic place extraction algorithm based on a superstate model. *Mobile Computing, IEEE Transactions on*, 12:945–956.

[Liu and Nocedal, 1989] Liu, D. C. and Nocedal, J. (1989). On the limited memory BFGS method for large scale optimization. *Mathematical programming*, 45(1):503–528.

[Loewe and Prölss, 1997] Loewe, C. A. and Prölss, G. W. (1997). Classification and mean behavior of magnetic storms. *Journal of Geophysical Research*, 102(A7):14209–14213.

[Maus et al., 2002] Maus, S., Rother, M., Holme, R., Lühr, H., Olsen, N., and Haak, V. (2002). First scalar magnetic anomaly map from champ satellite data indicates weak lithospheric field. *Geophysical Research Letters*, 29(14):45–1–47–4.

[Maxwell, 1865] Maxwell, J. C. (1865). Viii. a dynamical theory of the electromagnetic field. *Philosophical Transactions of the Royal Society of London*, 155:459–512.

[McElhinny and McFadden, 1998] McElhinny, M. and McFadden, P. L. (1998). *The magnetic field of the earth: paleomagnetism, the core, and the deep mantle*, volume 63. Academic Press.

[Montemerlo and Thrun, 2007] Montemerlo, M. and Thrun, S. (2007). Fastslam 2.0. *FastSLAM: A scalable method for the simultaneous localization and mapping problem in robotics*, pages 63–90.

[Montemerlo et al., 2002] Montemerlo, M., Thrun, S., Koller, D., Wegbreit, B., et al. (2002). Fastslam: A factored solution to the simultaneous localization and mapping problem. *Aaai/iaai*, 593598.

[Murarka et al., 2009] Murarka, A., Kuhlmann, G., Gulati, S., Flesher, C., Sridharan, M., and Stone, W. C. (2009). Vision-based frozen surface egress: A docking algorithm for the ENDURANCE AUV. In *Proceedings UUST09, Conference on Un-manned, Un-tethered Submersible Technology*, pages 22–25.

[National Research Council, 2008] National Research Council (2008). *Severe Space Weather Events: Understanding Societal and Economic Impacts: A Workshop Report*. The National Academies Press, Washington, DC.

[Nüchter et al., 2007] Nüchter, A., Lingemann, K., Hertzberg, J., and Surmann, H. (2007). 6d slam—3d mapping outdoor environments. *Journal of Field Robotics*, 24(8-9):699–722.

[Oehmcke et al., 2017] Oehmcke, S., Zielinski, O., and Kramer, O. (2017). Recurrent neural networks and exponential paa for virtual marine sensors. In *2017 International Joint Conference on Neural Networks (IJCNN)*, pages 4459–4466. IEEE.

[Olson, 2011] Olson, E. (2011). Apriltag: A robust and flexible visual fiducial system. In *Robotics and Automation (ICRA), 2011 IEEE International Conference on*, pages 3400–3407. IEEE.

[Pedregosa et al., 2011] Pedregosa et al., F. (2011). Scikit-learn: Machine learning in Python. *Journal of Machine Learning Research*, 12:2825–2830.

[Purucker, 2008] Purucker, M. E. (2008). A global model of the internal magnetic field of the moon based on lunar prospector magnetometer observations. *Icarus*, 197(1):19–23.

[Rahok et al., 2010] Rahok, S. A., Shikanai, Y., and Ozaki, K. (2010). Trajectory tracking using environmental magnetic field for outdoor autonomous mobile robots. In *2010 IEEE/RSJ International Conference on Intelligent Robots and Systems*, pages 1402–1407.

[Renaudin et al., 2010] Renaudin, V., Afzal, M. H., and Lachapelle, G. (2010). Complete triaxis magnetometer calibration in the magnetic domain. *Journal of sensors*, 2010.

[Robertson et al., 2013] Robertson, P., Frassl, M., Angermann, M., Doniec, M., Julian, B. J., Puyol, M. G., Khider, M., Lichtenstern, M., and Bruno, L. (2013). Simultaneous localization and mapping for pedestrians using distortions of the local magnetic field intensity in large indoor environments. In *International Conference on Indoor Positioning and Indoor Navigation*.

[Rock, 2013] Rock (2013). ROCK, the Robot Construction Kit. http://www.rock-robotics.org. Accessed: 2019-07-08.

[Sabaka et al., 2018] Sabaka, T. J., Tøffner-Clausen, L., Olsen, N., and Finlay, C. C. (2018). A comprehensive model of earth's magnetic field determined from 4 years of swarm satellite observations. *Earth, Planets and Space*, 70(1):130.

[Sagnotti et al., 2014] Sagnotti, L., Scardia, G., Giaccio, B., Liddicoat, J. C., Nomade, S., Renne, P. R., and Sprain, C. J. (2014). Extremely rapid directional change during Matuyama-Brunhes geomagnetic polarity reversal. *Geophysical Journal International*, 199:1110–1124.

[Sayad, 2019] Sayad, S. (2019). An introductin to data science. `https://www.saedsayad.com/support_vector_machine_reg.htm`. Accessed: 2019-07-08.

[Schwendner, 2013] Schwendner, J. (2013). *Embodied Localisation and Mapping*. PhD thesis, University of Bremen.

[Schwendner et al., 2014a] Schwendner, J., Joyeux, S., and Kirchner, F. (2014a). Using embodied data for localization and mapping. *Journal of Field Robotics*, 31(2):263–295.

[Schwendner and Kirchner, 2010] Schwendner, J. and Kirchner, F. (2010). eSLAM—Self Localisation and Mapping Using Embodied Data. *KI - Künstliche Intelligenz*, 24.

[Schwendner et al., 2014b] Schwendner, J., Roehr, T. M., Haase, S., Wirkus, M., Manz, M., Arnold, S., and Machowinski, J. (2014b). The artemis rover as an example for model based engineering in space robotics. In *Workshop Proceedings of the IEEE International Conference on Robotics and Automation 2014. Hong Kong, China*. IEEE.

[Siegwart et al., 2017] Siegwart, R., Chli, M., and Rufli, M. (2017). Autonomous Mobile Robots - Perception I: Sensors.

[Smola and Schölkopf, 2004] Smola, A. J. and Schölkopf, B. (2004). A tutorial on support vector regression. *Statistics and Computing*, 14(3):199–222.

[Sonsalla et al., 2017] Sonsalla, R., Cordes, F., Christensen, L., Roehr, T. M., Stark, T., Planthaber, S., Maurus, M., Mallwitz, M., and Kirchner, E. A. (2017). Field testing of a cooperative multi-robot sample return mission in mars analogue environment. In *Proceedings of the 14th Symposium on Advanced Space Technologies in Robotics and Automation (ASTRA)*.

[Sonsalla et al., 2015] Sonsalla, R. U., Akpo, J. B., and Kirchner, F. (2015). Coyote III: Development of a modular and highly mobile micro rover. In *Proceedings of the 13th Symposium on Advanced Space Technologies in Robotics and Automation (ASTRA-2015)*, Noordwijk, The Netherlands.

[Sonsalla et al., 2014] Sonsalla, R. U., Cordes, F., Christensen, L., Planthaber, S., Albiez, J., Scholz, I., and Kirchner, F. (2014). Towards a heterogeneous modular robotic team in a logistics chain for extended extraterrestial exploration. In *Proceedings of the 12th International Symposium on Artificial Intelligence, Robotics and Automation in Space-i-Sairas*.

[Sra, 2012] Sra, S. (2012). A short note on parameter approximation for von Mises-Fisher distributions: and a fast implementation of $I_s(x)$. *Computational Statistics*, 27(1):177–190.

[Telecommunications Industry Association et al., 2003] Telecommunications Industry Association et al. (2003). Tia-485-a, electrical characteristics of generators and receivers for use in balanced digital multipoint systems (ansi/tia/eia-485-a-98)(r2003).

[Thrun et al., 2005] Thrun, S., Burgard, W., and Fox, D. (2005). *Probabilistic Robotics (Intelligent Robotics and Autonomous Agents)*. The MIT Press.

[Vallivaara et al., 2010] Vallivaara, I., Haverinen, J., Kemppainen, A., and Röning, J. (2010). Simultaneous localization and mapping using ambient magnetic field. In *Multisensor Fusion and Integration for Intelligent Systems (MFI), 2010 IEEE Conference on*, pages 14–19. IEEE.

[Vapnik, 2000] Vapnik, V. (2000). The nature of statistical learning theory. *Springer*.

[Vissière et al., 2007] Vissière, D., Martin, A., and Petit, N. (2007). Using magnetic disturbances to improve imu-based position estimation. In *2007 European Control Conference (ECC)*, pages 2853–2858.

[Wirtz et al., 2012] Wirtz, M., Hildebrandt, M., and Gaudig, C. (2012). Design and test of a robust docking system for hovering AUVs. In *2012 Oceans*, pages 1–6. Ieee.

[Xu et al., 2006] Xu, H. G., Wang, C. X., Yang, R. Q., and Yang, M. (2006). Extended kalman filter based magnetic guidance for intelligent vehicles. In *2006 IEEE Intelligent Vehicles Symposium*, pages 169–175.

List of Figures

Acronyms

AMR	anisotropic magnetoresistance
ANN	Artificial Neural Network
AUV	autonomous underwater vehicle
BWT	ballast water tank
CGS	centimeter–gram–second system of units
CHAMP	Challenging Minisatellite Payload
CIR	co-rotating interaction region
CIRES	Cooperative Intitute for Research in Environmental Sciences
CME	coronar mass ejection
COBS	Consistent Overhead Byte Stuffing
DFKI	Deutsches Forschungszentrum für Künstliche Intelligenz
DLR	Deutsches Zentrum für Luft- und Raumfahrt
DoF	degrees of freedom
DVL	Doppler Velocity Log
EKF	Extended Kalman filter
FOG	Fibre Optic Gyroscope
GIC	geologically induced current
GLONASS	Globalnaja nawigazionnaja sputnikowaja sistema
GNSS	global navigation satellite system

GPS	Global Positioning System
I^2C	Inter-Integrated Circuit
IAGA	Internation Association of Geomagnetism and Aeronomy
IGRF	International Geomagnetic Reference Field
IHO	International Hydrographic Organization
IMU	Inertial Measurement Unit
IQR	interquartile range
LBFGS	Limited-memory Broyden-Fletcher-Goldfarb-Shanno algorithm
LBL	Acoustic Long Baseline Navigation System
LIDAR	Light Detection and Ranging
MEMS	microelectromechanical systems
ML	Machine Learning
MLP	Multilayer Perceptron Regression
NATO	North Atlantic Treaty Organization
NdFeB	Neodymium Iron and Boron
NGDC	National Geophysics Data Center
NOAA	National Oceanic and Atmospheric Administration
PMD	Photonic Mixing Device
PWM	pulse width modulation
RBF	Radial Basis Function
RBPF	Rao-Blackwellized Particle Filter
ReLU	Rectified linear unit
RGB-D	RGB camera with additional depth information
RIC	Robotics Innovation Center
RNN	Recurrent Neural Network
SI	Système international d’unités - International System of Units

SLAM	Simultaneous Localization and Mapping
SMD	Surface Mounted Device
SPI	Serial Peripheral Interface
sq	solar-quiet variation
SVC	Support Vector Classification
SVM	Support Vector Machine
SVR	Support Vector Regression
ToF	Time of Flight
USBL	Ultra Short Baseline Navigation System
UUV	Unmanned Underwater Vehicle
vMF	von Mises-Fisher
WMM	World Magnetic Model